Theses and Dissertations

August 2015

Tunneling Experiments with Dirac Electrons in Graphene Heterojunctions

Shivani Rajput
University of Wisconsin-Milwaukee

TUNNELING EXPERIMENTS WITH DIRAC ELECTRONS IN GRAPHENE

HETEROJUNCTIONS

by

Shivani Rajput

A Dissertation Submitted in

Partial Fulfilment of the

Requirement for the Degree of

Doctor of Philosophy

in Physics

at

The University of Wisconsin – Milwaukee

August 2015

ABSTRACT

TUNNELING EXPERIMENTS WITH DIRAC ELECTRONS IN GRAPHENE
HETEROJUNCTIONS

by

Shivani Rajput

The University of Wisconsin – Milwaukee, 2015
Under the Supervision of Professor Lian Li

This dissertation presents results of scanning tunneling microscopy/spectroscopy experiments performed on graphene, a two-dimensional membrane of carbon atoms arranged in a honeycomb lattice, where charge carriers behave like massless fermions described by the Dirac equation. Our findings demonstrate that interface engineering is a viable route to control and further enhance the electronic properties of graphene.

In the first experiment, by transferring chemical vapor deposited (CVD) graphene onto substrates of opposite polarization - H-terminated Si-face and C-faces of hexagonal silicon carbide (SiC), we show that the type of charge carrier in graphene can be controlled by substrate polarization. Furthermore, we find that the charge carrier in epitaxial graphene/Si-face SiC(0001) convert from n- to p-type upon H-intercalation at the interface. Finally, we observe the formation of ripples in the graphene H-terminated SiC heterojunctions, which causes atomic scale fluctuations in the Dirac point. Density functional theory calculations suggest the formation of a Schottky dipole just ~ 1 nm at the graphene/SiC interface, thus the Dirac point depends strongly on the spacing between

graphene and SiC. As a result, ripples, i.e., atomic scale topographic fluctuations of graphene with respect to the substrate, lead to the variations in the Dirac point.

In the second experiment, we discover two types of intrinsic atomic-scale inhomogeneities that can cause fluctuations in the Schottky barrier height at graphene/semiconductor junctions: graphene ripples and/or trapped charge impurities and surface states of the semiconductor. These findings provide insight into the fundamental physics of nanoscale devices based on graphene - semiconductor junctions.

In the third experiment, we experimentally demonstrate proximity-induced spin-orbit coupling in graphene-topological insulator van der Waals (vdW) heterostructures fabricated by transferring CVD graphene onto Bi_2Se_3 grown by molecular beam epitaxy. We observe a spin-orbit splitting of up to 80 meV in the graphene Dirac states, an enhancement of several orders of magnitude compared to the intrinsic value. Moreover, the spin-orbit splitting exhibits spatial variations of ± 20 meV, as a result of the lack of epitaxial relation between the graphene and Bi_2Se_3 layers. Density functional theory calculations further reveal that this giant spin-orbit splitting of the graphene bands is a consequence of the orthogonalization requirement on the overlapping wave functions, rather than arising from simple direct bonding at the interface. This revelation of the indirect bonding mechanism of the proximity effect is an enabling step towards more effective engineering of desired properties in vdW heterostructures.

iii

TABLE OF CONTENTS

LIST OF FIGURES

LIST OF ABBREVIATIONS

1D	One-dimensional
2D	Two-dimensional
2DEG	Two-dimensional electron gas
3D	Three-dimensional
AFM	Atomic force microscopy
ARPES	Angle-resolved photoemission spectroscopy
BZ	Brillouin zone
CVD	Chemical vapor deposition
DFT	Density functional theory
dI/dV	Differential tunneling conductance
DOS	Density of states
FWHM	Full width at half maximum
PZT	Lead zirconate titanate
QFS	Quasi-free standing
QL	Quintuple layer
SiC	Silicon carbide
SOC	Spin orbit coupling
STM	Scanning tunneling microscopy
STS	Scanning tunneling spectroscopy
TEM	Transmission electron microscopy
UHV	Ultra-high vacuum
vdW	Van der Waals

ACKNOWLEDGEMENTS

I would like to thank a number of people who have encouraged and helped me throughout my graduate experience. Foremost, I like to express my gratitude to my advisor Prof. Lian Li for his endless support and patient guidance. I have been very fortunate to have an advisor who gave me opportunity to conduct cutting-edge research in the area of graphene. He always encouraged me to think of newer ideas and provided direction at each step of the way. Working with him, I can feel his dedication as a physicist and whole hearted support as an advisor.

I also like to thank my PhD committee members Prof. Michael Weinert, Prof. Deniel Agterberg, Prof. Marija Gajdardziska and Prof. Jorg Woehl for their time, mentoring and all their inputs in this work. Thanks to Prof. Michael Weinert for being a great collaborator and for many useful discussions related to my research. I like to thank all the former and present members of Li's laboratory to support me and work with me on various projects; Dr. Yaoyi Li, Dushyant Tomer, Lawrence Hudy, Zhuozhi Ge, Rusty Mundorf, but especially to Dr. Ying Liu for introducing me to many instruments in the lab during my initial stay here.

I like to thank to all the faculty, graduate students and staff members of the Physics department. I also appreciate the help from a number of people: Jerry for always willing to help on the technical details in machine shop, Dr. Steve Hardcastle for AFM and Raman training and Dr. Heather Owen for SEM training, Kate Valerius for official paper work and Reba Sinha for clearing my reimbursement forms. I also like to thank Donald Robertson

for all the interesting lunch chats and helping me on various aspect such as carrying gas cylinders, using optical microscope and filling Liquid nitrogen on the dock.

Last but not the least, I would like to express my gratitude to my parents and family members for their devoted love and support. I also feel grateful to my husband, Dushyant Tomer, who have always been a source of encouragement. Without his support, this dissertation would not have been possible.

Chapter 1
Introduction

1.1 Introduction

Graphene is an atomic layer of carbon atoms arranged in a honeycomb lattice. Carbon atoms in graphene are covalently bonded to their nearest neighbors with in-plane σ bonds formed by sp^2 hybridization. Graphene is the building block of all the sp^2 graphitic allotropes; three-dimensional (3D) graphite, one-dimensional (1D) carbon nanotubes and zero dimensional fullerenes [1]. Graphite may be viewed as a stack of graphene sheets held together by the van der Waals (vdW) interaction, which is much weaker than the in-plane covalent bonds. Thus, it is possible to peel the graphene layers off of the bulk graphite samples. Although graphene has been studied theoretically since the mid-1900s [1, 2], it was only first experimentally isolated from graphite in 2004 by the Manchester group [3]. They used simple scotch tape to mechanically exfoliate monolayer graphene, for which Drs. Andre Geim and Konstantin Novoselov were awarded the 2010 Noble Prize in Physics [4].

Graphene is the first two-dimensional (2D) crystalline material that is observed to be stable at room temperature. Before 2004, it was believed that strictly 2D crystals were thermodynamically unstable [5, 6]. Thermal fluctuations destroy long range order in low dimensional crystals ($d \leq 2$) resulting in melting of the 2D lattice at finite temperature. However, anhormonic coupling between bending and stretching modes suppresses these fluctuations, which stabilizes the 2D membranes through their deformation in the third dimension [7, 8]. Indeed, transmission electron microscopy (TEM) experiments and Monte

Carlo simulation reveal that monolayer graphene displays long range crystalline order, but has the tendency to form intrinsic atomic scale ripples within its surface [9, 10]. These imperfections are believed to be the reason for the stability of graphene at room temperature. Additionally, the strong in-plane σ bonds in graphene avoid the formation of dislocations or other defects due to thermal fluctuations.

In addition, when placed on most commonly used SiO_2 substrate, graphene conforms to the rough oxide surface and exhibits random topographic corrugations with lateral dimension of few nm and vertical dimension of few Å [11-13]. A careful analysis of scanning tunneling microscopy (STM) images suggests that the graphene topographic corrugations are a result of the underlying SiO_2 surface roughness, as well as the intrinsic ripples of graphene [11]. Atomic scale STM imaging shows that the honeycomb graphene lattice is continuous along the topographic corrugations with almost no defects.

When graphene is supported by a substrate with an atomically flat surface such as mica, h-BN or graphite, the height of the corrugations become as small as 20-30 pm [14-17]. Recent work suggests that 2D layered crystals such as MoS_2, WS_2, and WSe_2 are also viable substrates [18]. These results suggest that intrinsic ripples observed in suspended graphene can be strongly suppressed by the vdW interactions between graphene and an appropriate choice of substrate. However, the lattice mismatch and relative rotation angle between graphene and the vdW materials can result in Moiré patterns that leads to periodic corrugations in the topography [15, 19]. The periodicity of the moiré pattern depends on the relative rotational angle, and thus vary spatially on the sample in case of random alignment between the two crystals.

In neutral graphene, the Fermi level coincides with the Dirac point and the density of states (DOS) are electron-hole symmetric, thereby the Dirac point is commonly labeled as the charge neutrality point. When the surface charge density of graphene is changed either by doping with impurities or by application of an external electric field, the Fermi level shifts relative to the Dirac point [20, 21]. Depending on the electron- or hole- doping, the Dirac point moves below or above the Fermi level, respectively, as shown in Fig. 1.1(a). The charge carrier concentration in doped graphene can be estimated by $n(p) = 4\pi E_D{}^2/(\hbar v_f)^2$, where E_D is the Dirac point energy, $\hbar$ the Planck constant and v_f Fermi velocity of electrons.

The electronic properties of graphene heterostructures are strongly affected by disorder at the interface and charge impurities underneath graphene. The random charge impurities create an inhomogeneous electrostatic potential landscape, which causes fluctuations in the Dirac point energy across the graphene surface and produces spatial charge density inhomogeneity. Spatial inhomogeneity of charge carriers lead to the formation of electron and hole puddles in graphene [12, 13, 15, 22]. An illustration of the situation is shown in Fig 1.1(b).

Electron-hole puddles was first observed in graphene on SiO$_2$ by a single electron transistor with a spatial resolution of hundred nm and density fluctuations of the order of 4×10^{10} cm^{-2} [22]. Atomic resolution tunneling spectroscopy measurements on graphene/SiO$_2$ heterostructures exhibit $\sim$ 30-50 meV variation in the Dirac point that corresponds to a charge density inhomogeneity of 2×10^{11} - 4×10^{11} cm^{-2} [12, 13]. However, simultaneous mapping of topography and tunneling conductance confirms that electron-hole puddles are not related to the topographic corrugations of graphene, but to the charge

impurities in the substrate [12]. This is consistent with extremely low charge impurities concentration observed in suspended graphene in Raman measurements [23].

In layered vdW substrates such as h-BN and MoS_2, charge impurities does not exist in great quantities. Thus, the carrier density fluctuations in graphene on h-BN substrate are two orders of magnitude smaller in comparison to SiO_2 [15, 16]. However, moiré patterns in graphene/h-BN heterostructure act as weak periodic potential and leads to the emergence of new set of Dirac points in electronic spectrum [19]. As a result, periodic modulation appears in the local DOS of graphene near the new Dirac cones with the same period as that of topographic moiré pattern. Recent work further shows additional inhomogeneous strain distribution due to a commensurate-incommensurate transition in graphene/h-BN heterostructure, which strongly depends on the rotation angle between the lattices of the two crystals [24].

1.2   Motivation

The earlier work summarized above clearly shows that being a truly 2D material, the structural and electronic properties of graphene are extremely sensitive to immediate environment, especially to the supporting substrates underneath. This, however, also indicates a viable route to control and further enhance graphene's properties by forming heterojunctions. In the case of graphene interfaced with a semiconductor, a Schottky contact forms at the junction with rectifying properties [25]. As graphene is prone to form ripples that modulate its local electronic properties, one critical question is whether the graphene ripples will have an impact on the Schottky barrier formation.

The prediction of the quantum spin Hall effect in graphene [26], together with ultra-high electron mobility and long spin relaxation length makes it a potential material for spintronics [27, 28]. However, extremely small intrinsic spin orbit coupling (SOC) in graphene is a hurdle to overcome. Earlier attempts of enhancing the SOC in graphene have mostly relied on chemical functionalization and adsorption of heavy atoms [29-31], which introduces scattering centers or compromising graphene's structural integrity and/or intrinsic property such as high carrier mobility. By proximity to a topological insulator Bi_2Se_3, it has been shown that SOC in graphene can be enhanced by several orders of magnitude [32, 33]. However, Bi_2Se_3 itself also exhibits a layered structure with anisotropic in-plane strong covalent and out-of-plane weak vdW bonding [34]. As such, the interface between graphene and Bi_2Se_3 is expected to be vdW, fundamentally different from the legacy heteroepitaxy of covalently bonded semiconductors. The weak interlayer bonding, thus the lack of epitaxial relation between the two layers, however, can present unique challenges in tailoring the transferred SOC in graphene. In particular the non-epitaxial registration between layers can lead to spatial variation of the properties, thus requiring the understanding of the interface in graphene heterojunctions at the atomic scale.

STM is a powerful tool used to study the structural and electronic properties of conducting surfaces at the atomic scale. Besides its unique spatial and energy resolution, imaging and spectroscopy measurements can be performed simultaneously with the STM, and thereby facilitating a correlation between topographic features and electronic structure in ways not possible with other techniques. From the perspective of an STM experimentalist, graphene is a unique material in two important ways. First, the surface is the material in the case of graphene. Thus, an STM probe directly accesses the bulk

electronic states that contribute to transport and optical transitions, unlike in case of 3D materials where STM can only probe the surface states. Second, graphene is stable at room temperature. Information gained by STM measurements on graphene in ultra-high vacuum (UHV) reflects the material properties in ambient conditions, which is not the case for many conducting surfaces. Indeed, spectroscopy measurements on local imperfections, such as impurities, defects, grain boundaries and intrinsic ripples, are used in understanding their roles in transport [35, 36].

1.3   Outline of Dissertation

This dissertation addresses atomic scale inhomogeneity in graphene heterojunctions using STM and is organized as follows:

Chapter 1 provides a brief review of inhomogeneities in graphene heterojunctions that are relevant to this work, and the motivation of this dissertation.

Chapter 2 provides an introduction of the atomic and electronic properties of graphene.

Chapter 3 starts with a summary of graphene synthesis, focusing particularly on the epitaxial graphene growth on silicon carbide (SiC) and chemical vapor deposition (CVD) on Cu foil. Furthermore, it describes a step by step graphene transfer process from Cu foil to an arbitrary substrate using polymer assisted method.

Chapter 4 covers the working principles of the main characterization techniques. Section 4.1 provides an introduction of STM including the original tunneling theory developed by Bardeen and how it has been applied to STM by Tersoff and Hamann. (The instrumentation of STM/STS is provided in Appendix A.) Section 4.2 presents the basic theory of Raman scattering, followed by description of the main Raman bands observed in graphene.

Chapter 5 first presents the STM and Raman measurements on epitaxial graphene on hexagonal Si-face SiC before and after hydrogen intercalation, and explores the origin of p-type doping in hydrogen intercalated graphene. Then, polarization doping of graphene is investigated by directly transferring the CVD graphene onto H-terminated Si- and C-faces of hexagonal SiC.

Chapter 6 presents an atomic scale study of the Schottky barrier formation at the graphene-semiconductor junctions on polar (Si- and C-face SiC) as well as non-polar (Si and GaAs) semiconductor substrates, which also allows us to explore the impact of the electric field on Schottky barrier formation.

Chapter 7 presents the experimental results and density functional theory (DFT) calculations of the graphene-Bi_2Se_3 heterostructure. We find a spin-orbit coupling transferred in graphene due to proximity to Bi_2Se_3 is up to 80 meV, several orders of magnitude greater than the intrinsic values of $\sim\mu$eV [37]. We also show that the weak interlayer bonding, thus the lack of epitaxial relation between the layers can lead to spatial variation of proximity-induced properties in vdW heterostructures.

Chapter 8 provides summary and prospective.

References

1. R. Saito, G. Dresselhaus and M. S. Dresselhaus. Physical Properties of Carbon Nanotubes. Imperial College Press, London (1998).
2. P. R. Wallace *et al.* The band theory of graphite. *Phys. Rev.* **71,** 622 (1947).
3. K. S. Novoselov *et al.* Electric field effect in atomically thin carbon films. *Science* **306**, 666 (2004).
4. A. K. Geim. Random walk to graphene. Nobel lecture (2010).

5. L. D. Landau. Zur Theorie der Phasenumwandlungen II. *Phys. Z. Sowjetunion* **11,** 26 (1937).

6. N. D. Mermin. Crystalline order in two dimensions. *Phys. Rev.* **176,** 250 (1968).

7. D. R. Nelson and L. Peliti. Fluctuations in membranes with crystalline and hexatic order. *J. Phys.* **48,** 1085 (1987).

8. D. R. Nelson, T. Piran and S. Weinberg. Statistical Mechanics of Membranes and Surfaces. World Scientific, Singapore (2004).

9. J. C. Mayer, A. K. Geim, M. I. Katsnelson, K. S. Novoselov, T. J. Booth and S. Roth. The structure of suspended graphene sheets. *Nature* **446,** 60 (2007).

10. A. Fasolino, J. H. Los and M. I. Katsnelson. Intrinsic ripples in graphene. *Nat. Materls.* **6,** 858 (2007).

11. V. Geringer *et al.* Intrinsic and extrinsic corrugation of monolayer graphene deposited on SiO_2. *Phys. Rev. Lett.* **102,** 076102 (2009).

12. Y. Zhang, V. W. Brar, C. Girit, A. Zettl, and M. F. Crommie. Origin of spatial charge inhomogeneity in graphene. *Nat. Phys.* **5**, 722 (2009).

13. A. Deshpande, W. Bao, F. Miao, C. N. Lau and B. J. LeRoy. Spatially resolved spectroscopy of monolayer graphene on SiO_2. *Phys. Rev. B* **79**, 205411 (2009).

14. C. H. Lui, L. Liu, K. F. Mak, G. W. Flynn and T. F. Heinz. Ultraflat graphene. *Nature* **462**, 339 (2009).

15. J. Xue *et al.* Scanning tunneling microscopy and spectroscopy of ultra-flat graphene on hexagonal boron nitride. *Nat. Mater.* **10**, 282 (2011).

16. C. R. Dean *et al.* Boron nitride substrate for high quality graphene electronics. *Nat. Nanotechnol.* **5,** 722 (2010).

17. G. Li, A. Luican and E. Y. Andrei. Scanning tunneling spectroscopy of graphene on graphite. *Phys. Rev. Lett.* **102,** 176804 (2009).

18. J. Y. Tan *et al*. Electronic transport in graphene based heterostructures. *Appl. Phys. Lett.* **104**, 183504 (2014).

19. M. Yankowitz *et al.* Emergence of supperlattice Dirac points in graphene on hexagonal boron nitride. *Nat. Phys.* **8,** 382 (2012).

20. A. H. Castro Neto, F. Guinea, N. M. R. Peres, K. S. Novesolev and A. K. Geim. The electronic properties of graphene. *Rev. Mod. Phys.* **81,** 109 (2009).

21. Y. Zhang *et al.* Giant phonon-induced conductance in scanning tunneling spectroscopy of gate-tunable graphene. *Nat. Phys.* **4,** 627 (2008).

22. J. Martin *et al.* observation of electron-hole puddles in graphene using a scanning single-electron transistor. *Nat. Phys.* **4**, 144 (2008).

23. Z. H. Ni *et al.* Probing charged impurities in suspended graphene using Raman spectroscopy. *ACS Nano* **3,** 569 (2009).

24. C. R. Wood *et al.* Commensurate-incommensurate transition in graphene on hexagonal boron nitride. *Nat. Phys.* **10,** 451 (2014).

25. S. Tongay *et al.* Rectification at graphene-semiconductor interfaces: Zero-gap semiconductor based diodes. *Phys. Rev. X* **2,** 011002 (2012).

26. C. L. Kane and E. J. Mele. Quantum spin Hall Effect in graphene. *Phys. Rev. Lett.* **95,** 226801 (2005).

27. K. L. Bolotin *et al.* Ultrahigh electron mobility in suspended graphene. *Solid state comm.* **146,** 351 (2008).

28. T. Maassen *et al.* Long spin relaxation times in wafer scale epitaxial graphene on SiC (0001). *Nano Lett.* **12,** 1498 (2012).

29. J. Balakrishnan, G. K. W. Koon, M. Jaiswal, A. H. CastroNeto and B. Ozyilmaz. Colossal enhancement of spin–orbit coupling in weakly hydrogenated graphene. *Nat. Phys.* **9,** 284 (2013).

30. D. Marchenko *et al.* Giant Rashba splitting in graphene due to hybridization with gold. *Nat. Comm.* **3,** 1232 (2012).

31. C. Weeks, J. Hu, J. Alicea, M. Franz and R. Wu. Engineering a robust quantum spin Hall state in graphene via adatom deposition. *Phys. Rev. X* **1,** 021001 (2011).

32. K. H. Jin and S-H Jhi. Proximity-induced giant spin-orbit interaction in epitaxial graphene on a topological insulator. *Phys. Rev. B* **87,** 075442 (2013).

33. J. Zhang, C. Triola and E. Rossi. Proximity effect in graphene-topological insulator heterostructures. *Phys. Rev. Lett.* **112,** 096802 (2014).

34. H. Zhang, C.-X. Liu, X.-L. Qi, X. Dai, Z. Fang and S. C. Zhang. Topological insulator in Bi_2Se_3, Bi_2Te_3 and Sb_2Te_3 with a single Dirac cone on the surface. *Nat. Phys.* **5,** 438 (2009).

35. L. Zhao *et al.* Visualizing individual nitrogen dopants in monolayer graphene. *Science* **333**, 999 (2009).

36. L. Tapaszto *et al.* Mapping the electronic properties of individual graphene grain boundaries. *App. Phys. Lett.* **100,** 053114 (2002).

37. Y. Yao, F. Ye, X. L. Qi, S. C. Zhang and Z. Fang. Spin-orbit gap of graphene: First-principles calculations. *Phys. Rev. B* **75,** 041401 (2007).
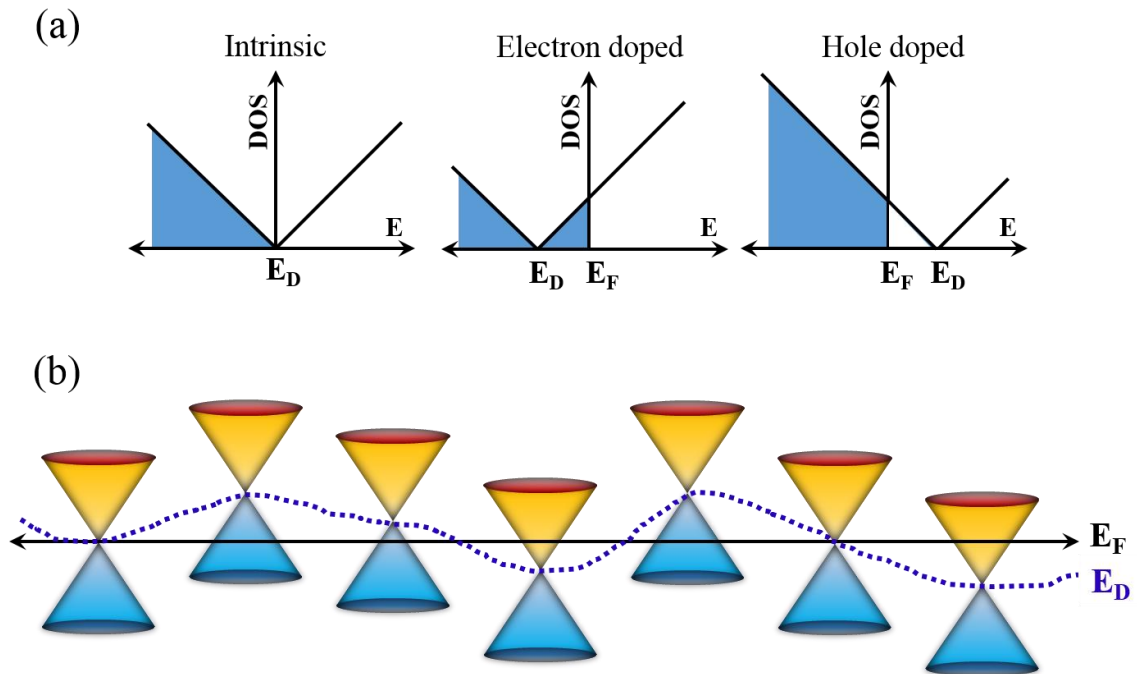
Figure 1.1: (a) Schematic of the DOS of intrinsic, electron- and hole-doped graphene where Dirac point is at, below and above the Fermi level, respectively. (b) Illustration of the Dirac point variation relative to the Fermi energy across a graphene sample that causes spatial charge inhomogeneity.

Chapter 2
Graphene Basics

2.1 Graphene band structure

The primitive unit cell of monolayer graphene contains two carbon atoms at sites A and B, as shown by a shaded diamond in Fig. 2.1(a). The carbon atom at site A has three nearest neighbors at site B and vice versa, separated by carbon-carbon distance $a_{c-c} = 1.42$ Å. The unit lattice vectors $\overrightarrow{a_1}$ and $\overrightarrow{a_2}$ can be written in Cartesian coordinates as:

$$\overrightarrow{a_1} = a\left(\frac{\sqrt{3}}{2}\hat{x} + \frac{1}{2}\hat{y}\right), \quad \overrightarrow{a_2} = a\left(\frac{\sqrt{3}}{2}\hat{x} - \frac{1}{2}\hat{y}\right) \tag{2.1}$$

where $a = |\overrightarrow{a_1}| = |\overrightarrow{a_2}| = \sqrt{3}\,a_{c-c} = 2.46$ Å is the lattice constant of monolayer graphene. The unit cell in reciprocal space is also a hexagonal lattice, rotated 30° relative to the real space lattice [Fig. 2.1(b)]. There are four high symmetry points in the first Brillouin zone (BZ): the Γ point at zone center, the M point in the middle of hexagon sides and the K and K' points at the corners of the hexagon. Notice that the K and K' points are inequivalent since they cannot be connected by the unit vectors of the reciprocal lattice $\overrightarrow{b_1}$ and $\overrightarrow{b_2}$, given by

$$\overrightarrow{b_1} = \frac{2\pi}{a}\left(\frac{1}{\sqrt{3}}\hat{x} + \hat{y}\right), \quad \overrightarrow{b_2} = \frac{2\pi}{a}\left(\frac{1}{\sqrt{3}}\hat{x} - \hat{y}\right) \tag{2.2}$$

Each carbon atom contributes four valence electrons ($2s$, $2p_x$, $2p_y$ and $2p_z$) per unit cell, so there are eight electronic energy bands 3 σ, 3 σ^*, 1 π and 1 π^* [1]. The $2s$, $2p_x$ and $2p_y$ orbitals of a carbon atom hybridize into a sp^2 configuration and generate three sp^2 orbitals, which lie in the graphene plane at an angle of 120°. Overlapping of the sp^2 orbitals of two neighboring carbon atoms forms three σ bonding and three σ^* antibonding bands. The

remaining two $2p_z$ orbitals hybridize and form π bonding and π^* anti-bonding bands orthogonal to the graphene plane. The 3σ and π bonding bands are completely filled and lie below the Fermi level. Out of the 8 electrons per unit cell, 6 electrons fill the 3σ bands and remaining two fill the π energy bands with spin up and spin down electrons. The $3\sigma^*$ and the π^* antibonding bands are unoccupied in the ground states and all lie above the Fermi level. The electronic properties of graphene at low energies are mainly determined by the π electrons, because the σ electrons form bands far away from the Fermi energy and play no role.

2.1.1 The π bands

The energy dispersion of π electrons in graphene was first derived in 1947 by Wallace using the tight binding approximation [2]. In tight binding, the wave function is constructed as a linear combination of the valence orbitals of all of the atoms in the primitive unit cell of a crystal. Considering only $2p_z$ orbitals of each carbon atom in the unit cell, the tight binding wave function of graphene can be written as

$$\psi_{\vec{k}}(\vec{r}) = \frac{1}{\sqrt{N}} \sum_{\vec{R}} e^{i\vec{k}.\vec{R}} \left[c_A \, \varphi_A(\vec{r} - \vec{R}) + c_B \varphi_B(\vec{r} - \vec{R}) \right] \tag{2.3}$$

where N is the number of unit cells, R is the set of all lattice vectors, φ_A and φ_B are the $2p_z$ orbitals of carbon atoms at site A and B respectively, and c_A and c_B are constants that represent the probability amplitude of an electron being on the A site or the B site carbon atom, respectively, such that $|c_A|^2 + |c_B|^2 = 1$. To determine dispersion relation, multiply the time independent Schrodinger equation from the left by the states φ_A and φ_B and integrate over space. This results in the following two equations

$$\langle\varphi_A|H|\psi_k\rangle = E\langle\varphi_A|\psi_k\rangle \tag{2.4}$$

$$\langle\varphi_B|H|\psi_k\rangle = E\langle\varphi_B|\psi_k\rangle \tag{2.5}$$

Substituting Eq. (2.3) in Eq. (2.4), we have

$$\sum_{\vec{R}} e^{i\vec{k}.\vec{R}} \left[c_A \left\langle \varphi_A(\vec{r}) \middle| H \middle| \varphi_A(\vec{r}-\vec{R}) \right\rangle + c_B \left\langle \varphi_A(\vec{r}) \middle| H \middle| \varphi_B(\vec{r}-\vec{R}) \right\rangle \right]$$

$$= E \sum_{\vec{R}} e^{i\vec{k}.\vec{R}} \left[c_A \left\langle \varphi_A(\vec{r}) \middle| \varphi_A(\vec{r}-\vec{R}) \right\rangle + c_B \left\langle \varphi_A(\vec{r}) \middle| \varphi_B(\vec{r}-\vec{R}) \right\rangle \right] \tag{2.6}$$

If we consider that all overlaps are negligible except for nearest neighbors, only on-site matrix elements for $\vec{R} = 0$ and nearest neighbor matrix elements for $\vec{R} = \vec{n_l}$ are retained in the first and second term on the left side, respectively, where $\vec{n_l}$ are nearest neighbor vectors. We also neglect direct overlap of $2p_z$ orbitals centered on different atoms, e.g. $\left\langle \varphi_A(\vec{r}) \middle| \varphi_B(\vec{r}-\vec{R}) \right\rangle = 0$. Then only taking the on-site term on the right side, Eq. (2.6) can be written as

$$c_A\langle\varphi_A(\vec{r})|H|\varphi_A(\vec{r})\rangle + c_B \sum_{l} e^{i\vec{k}.\vec{n_l}} \langle\varphi_A(\vec{r})|H|\varphi_B(\vec{r}-\vec{n_l})\rangle = E c_A\langle\varphi_A(\vec{r})|\varphi_A(\vec{r})\rangle \tag{2.7}$$

Now, we define the on-site energy of the $2p_z$ orbitals as $\left\langle \varphi_{A(B)}(\vec{r}) \middle| H \middle| \varphi_{A(B)}(\vec{r}) \right\rangle = \varepsilon_0$, and for normalized wave function $\langle\varphi_A(\vec{r})|\varphi_A(\vec{r})\rangle = 1$. Remember each carbon atom has three nearest neighbor in honeycomb lattice. The nearest neighbor vectors for a carbon atom at site A are given by

$$\vec{n_1} = \frac{a}{\sqrt{3}}\hat{x}, \qquad \vec{n_2} = \frac{a}{\sqrt{3}}\left(-\frac{1}{2}\hat{x}+\frac{\sqrt{3}}{2}\hat{y}\right), \qquad \vec{n_3} = \frac{a}{\sqrt{3}}\left(-\frac{1}{2}\hat{x}-\frac{\sqrt{3}}{2}\hat{y}\right) \tag{2.8}$$

Then Eq. (2.7) can be written as

$$c_A\varepsilon_0 - c_B t \left[e^{i\vec{k}.\vec{n_1}} + e^{i\vec{k}.\vec{n_2}} + e^{i\vec{k}.\vec{n_3}} \right] = E c_A \tag{2.9}$$

Using Eq. (2.8)

$$c_A \varepsilon_0 - c_B t \left[e^{ik_x a/\sqrt{3}} + 2e^{-ik_x a/2\sqrt{3}} \cos\left(\frac{k_y a}{2}\right) \right] = E c_A \qquad (2.10)$$

Where t is nearest neighbor transfer integral defined as $t = -\langle \varphi_A(\vec{r})|H|\varphi_B(\vec{r} - \overrightarrow{n_l})\rangle$. The transfer integrals t is same for all three nearest neighbors due to the rotational symmetry of $2p_z$ orbitals about the z axis. Repeating similar steps for Eq. (2.5), we can write

$$c_B \varepsilon_0 - c_A t \left[e^{-ik_x a/\sqrt{3}} + 2e^{ik_x a/2\sqrt{3}} \cos\left(\frac{k_y a}{2}\right) \right] = E c_B \qquad (2.11)$$

Eq. (2.10) and (2.11) can be written in matrix form

$$\begin{pmatrix} \varepsilon_0 - E & -t\, f(k) \\ -tf(k)^* & \varepsilon_0 - E \end{pmatrix} \begin{pmatrix} c_A \\ c_B \end{pmatrix} = 0 \qquad (2.12)$$

where

$$f(k) = e^{ik_x a/\sqrt{3}} + 2e^{-ik_x a/2\sqrt{3}} \cos\left(\frac{k_y a}{2}\right) \qquad (2.13)$$

There is a non-trivial solution for c_A and c_B only when the matrix determinant equals zero. This condition gives

$$(\varepsilon_0 - E)^2 - t^2 \left[1 + 4\cos\left(\frac{k_y a}{2}\right)\cos\left(\frac{\sqrt{3}\,k_x a}{2}\right) + 4\cos^2\left(\frac{k_y a}{2}\right) \right] = 0 \qquad (2.14)$$

Solving for energy E and taking $\varepsilon_0 \to 0$ as reference energy, we have

$$E_\pm(\vec{k}) = \pm t \sqrt{1 + 4\cos\left(\frac{k_y a}{2}\right)\cos\left(\frac{\sqrt{3}\,k_x a}{2}\right) + 4\cos^2\left(\frac{k_y a}{2}\right)} \qquad (2.15)$$

The energy dispersion relation for graphene according to this formula is plotted in Fig. 2.1(c) for the entire region of the first BZ [3]. The upper half of the dispersion curve is the π^* anti-bonding band while the lower half is the π bonding band. There is an energy gap between the π and π^* bands along the BZ edge M-K, that becomes zero at the K points. The two bands are degenerate at the K and K` points where the dispersion vanishes ($E_\pm = 0$). The Fermi energy (E_F) level of intrinsic graphene is also situated at the connection

points of the two bands. Two electron per unit cell therefore completely fill the lower π band with spin up and spin down electrons, which leaves the upper π^* band empty.

The existence of zero band gap at the K and K` points comes from the fact that two carbon atoms at A and B sites in the primitive unit cell are equivalent to each other by symmetry. If AB lattice symmetry is broken somehow, the onsite energy would be different for sites A and B, and the dispersion would show an energy gap $E_g = (\varepsilon_{0A} - \varepsilon_{0B})$ between the π and π^* bands. For example, hexagonal boron nitride (h-BN) with B and N atoms in a honeycomb lattice at A and B sites have a band gap of $E_g = 3.5 \; eV$ at the K (K`) points [4].

2.1.2 Massless Dirac fermions

The electronic states near the Fermi level can be described by expanding the energy dispersion (Eq. 2.15) around the K and K` points. Introducing a relative wavevector $\vec{\Bbbk}$ measured from the K point, defined as

$$\vec{\Bbbk} = \left(\vec{k} - \vec{k}_K\right) \tag{2.16}$$

where

$$\vec{k}_K = \frac{2\pi}{a}\left(\frac{1}{3}\hat{x} + \frac{1}{\sqrt{3}}\hat{y}\right) \tag{2.17}$$

is the wavevector at the K points. Substituting $k_x = \left(\Bbbk_x + \frac{2\pi}{3a}\right)$ and $k_y = \left(\Bbbk_y + \frac{2\pi}{\sqrt{3}a}\right)$ in Eq. (2.13) and expanding $f\left(\vec{\Bbbk}\right)$ up to the first order in $\Bbbk$, we have

$$f\left(\vec{\Bbbk}\right) \approx \frac{\sqrt{3}}{2}a\left(\Bbbk_x - i\Bbbk_y\right) \tag{2.18}$$

Rewriting Eq. (2.12)

$$-\frac{\sqrt{3}}{2}a\,t\begin{pmatrix} \varepsilon_0 - E & \Bbbk_x - i\Bbbk_y \\ \Bbbk_x + i\Bbbk_y & \varepsilon_0 - E \end{pmatrix}\begin{pmatrix} c_A \\ c_B \end{pmatrix} = 0 \qquad (2.19)$$

Again taking $\varepsilon_0 \rightarrow 0$ as reference energy, the solution of this equation is

$$E_{\pm}(\vec{\Bbbk}) = \pm\frac{\sqrt{3}}{2}a\,t|\vec{\Bbbk}| = \pm\hbar v_f|\vec{\Bbbk}| \qquad (2.20)$$

where $v_f = \sqrt{3}at/2\,\hbar$ is the Fermi velocity of the π electrons, which is measured to be ~ 1.1×10^6 m/s [5]. Equation (2.20) shows that graphene has a linear energy dispersion relation in the vicinity of the K and K` points. Thus, the valence and conduction bands of graphene appear as two cones meeting at the K and the K` points, as shown in Fig. 2.1(d). As a consequence of the linear energy dispersion, the DOS of graphene is linear $[\rho(E) \propto E]$ and vanishes at zero energy. It is important to note that low energy linear dispersion results holds up to $\pm 1eV$, and valid even when the next nearest neighbors are taken into account in the tight binding approximation [6].

In the effective mass approximation, the Hamiltonian in the vicinity of the K point is

$$\mathcal{H}_0(\vec{\Bbbk}) = \hbar v_f\begin{pmatrix} 0 & \Bbbk_x - i\Bbbk_y \\ \Bbbk_x + i\Bbbk_y & 0 \end{pmatrix} = \hbar v_f(\vec{\sigma}.\vec{\Bbbk}) \qquad (2.21)$$

where $\vec{\sigma} = (\sigma_x, \sigma_y)$ are the Pauli matrices. This Hamiltonian is analogous to the Dirac Hamiltonian for 2D massless neutrinos, where the electron Fermi velocity v_f is substituted for the speed of light. Thus, the low energy electrons in graphene mimic relativistic particles with zero rest mass and a constant velocity $v_f \approx c/300$ (rather than the speed of light c). Because of this unique behavior, charge carriers in graphene are known as "massless Dirac fermions", and the K and K` points are termed as "Dirac points". This ultra- relativistic nature of charge carriers in graphene leads to a number of interesting observations such as room temperature quantum Hall effect [7] and Klein tunneling [8].

2.1.3 Pseudospin

The sublattice symmetry of graphene also leads to the concept of pseudospin. Let's define

an angle $\theta_{\Bbbk}$ between the $\Bbbk$ vector and the $\Bbbk_y$ axis, then $\Bbbk_x \pm i\Bbbk_y = i|\Bbbk|e^{\mp i\theta_{\Bbbk}}$. After

substituting these values in Eq. (2.19), and solving for eigenvectors of the massless Dirac

Hamiltonian at the K point, we have

$$\binom{c_A}{c_B} = |\Bbbk\rangle = \frac{1}{\sqrt{2}} e^{i\vec{\Bbbk}\cdot\vec{r}} \begin{pmatrix} -i\, s\, e^{-i\theta_{\Bbbk}/2} \\ e^{i\theta_{\Bbbk}/2} \end{pmatrix} \tag{2.22}$$

where $s = +1(-1)$ corresponds to the states above(below) the K point. Here, the $e^{i\vec{\Bbbk}\cdot\vec{r}}$

term is simply a plane wave but the second term, $\left(|S_p\rangle = e^{-i\vec{\Bbbk}\cdot\vec{r}}|\Bbbk\rangle\right)$, is a vector whose

top and bottom components give the relative amplitude of the electronic wave function on

the A and B sublattice. The vector $|S_p\rangle$ can be obtained from an initial state $|S_p{}^0\rangle$ by a

rotation operation around the $\hat{z}$ axis, i.e. $|S_p\rangle = R(\theta_{\Bbbk})|S_p{}^0\rangle$, where $R(\theta)$ is a spin ½

rotation operator, given by

$$R(\theta) = exp\left(-i\frac{\theta}{2}\,\sigma_z\right) = \begin{pmatrix} e^{-i\theta/2} & 0 \\ 0 & e^{+i\theta/2} \end{pmatrix} \tag{2.23}$$

and

$$|S_p{}^0\rangle = \frac{1}{\sqrt{2}}\binom{-i\,s}{1} \tag{2.24}$$

This rotation operation resembles that of a two component spinor describing electron spin,

but arising from the sublattice symmetry of graphene. Therefore, this vector $|S_p\rangle$ is often

called the "pseudospin" of massless Dirac fermions, in contrast to real spin. The orientation

of the pseudospin is tied to the direction of the $\Bbbk$ vector, analogous to the real spin of

massless fermions which points along the direction of propagation. For the upper

cone ($s = +1$), the pseudospin is parallel to $\vec{\Bbbk}$ and states near the K point correspond to

right-handed Dirac fermions, whereas for the lower cone ($s = -1$), the pseudospin is antiparallel to $\vec{k}$ and states correspond to left-handed Dirac anti-fermions. Thus, charge carriers in the conduction and valence bands have opposite chirality. This situation is reversed for the K` Points, thus the charge carriers have opposite chirality in the K and K` valleys.

As a consequence of the chiral fermions each scattering process is described by a corresponding spin rotation. This has important implications on the electronic transport in graphene such as the suppression of backscattering and a non-trivial Berry phase [9, 10]. A backscattering process (particles scatter from $\vec{k}$ to $-\vec{k}$) can be described by rotating $|k\rangle$ by the rotation operator $R(\pi)$. For a potential $V(\vec{r})$ with a range larger than the lattice constant in graphene (no inter-valley scattering), the resulting matrix element between the two states is given by [11]

$$\langle -\vec{k}|V(\vec{r})|\vec{k}\rangle \approx V\left(\vec{k} - \left(-\vec{k}\right)\right)\langle \vec{k}|R(\pi)|\vec{k}\rangle \tag{2.25}$$

Note that a π rotation of a certain $\vec{k}$ state always produces an orthogonal state to the original one, so the overlap matrix element vanishes and completely suppresses the backscattering. The Berry phase is a phase change acquired by a wavefunction due to adiabatic rotation of the wavevector $\vec{k}$ around the origin as a function of time. Graphene has a non-trivial Berry phase due to the phase difference of π between the wave functions at the K and K` points, which stems from 2π rotation of the pseudospin vector between the scattering processes from two points because $R(2\pi) = e^{i\pi}$.

2.2 Spin orbit coupling

In the previous section, the low energy π bands of graphene were described by the 2D Dirac Hamiltonian with linear energy dispersion without considering the electron spin. The π and π^* bands are degenerate at the Dirac points. However, when the spin degree of freedom is included, the two bands become four fold degenerate at the Dirac points [Fig. 2.2(a)]. When the interaction between the orbital and spin degrees of freedom is also considered, the effective Hamiltonian takes the form [12, 13]

$$\mathcal{H} = \mathcal{H}_0 + \mathcal{H}_{SOC} \tag{2.26}$$

where $\mathcal{H}_0$ is the 2D Dirac Hamiltonian given by Eq. (2.21), and $\mathcal{H}_{SOC}$ is the Hamiltonian due to SOC in graphene. Two different spin orbit terms have been considered in graphene in the vicinity of the Dirac points: intrinsic and Rashba [13, 14].

The intrinsic SOC in graphene lifts the orbital degeneracy at the Dirac point and induces a spin orbit gap between the valence and conduction bands as shown in Fig. 2.2(b) [15, 16]. Electrons acquire finite mass and consequently the two bands become parabolic, while preserving their spin degeneracy. The Hamiltonian for the intrinsic SOC of graphene is given by [13]

$$\mathcal{H}_{SO} = \lambda_{SO}\tau_z\sigma_z S_z \tag{2.27}$$

where λ_{SO} is intrinsic SOC parameter, τ_z is +1 and -1 for the K and K` points respectively, σ_z is the pseudospin Pauli matrix and S_z is the real spin Pauli matrix. The magnitude of the spin orbit gap is $\Delta_{SOC} = 2\lambda_{SO}$, which has been estimated to be ~ 1 μeV by considering the mixing of only σ and π bands in the tight binding approximation [13, 15]. However, first principle calculations predict the gap value to be 24 μeV with the d orbital contribution

[16]. Direct experimental observation of this extremely small spin orbit gap is challenging, because it should only be observable at a temperature below ~ 0.01 K.

The Rashba SOC appears only when inversion symmetry of the graphene plane is broken, either by a perpendicular electric field or by interactions with the substrate [14, 15]. The Rashba interaction lifts the spin degeneracy of the pristine graphene energy bands. The Hamiltonian for the Rashba interaction is given by [13]

$$\mathcal{H}_R = \lambda_R\big(\tau_z \sigma_x S_y - \sigma_y S_x\big) \tag{2.28}$$

where λ_R is the Rashba coupling parameter. As a result of Rashba coupling, each parabolic band splits into two with their energies differing by $2\lambda_R$ at a given momentum [Fig. 2.2(c)]. Unlike the conventional two dimensional electron gas (2DEG), the Rashba splitting in graphene does not depend on momentum, but it is proportional to the Fermi velocity of the massless Dirac fermions. The Rashba spin orbit strength is estimated to be ~ 10 μeV per 1V/nm of external electric field, which mainly comes from hybridization of the σ and π bands [13, 16].

The band structure topology of graphene depends on the relative strength of the intrinsic and Rashba spin orbit interactions. When the Rashba interaction is negligible, $\lambda_{SO} \gg \lambda_R$, Kane and Mele predicted that the intrinsic SOC generates an energy gap in graphene and converts it to a quantum spin Hall insulator from a zero gap semiconductor [12]. This novel electronic state of matter has gapless edge states that support spin and charge transport at the graphene edges. When the intrinsic and Rashba coupling are equal at a certain electric field, $\lambda_{SO} \approx \lambda_R$, then two bands form Dirac cones with no energy gap and the remaining two show a spin orbit gap with parabolic dispersion [16, 17]. When Rashba coupling dominates, $\lambda_R \gg \lambda_{SO}$, all the bands are parabolic with one

electron and one hole band being degenerate [16, 17]. The spin orbit gap closes and

graphene becomes zero gap semiconductor with parabolic dispersion.

References

1. R. Saito, G. Dresselhaus and M. S. Dresselhaus. Physical Properties of Carbon Nanotubes. Imperial College Press, London (1998).

2. P. R. Wallace *et al.* The band theory of graphite. *Phys. Rev.* **71,** 622 (1947).

3. A. H. Castro Neto, F. Guinea, N. M. R. Peres, K. S. Novoselov and A. K. Geim. The electronic properties of graphene. *Rev. Mod. Phys.* **109**, 81 (2009).

4. A. Jario, R. Satio, G. Dresselhaus and M. S. Dresselhaus. Raman spectroscopy in graphene related systems. WILEY-VCH Verlag GmbH & Co. KGaA (2011).

5. K. S. Novesolev *et al.* Two dimensional gas of massless Dirac fermions in graphene. *Nature* **438,** 197 (2005).

6. S. Reich, J. Maultzsch and C. Thomsen. Tight binding description of graphene. *Phys. Rev. B* **66,** 035412 (2002).

7. K. S. Novoselev *et al.* Room temperature quantum Hall effect in graphene. *Science* **315,** 1379 (2007).

8. N. Stander, B. Huard and D. Goldhaber-Gordon. Evidence for Klein tunneling in graphene p-n junction. *Phys. Rev. Lett.* **102,** 026807 (2009).

9. T. Ando, T. Nakanishi, R. Satio. Berry's phase and absence of backscattering in carbon nanotubes. *J. Phys. Soc. Jpn.* **67,** 2857 (1998).

10. Y. Zhang, Y-W. Tan, H. L. Stormer and P. Kim. Experimental observation of quantum Hall effect and Berry's phase in graphene. *Nature* **438,** 201 (2005).

11. H. Aoki and M. S. Dresselhaus. Physics of Graphene. Springer international publishing, Switzerland (2014).

12. C. L. Kane and E. J. Mele. Quantum spin Hall Effect in graphene. *Phys. Rev. Lett.* **95,** 226801 (2005).

13. H. Min, J. E. Hill, N. A. Sinitsyn, B. R. Sahu, L. Kleinman and A. H. MacDonald. Intrinsic and Rashba spin-orbit interaction in graphene sheets. *Phys. Rev. B* **74,** 165310 (2006).

14. E. I. Rashba. Properties of semiconductor with an extremum loop.1.Cyolotron and combinational resonance in a magnetic field perpendicular to the plane of the loop. *Sov. Phys. Solid. State* **2,** 1109 (1960).

15. Y. Yao, F. Ye, X. L. Qi, S. C. Zhang and Z. Fang. Spin-orbit gap of graphene: First principles calculations. *Phys. Rev. B* **75,** 041401 (2007).

16. M. Gmitra, S. Konschuh, C. Ertler, C. A. Draxl and J. Fabian. Band structure topologies of graphene: Spin orbit coupling effect from first principles. *Phys. Rev. B* **80,** 235431 (2009).

17. W. Han, R. K. Kawakami, M. Gmitra and J. Fabian. Graphene spinotronics. *Nat. Nanotechnl.* **9,** 794 (2014).
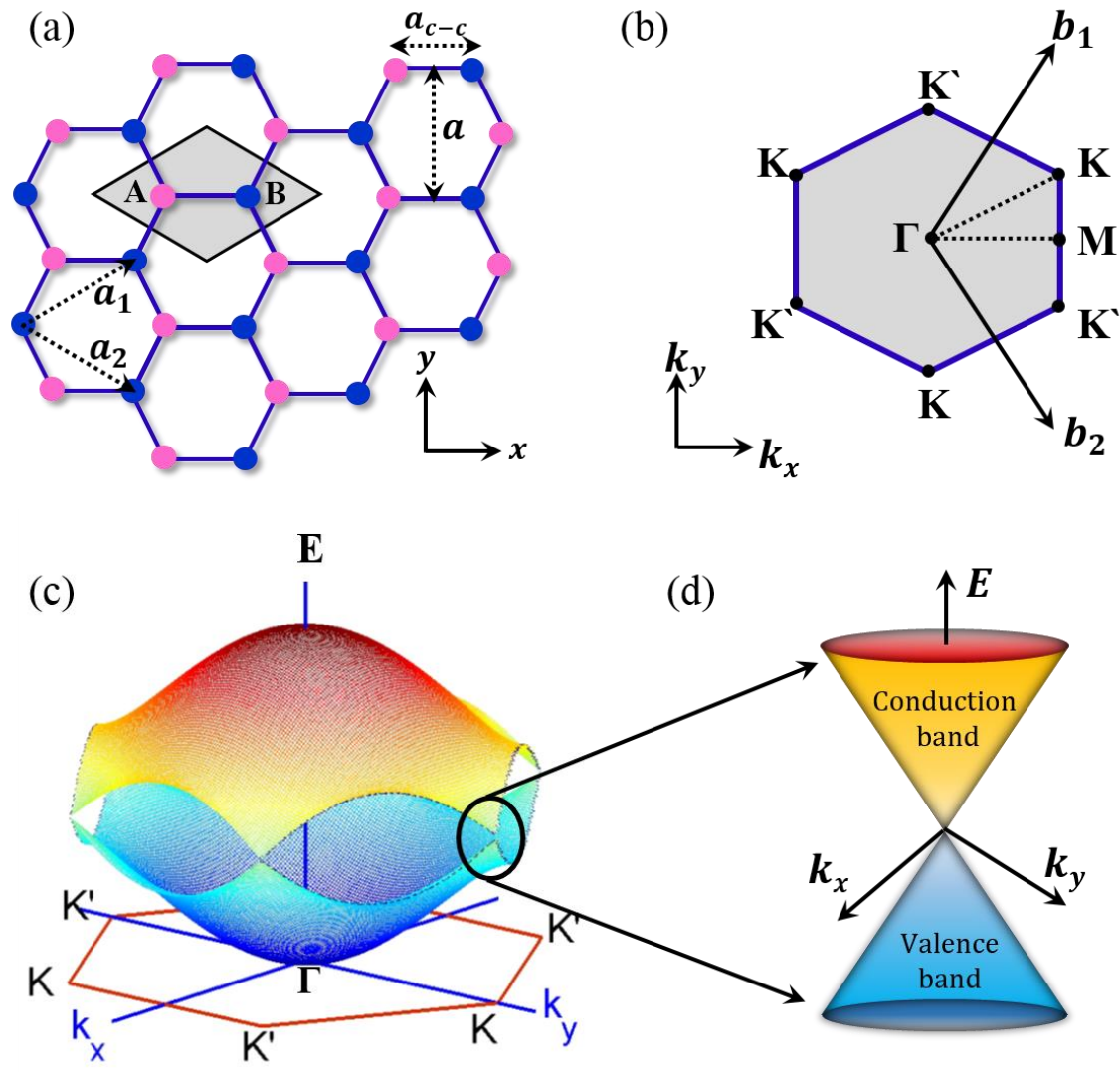
Figure 2.1: (a) Schematic of the graphene hexagonal lattice where pink and blue dots represent carbon atoms at A and B sites, respectively. The shaded diamond shape corresponds to the primitive unit cell with unit vectors $\vec{a_1}$ and $\vec{a_2}$. (b) First BZ of monolayer graphene where high symmetry points are marked by the black dots. $\vec{b_1}$ and $\vec{b_2}$ are the reciprocal lattice vectors. (c) The energy dispersion relation of graphene in the first BZ obtained from nearest neighbor tight binding model. (d) Close up view of low energy dispersion at one of the K points exhibiting linear dispersion and zero band gap.
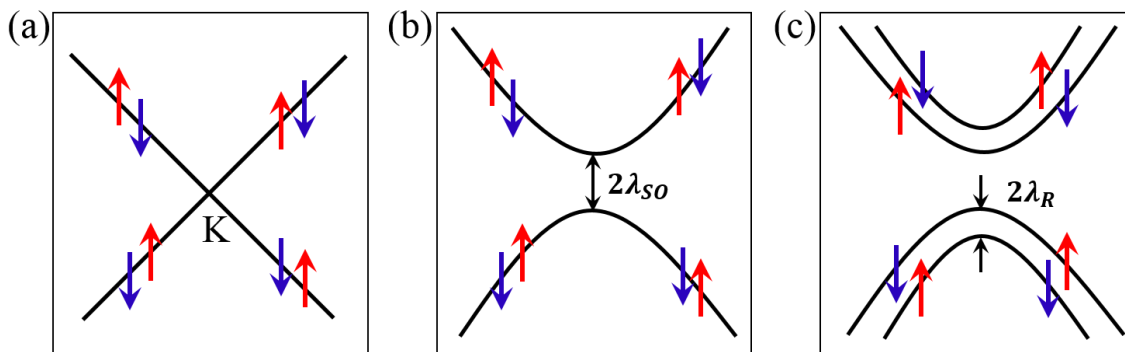
Figure 2.2: Schematic of the band structure of graphene (a) when SOC is neglected, two Dirac cones touch each other at the K and K` points. (b) When intrinsic SOC is included, the Dirac cones become parabolic bands that are spin degenerate and separated by a spin orbit gap. (c) When inversion symmetry is broken, Rashba coupling lifts the spin degeneracy of graphene bands. Here red and blue arrows represent up and down electron spins, respectively

Chapter 3
Material Synthesis

This chapter summarizes experimental methods used to prepare graphene heterojunctions studied in this dissertation. Section 3.1 provides details of graphene synthesis. Section 3.2 describes graphene transfer methods for the fabrication of these heterojunctions.

3.1   Graphene synthesis

Graphene was first isolated from graphite in 2004 by mechanical exfoliation using scotch tape [1]. Since then many new ways of synthesizing graphene have been developed such as chemical exfoliation of graphite [2], reduction of graphene oxide [3], thermal decomposition of SiC [4, 5] , and CVD on a transitional metal substrate [6, 7]. Mechanical exfoliation produces the best quality graphene, but sample uniformity, size and location are largely uncontrollable. Whereas, chemical exfoliation introduces structural and electronic disorders in graphene. Thermal decomposition of SiC provides high quality wafer scale epitaxial graphene [5]. Growing graphene via CVD is the most popular method as it produces large area graphene and subsequent etching of the metal substrate allows the transfer of graphene onto an arbitrary substrate [6-8]. We used both epitaxial and CVD graphene in this dissertation, and this section provides details of the two growth processes.

3.1.1 Epitaxial graphene growth

SiC is a wide band gap semiconductor (~3 eV), occurring in many different crystal structures called polytypes. The most commonly available polytypes are 3C, 2H, 4H and

6H, where letters "C' and "H" denote the cubic and hexagonal crystal structures, respectively, and the numbers refer to the number of Si-C double atomic layers in one repeating unit along c-axis. As shown in Fig. 3.1(a), the stacking sequence of three types of Si-C double atomic layers A, B and C defines the crystal structure for various polytypes, e.g. 6H-SiC has a stacking sequence of ABCACB. Furthermore, for a hexagonal SiC single crystal, the (0001) Si-face and (000$\bar{1}$) C-face are terminated by a layer of Si and C atoms, respectively [Fig. 3.1(b)]. Due to the polar nature of Si-C bonds, hexagonal SiC crystals also exhibit an intrinsic polarization, which is opposite for the Si and C-terminated surfaces of SiC.

Epitaxial graphene can be grown by heating the 4H- or 6H-SiC crystals either in UHV [4, 9] or under Ar atmosphere in a furnace [5]. Thermal decomposition of SiC initiates with Si desorption, and liberated C atoms form graphene layers on the surface.

$$SiC \xrightarrow{1300\ ^0C} Si(\uparrow) + C \qquad (3.1)$$

This method is the most promising route to produce wafer sized graphene directly on a semi-conducting substrate.

The growth mechanism and electronic properties of epitaxial graphene grown on Si- and C-face of SiC are significantly different [10]. On Si-face SiC, graphene is epitaxial with a 30° rotation relative to the substrate [11]. Earlier studies have shown that graphitization starts with a warped interface layer having a (6√3 × 6√3) structure which remains at the interface during subsequent layer growth [4, 11]. The interface layer plays a critical role in growth kinetics and limits the graphene growth to only few layers (normally < 3 layers). While on C- face SiC, the absence of an ordered interface layer results in growth of multilayer graphene (typically > 10 layers) with rotational disorder

[12, 13]. Due to the lack of control of number of graphene layers on C-face SiC, we primarily worked with Si-face SiC to grow epitaxial graphene in this dissertation.

3.1.1.1   SiC surface preparation

Our experiments are carried out on nitrogen doped 6H-Si-SiC and 4H-C-SiC substrates (Cree Inc.). As received SiC wafers typically have a very rough surface due to polishing damages. Figure 3.2(a) shows an atomic force microscope (AFM) image of as received SiC, exhibiting random scratches of ~10 nm in depth. To remove these scratches, SiC substrates are etched at 1600 ℃ in an H_2/Ar atmosphere [14]. In this process, a SiC substrate is placed on a molybdenum (Mo) boat inside the etching chamber after ultrasonic cleaning in acetone and methanol. Ar gas is used to purge the chamber first then followed by H_2 gas flow with a ratio of 2:1 for Ar:H_2 mixture. Then current is passed through the Mo boat to heat the SiC substrate. The SiC substrate is kept at ~ 1600 ℃ for 15 minutes and then allowed to cool down slowly in presence of Ar gas. At higher temperature, SiC reacts with H_2 gas according to the following reaction

$$2SiC + 5H_2(\uparrow) \xrightarrow{1600\ ^0C} 2SiH_4(\uparrow) + 2C_2H_2(\uparrow) \tag{3.2}$$
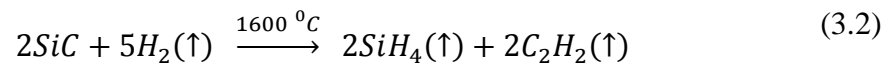
The hydrogen etching treatment of SiC results in an atomically flat step terrace morphology as shown in Fig. 3.2(b). Average step height is ~1.4 nm corresponding to approximately six Si-C bilayers, and the terrace size is ~ 0.45 μm. This process further saturates the surface dangling bonds and leads to a chemically inert surface likely terminated with hydrogen or silicates [15, 16], which protects the SiC surface from oxidation. Similar surface treatment is used to prepare the SiC substrates for graphene transfer.

3.1.1.2   Graphene growth on Si-face SiC

A hydrogen etched Si-face SiC substrate is loaded into a UHV chamber and degassed at 600 ℃ for a couple of hours. Then the SiC is annealed at 950 ℃ for 15 minutes in the presence of Si flux to produce a (3×3) reconstructed surface, and finally temperature is ramped up to ~ 1300 ℃ for another 15 minutes to grow graphene. The sample is annealed by using direct current heating and the temperature is measured by an infrared pyrometer. The number of graphene layers can be controlled by the growth temperature and time. Annealing of the SiC substrate at higher temperature for longer time results in the growth of multi-layer graphene (up to three). A typical image of UHV grown epitaxial graphene is shown in Fig. 3.2(c). Due to the preferential desorption of Si atoms from the step edges, pits are commonly form there. However, graphene growth is continuous over the SiC step edges. Graphene grows with reduced pit density if the Si desorption rate is suppressed by supplying additional Si from external source during the growth [17].

There is strong interaction between the interfacial layer and the Si-SiC substrate [18], as it is partially bonded to the Si dangling bonds at the interface [Fig. 3.2(d)]. In addition, epitaxial graphene typically exhibits electron doping due to charge transfer from the Si dangling bonds at the interface [19]. In order to reduce the influence of the SiC on the electronic properties of graphene, it is desirable to decouple the graphene layers from the SiC substrate, producing quasi-free standing (QFS) graphene. This can be done by saturating the Si dangling bonds by hydrogen intercalation at the interface [20], which turns the interface and the first graphene layer into first and second QFS graphene layers, respectively, as shown in Fig. 3.2(e). To prepare a hydrogen intercalated graphene sample,

epitaxial graphene/SiC is taken out from UHV and annealed at ~ 800 ^{o}C in H$_2$ gas at atmospheric pressure.

3.1.2 CVD graphene growth

Graphene is grown on transition metal substrates via CVD by thermal decomposition of hydrocarbon gases on the surface. The metallic substrates work as a catalysts during the growth and determine the quality of graphene. CVD graphene has been synthesized on a number of substrates, such as Pt, Pd, Ru, Ir, Ni and Cu [6, 7, 21-25]. In particular, graphene growth on Ni and Cu has been studied extensively as these substrates are relatively inexpensive. Nevertheless, growth mechanisms on Ni and Cu substrates are quite different [6, 26].

On a polycrystalline Ni substrate, CVD graphene grows in a two-step process. First, carbon atoms incorporate into bulk of the Ni substrate at high temperature (> 800 ^{o}C) due to a high solubility of carbon in Ni. Then during the cooling down, carbon atoms diffuse out onto Ni surface and precipitate to form graphene [Fig. 3.3(a)]. The precipitation process preferentially takes place at grain boundaries of the polycrystalline Ni substrate, and results in multilayer graphene growth near the boundaries compared to within the grains [8]. In general, graphene growth on the Ni substrate is inhomogeneous due to the lack of control of number of graphene layers.

On the other hand, CVD graphene growth on polycrystalline Cu substrate is mostly uniform monolayer over large areas. Due to low carbon solubility in Cu, graphene growth on Cu is a surface adsorption process rather than a precipitation process [26]. Hydrocarbon gases catalytically decompose on the Cu surface and led to random nucleation of graphene as shown in Fig. 3.3(b). These initial graphene island may have different lattice orientations

depending on the underneath Cu grains. As growth continues, the graphene domains increase in size and eventually coalesce into a continuous graphene film. Weak interaction between graphene and Cu allows the graphene grains to expand over the grain boundaries of Cu with minimum structural disruption [27]. Once monolayer graphene covers the Cu surface completely, there is no catalyst available to promote the decomposition of the hydrocarbons and further graphene growth. Thus, graphene growth on the Cu substrate is a self-limiting process.

3.1.2.1 CVD graphene growth on Cu foil

In this dissertation, we fabricate graphene heterojunctions using monolayer CVD graphene produced in our lab, as well as commercially available ones from Graphene Supermarket Inc. and Graphene Platform Inc. Details of our CVD growth on Cu foil are provided below.

Graphene growth is performed in a high pressure hot wall furnace with 2" diameter quartz tube. A schematic of the complete growth system is shown in Fig. 3.3(c). A high purity 25μm thick Cu foil is cut into small piece $\sim 1 \times 1$ cm^2 and cleaned with acetone and methanol. Solvent cleaning is necessary to remove thin layer of grease or organic impurities that may be present on the surface of as received Cu foil. The Cu foil is then placed inside the quartz tube and tube is pumped down to $\sim 10^{-1}$ Torr using a mechanical pump. The tube is flushed with Ar/ H$_2$ gas for 20-30 minutes to purge as much oxygen and water vapor as possible. Ar and H$_2$ gases are flowed throughout the growth process with flow rates of 500 and 10 standard cubic centimeters per minute (SCCM), respectively. Flow rates of the gases are regulated by individual mass flow controllers.

After purging the tube, the temperature of the furnace is ramped up to 900 $^{\circ}$C and the Cu foil is annealed for 20 minutes in an Ar and H$_2$ atmosphere. This pretreatment of

the Cu foil is important to remove the native copper oxide layer from the surface, which can reduce its catalytic activity. Annealing in an H_2 atmosphere also increases the grain size of the polycrystalline Cu foil [28], which reduces the effect of the Cu grain boundaries on graphene growth. After that, 7 SCCM of ethylene (C_2H_4) gas is introduced in the system for 10 minutes while keeping the furnace temperature at 900 ^{o}C. The furnace is then turned off and system is allowed to cool down naturally with Ar and H_2 gas flowing. Once the system is below 300 ^{o}C, H_2 gas can be turned off and the furnace lid can be opened for fast cooling of the tube down to room temperature. The Cu foil can be taken out of the quartz tube after its temperature has reached room temperature.

Graphene grows on both the sides of Cu foil during the CVD process. A scanning electron microscopy (SEM) image of monolayer CVD graphene grown on Cu is shown in Fig. 3.3(d). In this image graphene completely covers the Cu surface and long bright features (one marked by an arrow) corresponds to graphene ridges that form due to the difference in the thermal expansion coefficients of graphene and Cu ($\alpha_{graphene} = -6 \times 10^{-6} /K$ and $\alpha_{Cu} = 24 \times 10^{-6} /K$) [27]. During the cool down process after the growth, graphene expands while Cu substrate shrinks due to the negative and positive thermal expansion coefficients, respectively. As a result, graphene bulges up and forms ridges to relieve the compressive strain [28, 29].

3.2 Graphene transfer onto arbitrary substrates

One of the unique aspects of graphene is that its properties largely depends on the underlying substrate. Therefore, substrate engineering is a viable route to alter the electronic properties of graphene without modifying its structural properties [30, 31]. Since

direct growth of graphene is limited to only few substrates, one must be able to transfer the synthesized graphene onto a variety of desirable substrates to fully utilize its remarkable properties.

There are mainly two types of graphene transfer processes described in the literature, mechanical exfoliation [32, 33] and polymer assisted transfer process [34-36]. In the mechanical exfoliation process, graphene flakes can be obtained by using the scotch tape, thermal release tape or pre-patterned polydimethylsiloxane (PDMS) stamps, and then placed directly onto an arbitrary substrate. But this process results in a non-uniform graphene transfer with only ~ μm size flakes. On the other hand, polymer assisted transfer is more involved with multiple steps, but exactly replicates size and position of graphene flakes from source substrates [36], and also suitable to transfer large area graphene (on inches scale). To transfer large area monolayer graphene onto an arbitrary substrate, CVD graphene on Cu foil is the choice of material to start with. Epitaxial graphene grown on SiC is difficult to transfer due to resistance of SiC to chemical etching. Although epitaxial graphene on SiC can be peeled off using thermal release tape, but results in a defected transfer due to the strong interaction between graphene and SiC [32].

In this work, we used the polymer assisted process to transfer large area monolayer CVD graphene from Cu foil onto a variety of substrates such as SiC, Si, GaAs and Bi_2Se_3. A schematic of the transfer process is shown in Fig. 3.4(a). The first step is to cut a piece of Cu foil of desirable size. Remember graphene grows on both sides of the Cu foil during CVD. A layer of polymethyl methacrylate (PMMA) is spin coated (3000 rpm for 45 sec) on graphene on one side of the Cu foil. Optimized thickness for the PMMA layer is ~ 300nm, a thinner polymer layer does not support graphene perfectly and too thick layer is

hard to remove at the end of the process. The PMMA is then hardened by annealing the Cu foil at 135 ºC for 10 minutes on a hot plate.

In the next step, the Cu foil with the PMMA side on top is placed in an ammonium persulfate Cu etchant solution. Due to the hydrophilic nature of PMMA, Cu foil floats on the surface of the solution. In some reports, it is recommended to etch off the bottom graphene using oxygen plasma, prior to placing the Cu foil in the etchant. But we believe that when the Cu starts to etch from the edges, the bottom graphene layer gradually detaches from the Cu surface and drops off in the solution. After few hours, when Cu is etched away completely, a transparent PMMA/graphene stack floats on the surface. To wash off the Cu etchant residues from the bottom surface of graphene, the PMMA/graphene is then rinsed with deionized (DI) water a couple of times. To further clean the remaining metal residues, the PMMA/graphene film is transferred to a cleaning solution bath of 1:1:10 $HCl/H_2O_2/H_2O$ for 15 minutes at room temperature. Afterwards the film is again rinsed with DI water a couple of times.

The floating PMMA/graphene film in DI water is scooped out directly onto a desirable substrate, and allowed to dry in air for overnight (~ 12 hours). Small gaps could form between the graphene and the substrate due to trapped water at the interface. The imperfect contact of graphene with substrate can cause cracks and tears when the polymer material is removed. By annealing the substrate at 135 ºC for 10 minutes, the PMMA layer softens and becomes more flexible. This heat treatment step increases adhesion between the graphene and the substrate and improves the quality of the transferred graphene.

In the last step, the top PMMA layer is removed by solvent, leaving the graphene on the substrate. Typically, PMMA is dissolved by submerging the substrate either in

acetone or dichloromethane for couple of hours at 70 ºC. After taking out the sample from the polymer etchant, it is washed by ethyl alcohol and DI water to remove the polymer etchant residues. An optical microscope image of CVD graphene transferred onto a SiO_2 substrate is shown in Fig. 3.4(b). Monolayer graphene has a light pink color contrast compared to the SiO_2 substrate. The color contrast increases as number of graphene layer increases as evident in the image due to the folding of graphene layer. Nevertheless, the visibility of graphene on SiO_2 substrate strongly depends on the SiO_2 thickness and the wavelength of light. For a 550 nm light, graphene optical contrast is a maximum onto 90 nm and 285 nm thick SiO_2.

Dissolving the PMMA layer often leaves polymer residues on the graphene surface, which are not visible in optical microscope. A further annealing of the sample in vacuum at 300 ºC in presence of Ar/H_2 gases is very helpful to obtain a clean graphene surface [37]. Figure 3.4(c) is an AFM image of monolayer graphene, transferred onto a SiO_2 substrate and then annealed in Ar/H_2 atmosphere for three hours, exhibiting clean transfer. Graphene is continuous all over the surface except a minor crack that is marked by an arrow. The network of long white features in the image correspond to graphene ridges [29], those were formed during the CVD growth and preserved in the graphene transfer process.

References

1. K. S. Novoselov *et al.* Electric field effect in atomically thin carbon films. *Science* **306**, 666 (2004).

2. S. Stankovich *et al.* Graphene based composite materials. *Nature* **442,** 282 (2006)

3. G. Eda, G. Fanchini and M. Chhowalla. Large-area ultrathin films of reduced graphene oxide as a transparent and flexible electronic material. *Nat. Nanotechnol.* **3,** 270 (2008).

4. C. Reidl, U. Starke, J. Bernhardt, M. Franke and K. Heinz. Structural properties of graphene-SiC(0001) interface as a key for the preparation of homogeneous large terrace graphene surfaces. *Phys. Rev. B* **76**, 245406 (2007).

5. K. V. Emtsev *et al.* Towards wafer-size graphene layers by atmospheric pressure graphitization of silicon carbide. *Nat. Maters.* **8,** 203 (2009).

6. X. Li *et al.* Large-area synthesis of high-quality and uniform graphene films on copper foils. *Science* **324,** 1312 (2009).

7. S. Bae *et al.* Roll-to-roll production of 30-inch graphene films for transparent electrodes. *Nat. Nanotechnol.* **5,** 574 (2010).

8. A. Reina *et al.* Large area few layer graphene films on arbitrary substrates by chemical vapor deposition. *Nano Lett.* **9,** 30 (2009).

9. Y. Qi, S. H. Rhim, G. F. Sun, M. Weinert and L. Li. Epitaxial graphene on SiC (0001): More than just honeycombs. *Phys. Rev. Lett.* **105,** 085502 (2010).

10. K. V. Emtsev, F. Speck, Th. Seyller and L. Ley. Interaction, growth and ordering of epitaxial graphene on SiC surfaces: A comparative photoelectron spectroscopy study. *Phys. Rev. B* **77,** 155303 (2008).

11. A. J. van Bommel, J. E. Crombeen and A. van Tooren. LEED and Auger electron observation of the SiC(0001) surface. *Surf. Sci.* **48,** 463 (1975).

12. I. Forbeaux, J-M Themlin and J-M Debever. High temperature graphitization of 6H-SiC(000$\bar{1}$) face. *Surf. Sci.* **442,** 9 (1999).

13. J. Hass *et al.* Why multilayer graphene on 4H-SiC(000$\bar{1}$) behaves like single sheet of graphene. *Phys. Rev. Lett.* **100,** 125504 (2008).

14. S. Dogan, *et al.* The effect of H_2 etching on 6H-SiC studied by temperature dependent current voltage and atomic force microscopy. *Appl. Phys. Lett.* **85**, 1547 (2004).

15. N. Sieber, B. F. Mantel, T. H. Seyller, J. Ristein and J. Ley. Electronic and chemical passivation of hexagonal 6H-SiC surfaces by hydrogen termination. *Appl. Phys. Lett.* **78**, 1216 (2001).

16. U. Starke, J. Schardt, J. Bernhardt and K. Heinz. Reconstructed oxide structure stable in air: Silicate monolayers on hexagonal SiC surfaces. *J. Vac. Sci. Technol. A* **17,** 1688 (1999).

17. G. F. Sun, Y. Liu, S. H. Rhim, J. F. Jia, Q. K. Que, M. Weinert and L. Li. Si diffusion path for pit free graphene growth on SiC(0001). *Phys. Rev. B* **84,** 195455 (2011).

18. A. Bostwick *et al.* Symmetry breaking in few layer graphene films. *N. J. Phys.* **9,** 1 (2007).

19. P. Lauffer, K. V. Emtsev, R. Graupner, Th. Seyller and L. Ley. Atomic and electronic structure of few layer graphene on SiC(0001) studied by scanning tunneling microscopy and spectroscopy. *Phys. Rev. B* **77,** 155426 (2008).

20. C. Reidl, C. Coletti, T. Iwasaki, A. A. Zakharov and U. Starke. Quasi-free standing epitaxial graphene on SiC obtained by H_2 intercalation. *Phys. Rev. Lett.* **103,** 246804 (2009).

21. T. A. Land, T. Michely, R. J. Behm, J. C. Hamminger and G. Comsa. STM investigation of single layer graphite structures produced on Pt(111) by hydrocarbon decomposition. *Surf. Sci.* **264,** 261 (1992).

22. J. C. Hamilton and J. M. Blakely. Carbon segregation to single crystal surface of Pt, Pd and Co. *Surf. Sci.* **91,** 199 (1980).

23. P. W. Sutter, J. I. Flege and E. A. Sutter. Epitaxial graphene on ruthenium. *Nat. Mater.* **7,** 406 (2008).

24. J. Coraux, A. T. N. Diaye, C. Busse and T. Michely. Structural coherency of graphene on Ir(111). *Nano Lett.* **8,** 565 (2008).

25. A. N. Obraztsov, E. A. Obraztsova, A. V. Turnina and A. A. Zolotukhin. Chemical vapor deposition of thin graphite films of nanometer thickness. *Carbon* **45,** 2017 (2007).

26. X. Li, W. Cai, L. Colombo and R. S. Ruoff. Evolution of graphene grown on Ni and Cu by carbon isotope labeling. *Nano Lett.* **9,** 4268 (2009).

27. C. Mattevi, H. Kim and M. Chowalla. A review of chemical vapor deposition of graphen on copper. *J. Mat. Chem.* **21,** 3324 (2011).

28. W. Bao *et al.* Controlled ripple texturing of suspended graphene and ultrathin graphite membranes. *Nat. Nanotechnol.* **4,** 562 (2009).

29. G. F. Sun, J. F. jia, Q. K. Que and L. Li. Atomic-scale imaging and manipulation of ridges on epitaxial graphene on 6H-SiC(0001). *Nanotechnol.* **20,** 355701 (2009).

30. Y. Zheng, G. X. Ni, C. T. Toh, C. Y. Tan and B. Ozyilmaz. Graphene field effect transistor with ferroelectric gating. *Phys. Rev. Lett.* **2,** 011002 (2012).

31. S. Tongay, M. Lemaitre, X. Milao, B. Gila, B. R. Appleton and A. F. Hebard. Rectification at graphene semiconductor interfaces: Zero gap semiconductor based diodes. *Phys. Rev. X* **105,** 166602 (2010).

32. J. D. Caldwell *et al*. Technique for dry transfer of epitaxial graphene onto arbitrary substrates. *ACS Nano* **4,** 1108 (2010).

33. X. Liang, Z. Fu and S. Y. Chou. Graphene transistor fabricated via transfer printing in device active areas on large wafer. *Nano Lett.* **7,** 3840 (2007).

34. J. W. Suk *et al.* Transfer of CVD grown monolayer graphene onto arbitrary substrates. *ACS Nano* **5,** 6916 (2011).

35. X. Liang *et al.* Towards clean and crackles transfer of graphene. *ACS Nano* **5,** 9144 (2011).

36. A. Reina *et al.* Transferring and identification of single- and few-layer graphene on arbitrary substrates. *J. Phys. Chem. C* **112,** 17741 (2008).

37. A. Pirkle, J. Chan, A. Venugopal, D. Hinojos and C. W. Magnuson. The effect of chemical residues on the physical and electronic properties of chemical vapor deposited graphene transferred to SiO_2. *Appl. Phys. Lett.* **99,** 122108 (2011).
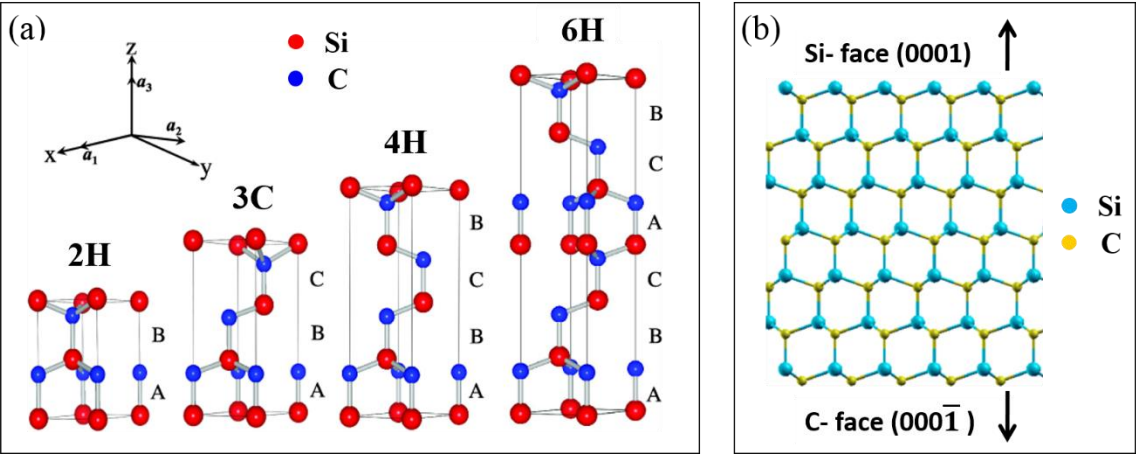
Figure 3.1: (a) Stacking sequences of most common SiC polytypes along the c-axis. The 2H-SiC is composed of only A and B type atomic layers and stacked as ABAB, while cubic 3C-SiC has ABC stacking. The 4H- and 6H-SiC unit cell is double and triple that of 2H with stacking sequences ABCB and ABCACB, respectively. (b) Schematic of a 6H-SiC crystal showing two different surface termination: Si-face in (0001) and C-face in (000$\bar{1}$) direction.
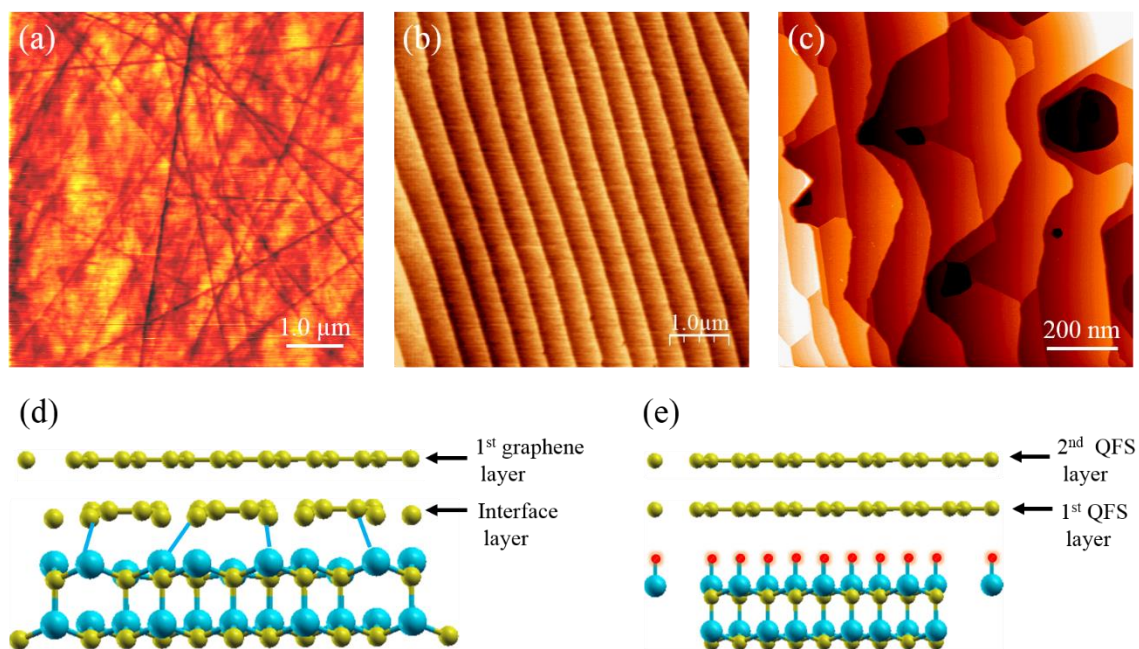
Figure 3.2: AFM images of (a) as received 6H-SiC(0001) which exhibits deep and random scratches on the surface and (b) 6H-SiC(0001) substrate after hydrogen etching shows atomically flat step terrace morphology. (c) STM image of epitaxial graphene grown on 6H-SiC(0001) in UHV. Schematic of (d) as grown epitaxial graphene where the interface layer is partially bonded to SiC and (e) hydrogen intercalated epitaxial graphene where the interface layer is decoupled from the substrate and becomes a quasi-free standing graphene layer.
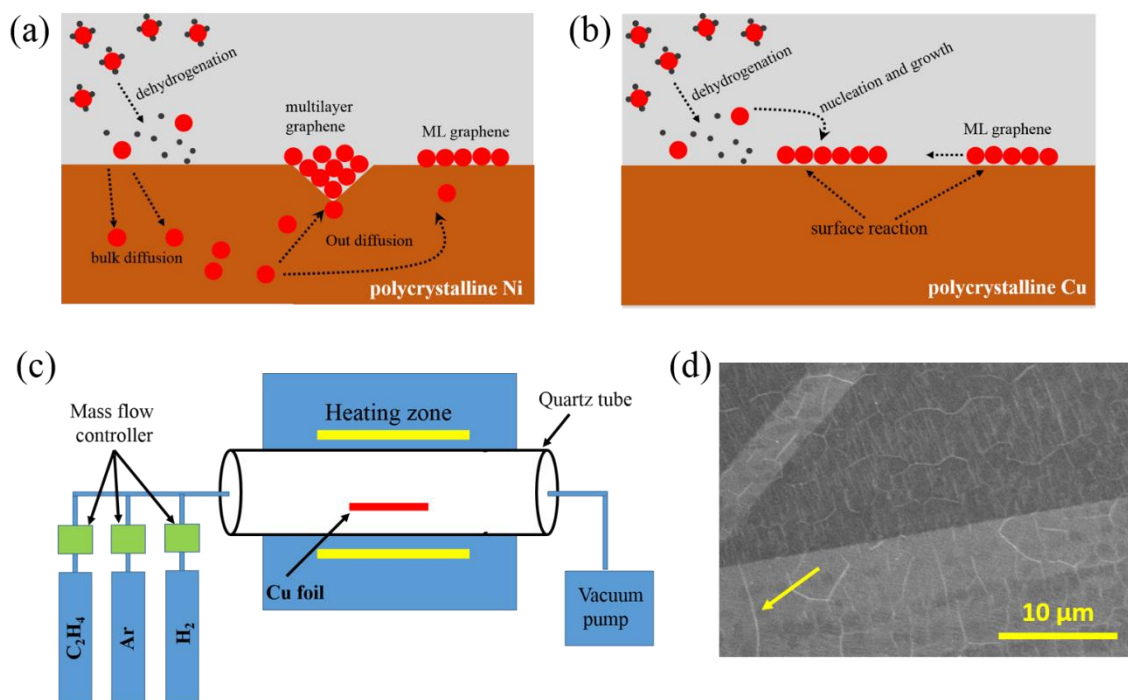
Figure 3.3: Illustration of the graphene growth mechanism on (a) Ni substrate, where bulk diffusion and faster precipitation at the grain boundaries result in multilayer graphene growth and (b) Cu substrate, where monolayer graphene forms due to a surface adsorption process. (c) Schematic of the complete CVD growth system. (d) SEM image of monolayer CVD graphene grown on Cu foil. Arrow points out the bulged up region of graphene called "graphene ridge" (Image adapted form Graphene Supermarket Inc. website).
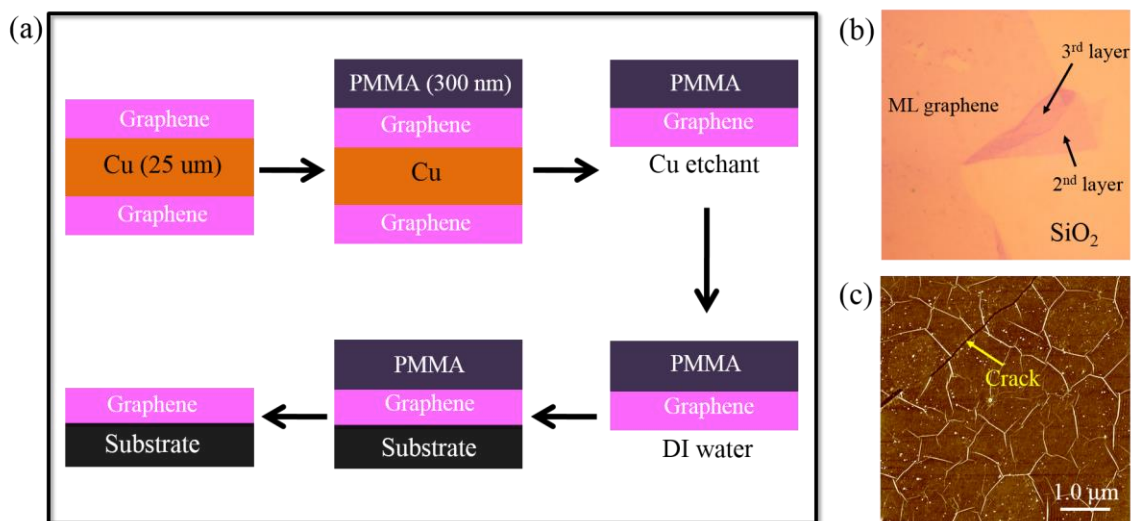
Figure 3.4: (a) Schematic of the polymer assisted graphene transfer process to transfer CVD graphene from Cu foil to an arbitrary substrate. (b) Optical microscope image of CVD graphene transferred onto a 285nm SiO_2 substrate. Number of graphene layers can be identified by different optical contrast on top of the SiO_2 substrate. (c) AFM image of uniform monolayer graphene transferred onto a SiO_2 substrate. Arrow points out a contrast between graphene and the underneath substrate due to a crack in the graphene film.

Chapter 4
Characterization Techniques

This chapter focuses on basic working principles of the main characterization techniques used in this dissertation. Section 4.1 covers Bardeen and Tersoff models for the calculation of tunneling current, and the implementation of scanning tunneling microscopy /spectroscopy (STM/STS). Section 4.2 presents Raman spectroscopy and its application to graphene.

4.1 Scanning tunneling microscopy/spectroscopy

Since the invention of STM by Binnig and Rohrer in 1982 [1], it has proven to be a powerful and unique tool to study the structural and electronic properties of conducting surfaces. An UHV STM provides unprecedented sub- Å spatial resolution that facilitates the visualization and manipulation of individual atoms. The first success of STM was the real space imaging of the 7×7 reconstruction of a Si(111) surface [2], which earned the inventors the 1986 Noble prize in physics. Since then, STM has contributed tremendously in determining atomic reconstructions on numerous surfaces and has become an integral part of research in the areas ranging from nanotechnology to chemistry to biology.

The operational principle of an STM is based on quantum mechanical tunneling. When a sharp metal tip is brought within ~1nm of the sample surface, applying a bias voltage between the tip and the sample allows tunneling of electrons through the gap between them. A schematic of an STM is shown in Fig. 4.1. The probe tip is attached to piezoelectric actuators that control the position of the tip in three dimensions. During

imaging, the STM tip raster scans in the xy plane on the surface, and a feedback loop simultaneously controls the z piezo actuator which adjusts the tip height ensuring a constant tunneling current. Surface morphology is acquired by monitoring the tunneling current as a function of tip position across the sample. Typically the tip height is in the range of 5 -10 Å above the surface, and the tunneling current is in the nano-Ampere range.

4.1.1 The working principle

In an elementary model, STM setup can be simplified to a one-dimensional metal-vacuum-metal tunneling junction where vacuum is modeled by a potential barrier U. If an applied bias voltage V_b is much smaller than the work function of the metal ϕ, the tunneling current in the junction is described by [3]

$$I(z) = I(0)e^{-2\Bbbk z} \tag{4.1}$$

where $\Bbbk = \sqrt{2m\phi}/\hbar$ is the decay constant. For typical values of work functions ($\phi \approx 5eV$) of materials used in STM, the decay constant $\Bbbk \approx 10 \text{ nm}^{-1}$. Thus, the tunneling current decays by an order of magnitude with the variation of 0.1 nm in the z axis. This sensitivity on the tip-sample distance is the reason for extremely high vertical resolution (~ 0.0001Å) of an STM.

Since this model is too simple to describe realistic STM experiments, the Bardeen and Tersoff-Hamann model of tunneling is presented in this section. As the majority of the results presented in this dissertation are obtained by STM and scanning tunneling spectroscopy (STS), the working principle of this technique is discussed in detail below.

4.1.1.1 Bardeen theory of tunneling

Bardeen's first order perturbation theory is the most widely used theory to explain tunneling phenomenon in a planar tunneling junction [4]. To model STM, tip and sample are represented by two electrodes separated by a vacuum barrier, and a tunneling current is given by a net rate of electrons transfer between the tip and the sample multiplied by the electron charge. The basic assumption of Bardeen's tunneling theory is that the electron-electron interaction can be ignored, and electrons in the sample and the tip are independently governed by single particle Hamiltonians, which can be described by

$$H_{sam}\Psi = \left[-\frac{\hbar^2}{2m}\frac{\partial^2}{\partial z^2} + U_{sam}(\vec{r})\right]\Psi(\vec{r}), \qquad \vec{r} \in R_S \tag{4.2}$$

$$H_{tip}\Psi = \left[-\frac{\hbar^2}{2m}\frac{\partial^2}{\partial z^2} + U_{tip}(\vec{r})\right]\Psi(\vec{r}), \qquad \vec{r} \in R_T \tag{4.3}$$

in terms of sample and tip potentials. Here, assume a nonzero sample potential $U_{sam}(\vec{r})$ inside the sample and barrier regions R_S, but zero in the tip region. Similarly set a nonzero tip potential $U_{tip}(\vec{r})$ inside the tip and barrier regions R_T, but zero in the sample region [Fig. 4.2 (a)]. The boundaries between the barrier region and the sample and tip regions are arbitrary. The eigenfunctions of the sample and tip Hamiltonians are called sample and tip states respectively. When the sample and tip are far apart, their wave functions decay into the vacuum and the stationary states are given by

$$\Psi_S = \psi_S e^{-iE_St/\hbar} \quad and \quad \Psi_T = \psi_T e^{-iE_Tt/\hbar} \tag{4.4}$$

with wavefunctions ψ and energy eigenvalues E satisfying

$$H_{sam}\psi_S = E_S\psi_S \quad and \quad H_{tip}\psi_T = E_T\psi_T \tag{4.5}$$

When the tip is close to the sample, the time dependent Schrödinger equation of the combined system is

$$i\hbar \frac{\partial \Psi}{\partial t} = \left[-\frac{\hbar^2}{2m}\frac{\partial^2}{\partial z^2} + U_{sam} + U_{tip} \right]\Psi \tag{4.6}$$

In the presence of the combined potentials, neither ψ_S nor ψ_T is an eigenfunction of the Hamiltonian. Instead, an electron initially in the sample state has a probability of transferring to the tip states and vice versa. Therefore for weak interaction, we assume the evolution of the wave function as

$$\Psi(t) = \psi_S\, e^{-iE_S t/\hbar} + \sum_{T=1}^{\infty} c_T(t)\, \psi_T\, e^{-iE_T t/\hbar} \tag{4.7}$$

where $c_T(0) = 0$. Plugging Eq. (4.7) into Eq. (4.6), and only taking up to first order perturbations, we have

$$i\hbar \sum_{T=1}^{\infty} \frac{dc_T(t)}{dt}\psi_T\, e^{-iE_T t/\hbar} = U_{tip}\psi_S\, e^{-iE_S t/\hbar} \tag{4.8}$$

After multiplying $< \psi_T |$ on both sides

$$i\hbar\, \frac{dc_T(t)}{dt} = \int \psi_S\, U_{tip}\psi_T^*\, d^3\vec{r}\; e^{-i(E_S - E_T)t/\hbar} \tag{4.9}$$

A tunneling matrix element, interaction energy due to the overlap of two unperturbed states, is defined as

$$M_{ST} = \int \psi_S\, U_{tip}\psi_T^*\, d^3\vec{r} \tag{4.10}$$

After integration of Eq. (4.9) over time, the amplitude of the tip state at time t is

$$c_T(t) = M_{ST}\, \frac{\left[e^{-i(E_S - E_T)t/\hbar} - 1 \right]}{E_S - E_T} \tag{4.11}$$

and the transition probability for an electron initially in a sample state that scatters into a Tth tip state at time t is

$$| < \psi_T | \Psi(t) > |^2 = | < \psi_T | \psi_S > e^{-iE_St/\hbar} + c_T(t)|^2 \tag{4.12}$$

Under the assumption of approximately orthogonal sample and tip states, the first term becomes small and the main contribution comes from $|c_T(t)|^2$. The total rate at which an electron initially in a sample state scatters into the tip states is expressed as

$$P_{ST}(t) = \frac{d}{dt} \sum_T |c_T(t)|^2 = \frac{d}{dt} \sum_T |M_{ST}|^2 \frac{4 \sin^2[(E_S - E_T)t/2\hbar]}{(E_S - E_T)^2} \tag{4.13}$$

which approaches zero rapidly for $E_T \neq E_S$. Considering the nearly elastic tunneling condition, $E_T \approx E_S$, the tip energy levels distribute with constant density over the narrow energy interval $-2h/t < (E_T - E_S) < 2h/t$. The summation over the discrete tip states can be replaced by an integral over energies using $\sum_T \rightarrow \int \rho(\varepsilon)d\varepsilon$. Let $\rho_{tip}(\varepsilon)$ represents the DOS of the tip at energy ϵ, then Eq. (4.13) can be approximated as

$$P_{ST}(t) = \frac{d}{dt}\left[4 |M_{ST}|^2 \rho_{tip}(\varepsilon) \int_{-2h/t}^{2h/t} \frac{4 \sin^2[\varepsilon t/2\hbar]}{(\varepsilon)^2} d\varepsilon\right]$$

$$= \frac{d}{dt}\left[4 |M_{ST}|^2 \rho_{tip}(\varepsilon) \frac{\pi t}{2\hbar}\right]$$

$$= \frac{2\pi}{\hbar} |M_{ST}|^2 \rho_{tip}(\epsilon) \tag{4.14}$$

Equation (4.14) gives the tunneling rate at which electrons transfer from a particular sample state $\psi_{S,n}$ to tip states of comparable energy, provided all those tip states are unoccupied. However, according to Pauli's Exclusion Principle only one electron can occupy a given tip state, so the tip DOS in Eq. (4.14) needs to be multiplied by the probability of unoccupied tip states at energy ϵ. Then

$$P_{ST} = \left(1 - f_{tip}(\varepsilon)\right)\frac{2\pi}{\hbar} |M_{ST}|^2 \rho_{tip}(\epsilon) \tag{4.15}$$

Where $f(\varepsilon)$ is the Fermi-Dirac distribution function,

$$f(\varepsilon) = \frac{1}{\left[1 + \exp\left(\frac{(\varepsilon - E_f)}{K_B T}\right)\right]} \tag{4.16}$$

and the probability of occupied and unoccupied states are described by $f(\varepsilon)$ and $[1 - f(\varepsilon)]$, respectively. Similarly, the tunneling rate due to scattering from all tip states into a particular sample state $\psi_{S,n}$ is given by

$$P_{TS} = f_{tip}(\varepsilon) \frac{2\pi}{\hbar} |M_{ST}|^2 \rho_{tip}(\epsilon) \tag{4.17}$$

Naturally an electron can only tunnel from an occupied state to an unoccupied state. Occupied sample states contribute to a current of electrons scattered from the sample to the tip at a rate given by Eq. (4.15), and unoccupied sample states enable electrons to flow from the tip to the sample at a rate given by Eq. (4.17). Therefore, the total tunneling current from the sample to tip and the tip to sample can be written as the electron charge times P_{TS} summed over all of the sample states $\psi_{S,n}$.

$$I_{S \to T} = \frac{4\pi e}{\hbar} \sum_n f_{Sam}(\varepsilon) * \left(1 - f_{tip}(\varepsilon)\right) |M_{ST}|^2 \rho_{tip}(\epsilon) \tag{4.18}$$

$$I_{T \to S} = \frac{4\pi e}{\hbar} \sum_n \left(1 - f_{sam}(\varepsilon)\right) * f_{tip}(\varepsilon) |M_{ST}|^2 \rho_{tip}(\epsilon) \tag{4.19}$$

The difference between the two currents gives a net tunneling current in the junction

$$I = \frac{4\pi e}{\hbar} \sum_n \left[f_{Sam}(\varepsilon) - f_{tip}(\varepsilon)\right] |M_{ST}|^2 \rho_{tip}(\epsilon)$$

$$= \frac{4\pi e}{\hbar} \int_{-\infty}^{\infty} \left[f_{Sam}(\varepsilon) - f_{tip}(\varepsilon)\right] |M_{ST}|^2 \rho_{tip}(\epsilon) \, \rho_{sam}(\epsilon) \, d\epsilon \tag{4.20}$$

Now, when a bias voltage V_b is applied between the sample and the tip, their Fermi levels are no longer aligned, and electrons can tunnel across the barrier from occupied

states into unoccupied states ranging from E_F to $(E_F - e\,V_b)$. For positive sample bias, electrons tunnel from occupied states of the tip to empty states of the sample. Whereas, for negative sample bias electrons tunnel from occupied states of the sample to empty states of the tip [Fig. 4.2 (b)]. The net tunneling current for a bias voltage V_b can be written as

$$I = \frac{4\pi e}{\hbar} \int_{-\infty}^{\infty} [f(E_F - e\,V_b + \varepsilon) - f(E_F + \varepsilon)] |M_{ST}|^2$$

$$\times \; \rho_{tip}(E_F - e\,V_b + \varepsilon)\, \rho_{sam}(E_F + \varepsilon)\, d\epsilon \tag{4.21}$$

For low temperatures, when $K_B T$ is smaller than the energy resolution required in measurement, the Fermi distribution function can be approximated by a step function and the tunneling current becomes

$$I = \frac{4\pi e}{\hbar} \int_{0}^{eV_b} \rho_{tip}(E_F - e\,V_b + \varepsilon)\, \rho_{sam}(E_F + \varepsilon)\, |M_{ST}|^2\, d\epsilon \tag{4.22}$$

Tunneling Matrix element: To apply Bardeen's tunneling theory, evaluation of the tunneling matrix elements is critical. We begin by plugging U_{tip} from Eq. (4.2) and Eq. (4.5) into Eq. (4.10), we can write

$$M_{ST} = \int \; \psi_S \left(E_T + \frac{\hbar^2}{2m} \frac{\partial^2}{\partial z^2} \right) \psi_T^* \, d^3\vec{r} \tag{4.23}$$

Again assuming an elastic tunneling condition again $E_T = E_S$, we have

$$M_{ST} = \int \; \left(\psi_T^* E_S \psi_S + \psi_S \frac{\hbar^2}{2m} \frac{\partial^2 \psi_T^*}{\partial z^2} \right) d^3\vec{r} \tag{4.24}$$

Using Eq. (4.5) to replace $E_S\,\psi_S$, and recalling that sample potential U_{sam} is zero on the tip side, Eq. (4.24) can be written as

$$M_{ST} = -\frac{\hbar^2}{2m} \int \left(\psi_T^* \frac{\partial^2 \psi_S}{\partial z^2} - \psi_S \frac{\partial^2 \psi_T^*}{\partial z^2} \right) d^3\vec{r} \tag{4.25}$$

After rewriting the bracket term as $\frac{\partial}{\partial z}\left[\psi_T^* \frac{\partial \psi_S}{\partial z} - \psi_S \frac{\partial \psi_T^*}{\partial z} \right]$ and taking integration over z,

Bardeen's tunneling matrix element becomes a two dimensional integral

$$M_{ST} = -\frac{\hbar^2}{2m} \int \left(\psi_T^* \frac{\partial \psi_S}{\partial z} - \psi_S \frac{\partial \psi_T^*}{\partial z} \right) dxdy \tag{4.26}$$

This is a surface integral of wave functions, evaluated at the 2D plane in between the two

free electrodes. Note that for elastic tunneling, the plane of integration could be anywhere

in between the two electrodes. Thus far we have assumed a simple planar tunneling

geometry. Using similar formalism for the general 3D case of tunneling between two non-

planar surfaces, the tunneling matrix element can be written as

$$M_{ST} = -\frac{\hbar^2}{2m} \int_{\Sigma} (\psi_T^* \nabla \psi_S - \psi_S \nabla \psi_T^*) . d\vec{S} \tag{4.27}$$

where integration take place on any separation surface Σ between the tip and the sample.

4.1.1.2 The Tersoff-Hamann model

According to Bardeen's theory, the tunneling current in STM is a function of the

convolution of the tip and sample electronic states as shown in Eq. (4.22). Unfortunately,

it is difficult to know the tip states experimentally. Tersoff and Hamann proposed a model

just one year after the invention of STM, which assumed the STM tip as a geometrical

point with negligible interaction between the tip and the sample [5, 6]. As shown in Fig.

4.2(c), the STM tip is modeled as a locally spherical potential well with radius of curvature

R centered at r_0. The tip wavefunction can be taken as spherically symmetric s-wave,

$$\psi_T(\vec{r}) = \sqrt{\frac{1}{4\pi} \frac{C}{k}} \frac{e^{-k|r-r_0|}}{|\vec{r} - \vec{r}_0|}$$

or in terms of Green's function

$$\psi_T(\mathbf{r}) = \frac{\sqrt{4\pi} \, C}{k} \, G(\vec{r} - \vec{r}_0) \tag{4.28}$$

If we plug Eq. (4.28) into Eq. (4.27) and use the divergence theorem to convert the surface

integral into a volume integral, the tunneling matrix element for an s-wave tip state is

$$M_{TS} = \frac{2\pi C \hbar^2}{km} \int_{\Omega_T} [\psi_S \nabla^2 G(\vec{r} - \vec{r}_0) - G(\vec{r} - \vec{r}_0) \nabla^2 \psi_S] \, d\vec{\tau} \tag{4.29}$$

Notice that the sample wave function satisfies the Schrodinger equation in vacuum, such

that $\nabla^2 \psi_S = k^2 \psi_S$, and Green's function satisfies $[\nabla^2 - k^2]G(\vec{r} - \vec{r}_0) = -\delta(\vec{r} - \vec{r}_0)$.

This simplifies Eq. (4.29) as

$$M_{TS} = \frac{2\pi C \hbar^2}{km} \int_{\Omega_T} \psi_S \, \delta(\vec{r} - \vec{r}_0) \, d\vec{\tau} = \frac{2\pi C \hbar^2}{km} \psi_S(\vec{r}_0) \tag{4.30}$$

This is the main result of the Tersoff-Hamann model, which demonstrates that the

tunneling matrix element is proportional to the sample wave function evaluated at the tip

apex for a spherically symmetric tip. This model neglects all the other tip wavefunctions

except s-wave, hence often referred to as the s-wave tip model. It is important to know that

the Tersoff-Hamann model is valid only for feature sizes larger than the typical length scale

of the electron states of the STM tip. For feature sizes $\leq 0.3 \, nm$, the p-wave or d-wave tip

state can dominate the tunneling matrix element and STM images can be very different

from the prediction of this model. According to Chen's derivative rule, if tunneling occurs

from a p- or d-wave tip state, the tunneling matrix element is proportional to the first or

second z-derivative of the sample wave function evaluated at the tip apex, respectively [3].

4.1.2 Two modes of operation: imaging and spectroscopy

4.1.2.1 Imaging mode and resolution

The STM can be operated either in constant current mode or constant height mode during imaging. In constant current mode, which is the most commonly used mode, the feedback electronics adjust the tip height during scanning so that the tunneling current between the tip and the sample is kept constant [Fig. 4.1(b)]. The tip height adjustment is performed by applying a correcting voltage to the z-piezo actuator. The changes in the tip height at each sample pixel can be used to generate a topographic image of the sample surface. Tunneling current has strong exponential dependence on the distance between the tip and the surface, and thus the feedback circuit is very sensitive to detecting minute changes in tip height [3]. Alternatively, in constant height mode, the STM tip scans at a constant height over the surface and modulation in the tunneling current is measured [Fig. 4.1(c)]. Constant height mode is faster compared to the constant current mode, however, it is only useful for flat surfaces and for small scan areas.

In the beginning of their experimentation, Binnig and Rohrer estimated the lateral resolution of STM using a simple spherical tip model, where the radius of curvature of the tip end is made of several atoms. They argued that if the distance between the tip and the sample surface is much smaller than the radius of the tip end R, it is possible to achieve a lateral resolution much smaller than the tip radius [7]. Near the tip end, the tunneling current lines are almost perpendicular to the sample surface, and are concentrated in a small region around the origin $x = 0$. At a point Δx on the tip, the distance to the sample surface is increased by $\Delta z \approx (\Delta x^2 / 2R)$. From Eq. (4.1), the lateral current distribution is

$$I(\Delta x) = I_0 exp\left(-2\mathfrak{k}\frac{\Delta x^2}{2R}\right) \tag{4.31}$$

For $R \approx 1nm$, the tunneling current decays by an order of magnitude at $\Delta x \approx 0.3nm$. Thus, the resolution limit of STM is determined by the diameter of such a current column $2\Delta x \approx 0.6nm$. However, this expectation is greatly exceeded by current STM technology where a lateral spatial resolution of $0.1nm$ is routinely observed.

According to Tersoff-Homann, the effective lateral resolution is related to the tip radius R and the tunneling gap d [6]

$$L_{eff} = \sqrt{\frac{R + d}{2\mathfrak{k}}} \tag{4.32}$$

If R $\gg$ d, the resolution is determined by the tip radius but it is nonetheless much smaller than R. For R $\ll$ d, as in case of single atom tip, the resolution is limited by the tunneling gap.

4.1.2.2 Spectroscopy mode

One of the most fascinating aspects of STM is its capability to perform local tunneling spectroscopy with atomic resolution, which distinguishes it from other surface spectroscopic techniques. Actually, the original idea of building a STM was to perform tunneling spectroscopy locally on an area of less than 10 nm in diameter [8]. In spectroscopy mode, the STM tip is held at a constant height above the surface by turning off the feedback loop, and the tunneling current is measured as a function of the bias voltage by applying a voltage ramp between the tip and the sample. The resulting $(I - V)$ curve provides information about the energy dependent DOS of both the tip and the sample. Recalling Bardeen's expression of tunneling current for a bias voltage V_b, from Eq. (4.22)

$$I = \frac{4\pi e}{\hbar} \int_0^{eV_b} \rho_{tip}(E_F - e\,V_b + \varepsilon)\,\rho_{sam}(E_F + \varepsilon)\,|M_{ST}|^2\,d\epsilon$$

For a small energy range, the tunneling matrix element does not depend on the energy level and can be taken out of integral [3]. If we further assume that the tip has a flat DOS over the energy interval of interest, $\rho_{tip}(E_F - e\,V_b + \varepsilon) = \rho_{tip}$ for all ε, the tunneling current becomes

$$I \approx \frac{4\pi e}{\hbar}\,\rho_{tip}\,|M|^2 \int_0^{eV_b} \rho_{sam}(E_F + \varepsilon)\,d\epsilon \tag{4.33}$$

Applying the Tersoff-Hamann model for finite bias voltages using Eq. (4.30), the tunneling current is proportional to

$$I \propto \rho_{tip}\,|\psi_S(\vec{r}_0)|^2 \int_0^{eV_b} \rho_{sam}(E_F + \varepsilon)\,d\epsilon \tag{4.34}$$

Remembering the definition of the local DOS of the sample at an energy level E at the center of curvature of the tip $\rho_{sam}(E, \vec{r}_0) = |\psi_S(\vec{r}_0)|^2\,\rho_{sam}(E)$, then

$$I \propto \int_0^{eV_b} \rho_{sam}(E_F + \varepsilon, \vec{r}_0)\,d\epsilon \tag{4.35}$$

Differentiating Eq. (4.35) with respect to V_b,

$$G(V_b) = \left(\frac{dI}{dV}\right)_{V=V_b} \propto \rho_{sam}(E_F + eV_b, \vec{r}_0) \tag{4.36}$$

This shows that the differential tunneling conductance (dI/dV) at low temperatures and low bias voltage is proportional to DOS of the sample at an energy level $(E_F + eV_b)$ at center of the curvature of tip. Hence the local DOS of the sample can be probed by measuring the tunneling current as a function of applied bias voltage. Note that this requires the STM tip to have flat DOS, which is typically achieved by pulsing or crashing the tip

into a metal surface. The methods for tip calibration will be discussed in detail in the instrumentation section (Appendix A).

Although the (dI/dV) can be numerically calculated by the slope of $(I - V)$ curve at each voltage, but this method produces extremely noisy data. To obtain a high signal to noise ratio, (dI/dV) is directly measured using lock-in technique. In this method, the bias voltage V_b is modulated with a small sinusoidal voltage $V_R \sin(\omega t)$. For $V_R \ll V_b$, the tunneling current can be expanded in the Taylor series

$$I(V_b + V_R \sin(\omega t)) = I(V_b) + \left.\frac{dI}{dV}\right|_{V_b} \cdot V_R \sin(\omega t)$$

$$+ \frac{1}{4}\left.\frac{d^2I}{dV^2}\right|_{V_b} V_R^2(1 - \cos(2\omega t)) + \cdots \qquad (4.37)$$

In the first approximation, the amplitude of the current modulation is proportional to (dI/dV) at that bias voltage, which is measured by the lock-in amplifier. Details of the lock-in technique will be discussed in the appendix section.

Thermal fluctuations reduce the resolution of both topography and spectroscopy. It is therefore beneficial to carry out STM experiments at low temperatures. In this dissertation, we used an Omicron VT-STM at room temperature and an LT-STM at 77 K under UHV with a base pressure of $\sim 1\times10^{-11}$ Torr. All the spectroscopy measurements were done at 77 K.

4.2   Raman Spectroscopy

Raman Spectroscopy has evolved as an important tool for nanoscience and nanotechnology. It has been extremely successful in advancing our knowledge about graphene and other 2D materials. It is a spectroscopic technique based on the Raman effect

which relies on inelastic scattering of light by matter [9]. When a sample is irradiated with an intense monochromatic light source (usually a laser), most of the photons scatter elastically with the same frequency as the incident radiation, known as Rayleigh scattering. A small proportion of the incident photons (0.01%) scatter inelastically, with frequency of the scattered photons being shifted up or down. Frequency difference between the incident and the scattered photons stems from the quantized excitation that is created or annihilated in the material. If the quantum excitation is a molecular vibration or an optical phonon, the inelastic light scattering process is known as the Raman effect [10]. It was discovered in 1928 by an Indian physicist Chandrasekhara Venkata Raman for which he was awarded the 1930 Nobel Prize in Physics [10, 11].

According to energy and momentum conservation, energy E_S and momentum k_S of the scattered photon in a Raman process

$$E_S = E_i \pm E_q \quad and \quad k_S = k_i \pm k_q \tag{4.38}$$

where E_i and k_i are energy and momentum of the incident photon. E_q and k_q are change in energy and momentum induced by the excitation in the medium. Although different excitations result from Raman scattering, the most usual scattering phenomenon involves phonons. The inelastic process when a photon loses energy in creating a phonon resulting in a scattered photon having lower energy, is known as Stokes Raman scattering [Fig. 4.3]. Another form of scattering occurs when the incident photon gains energy by annihilating a phonon resulting in a scattered photon with greater energy. This process is known as anti-Stokes Raman scattering. Both the processes can be described using a classical description.

4.2.1 The classical description of Raman effect

The Raman effect is based on molecular deformations in presence of electric field E determined by molecular polarizability α; a measure of how easy it is to polarize the molecule along each direction. Electric field of incident light can be considered as an oscillating electromagnetic wave with frequency ω_0

$$E = E_0 \cos(2\pi\omega_0 t) \tag{4.39}$$

where E_0 is the vibrational amplitude. When a molecule is irradiated by light, incident photons excite molecules and transform them into oscillating dipoles. Induced polarization by the applied field is

$$P = \alpha E = \alpha E_0 \cos(2\pi\omega_0 t) \tag{4.40}$$

The polarizability α can be looked on as the deformability of electron cloud of the molecule by the electric field. It does not have a constant value since certain lattice vibrations in solids can modulate the polarizability. For small displacement, the polarizability can be expanded in the Taylor series as

$$\alpha = \alpha_0 + \frac{\partial\alpha}{\partial Q}Q + \cdots \tag{4.41}$$

where α_0 is equilibrium polarizability, Q normal coordinate varying periodically such as

$$Q = Q_0 \cos(2\pi\omega_m t) \tag{4.42}$$

where ω_m is frequency of the normal co-ordinate vibration and Q_0 is constant. Combining all the above equations

$$P = \alpha_0 E_0 \cos(2\pi\omega_0 t) + \frac{\partial\alpha}{\partial Q}Q_0 E_0 \cos(2\pi\omega_0 t)\cos(2\pi\omega_m t)$$

$$P = \alpha_0 E_0 \cos(2\pi\omega_0 t) + \frac{\partial\alpha}{\partial Q}\frac{Q_0 E_0}{2}[\cos(2\pi(\omega_0 - \omega_m)t) + \cos(2\pi(\omega_0 + \omega_m)t)] \tag{4.43}$$

This demonstrates that oscillating dipoles emit light of three different frequencies ω_0, $(\omega_0 - \omega_m)$ and $(\omega_0 + \omega_m)$ that give rise to Rayleigh scattering, Stokes and anti-Stokes Raman scattering, respectively [Fig. 4.3].

1. With no Raman-active modes, excited molecules return back to a basic vibrational state and emit light elastically with the same frequency ω_0 as that of the excitation source. This type of interaction is called Rayleigh scattering.

2. When a photon with frequency ω_0 is absorbed by a Raman-active molecule, which is in the basic vibrational state at the time of interaction, part of the photon's energy transfers to the Raman-active mode and frequency of the scattered light downshifts by the natural vibration frequency of molecule to $(\omega_0 - \omega_m)$. This Raman frequency is called the Stokes frequency.

3. When a photon with frequency ω_0 is absorbed by a Raman-active molecule, which is in the excited vibrational state at the time of interaction, excessive energy of the excited Raman-active mode dissipates resulting in the molecule returning to a basic vibrational state. As a result, the frequency of the scattered light goes up to $(\omega_0 + \omega_m)$. This Raman frequency is called the anti-Stokes frequency.

For vibrations that cause no change in the polarizability i.e. $\partial\alpha/\partial Q = 0$, the Raman frequencies of the induced dipole moment have zero amplitude. Therefore in order for a molecular vibration to be Raman active, the vibration must be accompanied by a change in the polarizability of the molecule. According to the Boltzmann distribution function, the ratio of number of molecules in excited state to that of ground state for a given vibration is given by [9]

$$\frac{n_1}{n_0} = Exp\left[-\left(\frac{h\,\omega_m}{K\,T}\right)\right] \tag{4.44}$$

At room temperature most of the molecules exist in ground state and therefore the Stokes lines have greater intensities than the anti-Stokes lines which originate from an excited level with lower population.

4.2.2 Raman spectroscopy of graphene

Raman spectroscopy is a commonly used tool to differentiate between monolayer, bilayer and multilayer graphene. Among all the sp^2 carbon systems, the monolayer graphene has the simplest Raman spectra. Most prominent features in the Raman spectra of monolayer graphene are the G- and 2D-band appearing at ~ 1580 and ~ 2700 cm^{-1}, respectively, as shown in Fig. 4.4 (a) [12, 13]. A disorder induced D-band also appears at ~ 1350 cm^{-1} in presence of defects in graphene.

4.2.2.1 The G band

It is a first order Raman allowed feature originating from in plane stretching of the C-C bond in the sp^2 graphitic materials [13]. It is associated with doubly degenerate phonon modes (E$_{2g}$ symmetry) at the BZ center. The in-plane transverse optic (iTO) phonon and the longitudinal optical (LO) phonon modes are degenerate at the Γ point, and corresponds to the vibrations of sublattice A against sublattice B. In the presence of strain, the iTO and the LO phonon frequencies split and causes the G band to split into two peaks named as G^+ and G^-. These bands are related to longitudinal (G^-) and transverse (G^+) atomic motions with respect to strain direction [14]. The splitting between the peaks increases as the strain increases, as observed in carbon nanotubes. The G band is also quite sensitive to charge

doping in the graphene, and is observed to upshift in frequency and decrease in linewidth for electron as well as for hole doping [15].

In a Raman process, the incident photons interacts with the lattice vibrations via electrons. For a normal first order Raman scattering process, an incident photon excites an electron from the valence band to the conduction band. The excited electron then emits a phonon of wave vector q ≈ 0 through an electron-phonon interaction, and then the electron recombines with the hole and emits a photon of lower energy [Fig. 4.4 (b)]. The first and the last step in this process are optical transitions due to electron-photon interactions, which have an angular dependence on the incident light polarization. This causes a change in the G band intensity as a function of the polarization angle of the incident light [12].

4.2.2.2 The 2D band

It originates from a double resonance second order Raman process, involving two iTO phonon modes in the vicinity of the K point. A resonant Raman process takes place when the incident or the scattered photon energy matches the energy gap between an occupied initial state and an unoccupied final state. Probability of the Raman scattering increases by many orders of magnitude in the resonant Raman process. If a photon can connect the two conduction electronic states in the graphene, the scattering process will be resonant. A double resonance process involves electron-photon and electron-phonon resonant scattering events [16].

Raman process for the 2D band begins with excitation of an electron-hole pair by absorbing an incident photon at the K point [Fig. 4.4 (c)]. The excited electron with wave vector k then scatters inelastically to the other valley by emitting a phonon of wave vector q. At the end of this process the electron is at the K' point with a wave vector (k-q). Next,

the electron scatters back to the k state by a phonon of wave vector -q and recombines with hole at the k state by emitting a photon of lower energy. The resonance condition selects a phonon of specific momentum. The wave vectors q of the phonons associated with the 2D band preferentially couple to electronic states with a wave vector k, such that q ≈ 2k [12]. This process is called inter-valley two phonon scattering process because it connects two conduction band states of inequivalent K and K' points in the first BZ of graphene.

The 2D band is commonly used to determine the number of graphene layers and stacking order between them in samples [17, 18]. The Raman fingerprint of the monolayer graphene is a symmetric intense 2D peak with full width at half maximum (FWHM) ~ 30 cm^{-1}, which can be fit with a Lorentzian function. Large intensity of the 2D band relative to the first order G band is also a signature of the monolayer graphene. Since bilayer graphene has a parabolic dispersion relation near the K point with two conduction and two valence bands, the 2D peak of bilayer graphene is the superposition of four resonant contributions in the scattering process and can be fit by four Lorentzian functions [17]. The situation gets more complex as the number of graphene layers increases because then possible number of scattering processes increases. Trilayer graphene has 15 scattering possibilities and as a result 2D band becomes broader and strongly asymmetric [19].

4.2.2.3 The D band

This band is a probe for the amount of disorder in graphene and appears at roughly half of the position of the 2D band. It also originates from inter-valley second order double resonance process similar to the 2D band, but involving one iTO phonon near the K point and one defect [Fig. 4.4(d)]. Out of the two inelastic phonon scattering processes in the 2D band, one is replaced by an elastic scattering by a lattice defect in the case of the D band

[13]. For pristine graphene, there is only one single phonon scattering process for which momentum conservation requires q = 0. However for disordered graphene, the Raman modes corresponding to single phonon scattering with wave vector q≠ 0 are allowed and the momentum conservation requirement can be satisfied through an elastic process by a defect.

Both the 2D and the D bands exhibit dispersive behavior as their frequencies change as a function of energy of the incident laser light, which is a direct consequence of the double resonance Raman process. Since graphene has a zero energy gap at the K point, there is always a resonant absorption for a broad range of the excitation energies. When the energy of the incident light is changed, the excited electron wave vector is different and hence the wave vector and the energy of phonon that will satisfy double resonance condition is also different. Frequencies of the 2D and the D bands upshift linearly with the laser energy at a rate of ~100 cm^{-1}/eV and 50 cm^{-1}/eV respectively [20]. In this work, we used a Renishaw Raman spectrometer with 633 nm wavelength HeNe laser.

References

1. G. Binning and H. Rohrer. Scanning tunneling microscopy. *Surf. Sci.* **126,** 236 (1983).

2. G. Binning, H. Rohrer, Ch. Gerber and E. Weibel. 7 x 7 reconstruction on Si(111) resolved in real space. *Phys. Rev. Lett.* **50,** 120 (1983).

3. C. J. Chen. Introduction to Scanning Tunneling Microscopy. Oxford University Press, 2nd edition, New York (2008).

4. J. Bardeen. Tunneling from a many particle point of view. *Phys. Rev. Lett.* **6**, 57 (1961).

5. J. Tersoff and D. R. Hamann. Theory and application for the scanning tunneling microscope. *Phys. Rev. Lett.* **50**, 1998 (1983).

6. J. Tersoff and D. R. Hamann. Theory of scanning tunneling microscope. *Phys. Rev. B* **31**, 805 (1985).

7. C. F. Quate. Vacuum tunneling: A new technique for microscopy. Physics Today, page 26, August (1986).

8. G. Binning and H. Rohrer. Scanning tunneling microscopy- from birth to adolescence. *Rev. Mod. Phys.* **59,** 615 (1987).

9. N. B. Colthup, L. H. Daly and S. E. Wiberley. Introduction to infrared and Raman Spectroscopy (Academic press Inc., 1990).

10. C. V. Raman. A new radiation. *Indian J. Phys.* **2,** 387 (1928).

11. R. Singh. C. V. Raman and the discovery of the Raman effect. *Phys. Perspect.* **4,** 399 (2002).

12. L. M. Malard, M. A. Pimenta, G. Dresselhaus and M. S. Dresselhaus. Raman spectroscopy in graphene. *Phys. Reports* **473,** 51 (2009).

13. A. Jario, R. Satio, G. Dresselhaus and M. S. Dresselhaus. Raman Spectroscopy in Graphene Related Systems. WILEY-VCH Verlag GmbH & Co. KGaA (2011).

14. M. Huang, H. Yan, C. Chen, D. Song, T. F. Heinz and J. hone. Phonon softening and crystallographic orientation of strained graphene studied by Raman spectroscopy. *Proc. Natl. Acad. Sci.* **106,** 7304 (2009).

15. A. Das *et al.* Monitoring dopants by Raman scattering in an electrochemically top gated graphene transistor. *Nat. Nanotech.* **3,** 210 (2008).

16. C. Thomsen and S. Reich. Double resonant Raman scattering in graphite. *Phys. Rev. Lett.* **85,** 5214 (2000).

17. A. C. Ferrari *et al.* Raman spectrum of graphene and graphene layers. *Phys. Rev. Lett.* **97,** 187401 (2006).

18. J. S. Park, A. Raina, R. Saito, J. Kong, G. Dresselhaus and M. S. Dresselhaus. G' band Raman spectra of single, double and triple layer graphene. *Carbon* **47,** 1303 (2009).

19. L. M. Malard, M. H. D. Guimaraes, D. L. Mafra, M. S. C. Mazzoni and A. Jario. Group theory analysis of electrons and phonons in N-layer graphene system. *Phys. Rev. B* **79,** 125426 (2009).

20. M. J. Mathews, M. A. Pimenta, G. Dresselhaus, M. S. Dresselhaus and M. Endo. Origin of the dispersive effects of the Raman D band in carbon material. *Phys. Rev. B* **59,** 6585 (1999).
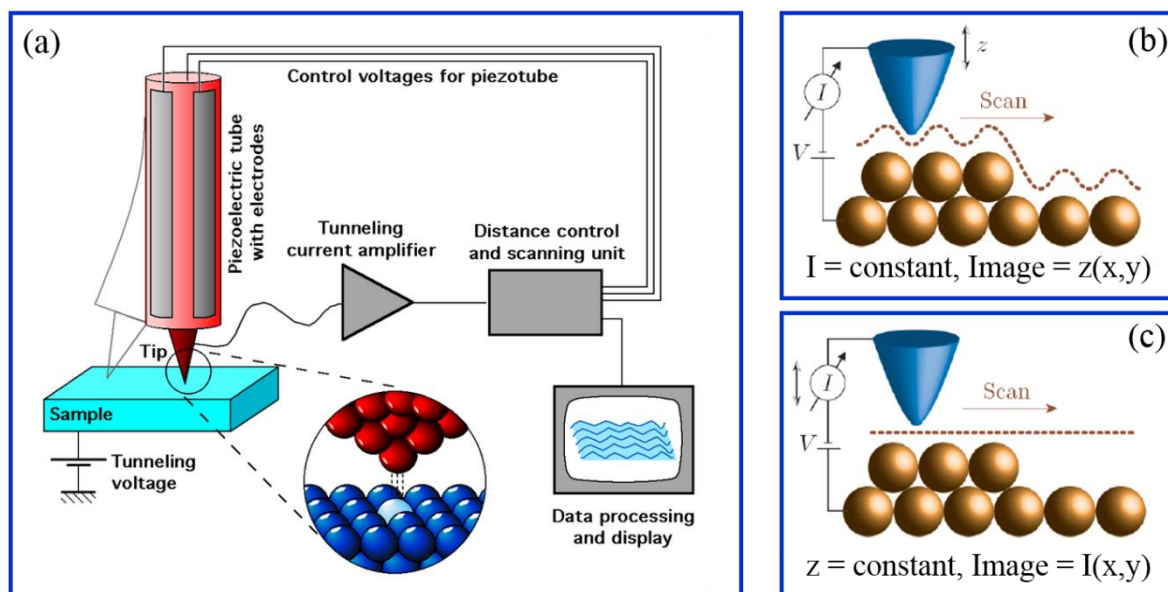
Figure 4.1: (a) Schematic of the basic components of an STM. The STM tip is brought close to sample with a piezoelectric scanner until the tunneling current is detected. The tunneling current is amplified and sent to the feedback electronics, which control the tip sample distance via a feedback loop. Inset shows the magnified view of the tip and sample where the tip is made up of a single atom at its apex. Schematic view of (b) constant current and (c) constant height scanning mode, where the sample surface topographic information is extracted by change in the tip height and the tunneling current, respectively. Image source www.wikipedia.org.
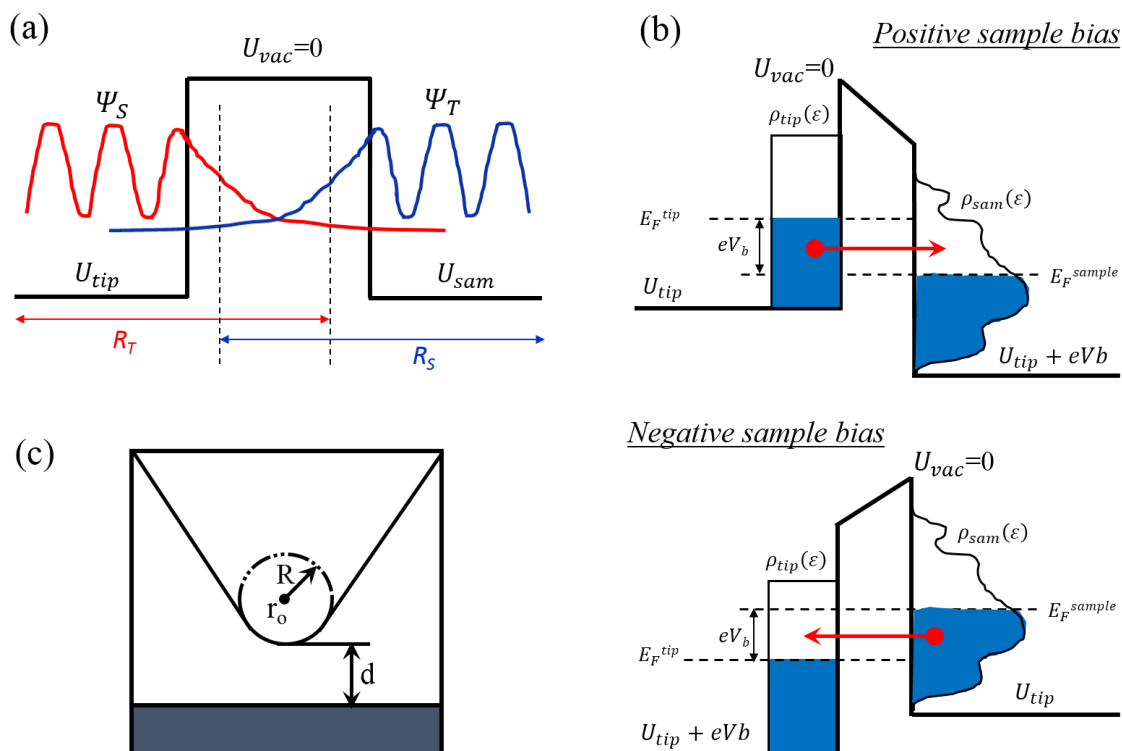
Figure 4.2: (a) Schematic of Bardeen's planer tunneling junction where the STM tip and sample are represented by two electrodes. When the two electrodes are far apart, their wave functions decay into vacuum, while tunneling can take place if the electrodes brought closer. (b) Schematic of the tunnel junction with a finite bias voltage applied between the tip and sample. A net tunneling current (represented by red arrow) flows from the occupied tip states to the unoccupied sample states for a positive sample bias, and from the occupied sample states to the unoccupied tip states for a negative sample bias. (c) The Tersoff – Hamann model of STM where the tip is modeled as a spherically symmetric potential well with radius of curvature R centered at r_0. (Adapted from ref. [5]).
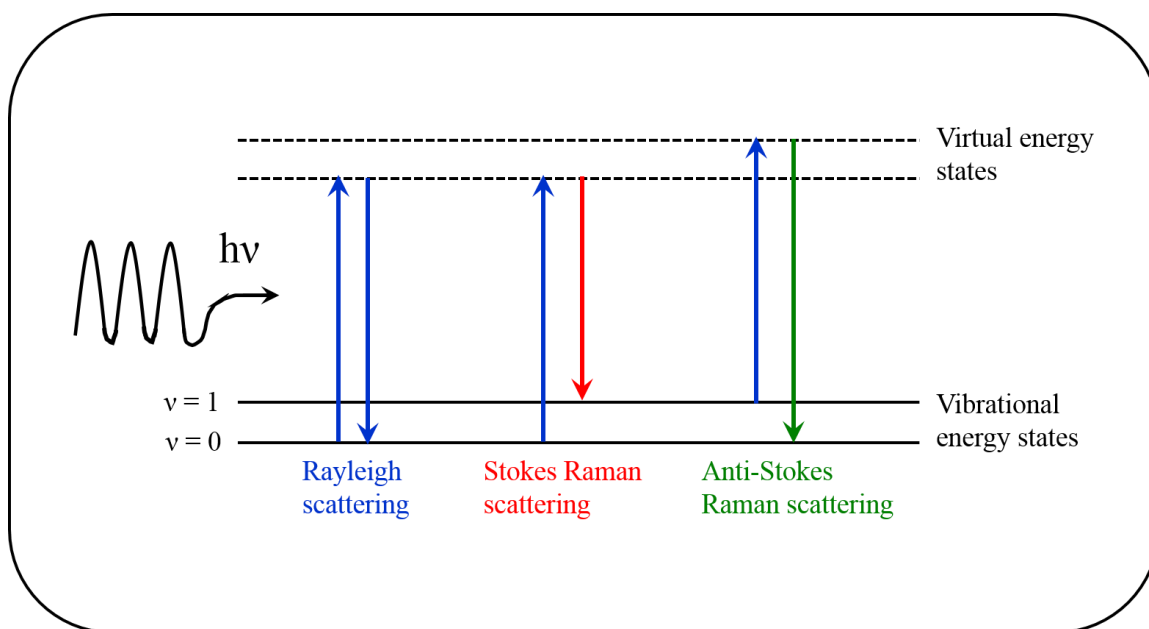
Figure 4.3: Schematic of various light scattering process exhibiting elastic Rayleigh and inelastic Stokes and Anti-Stokes Raman scattering.
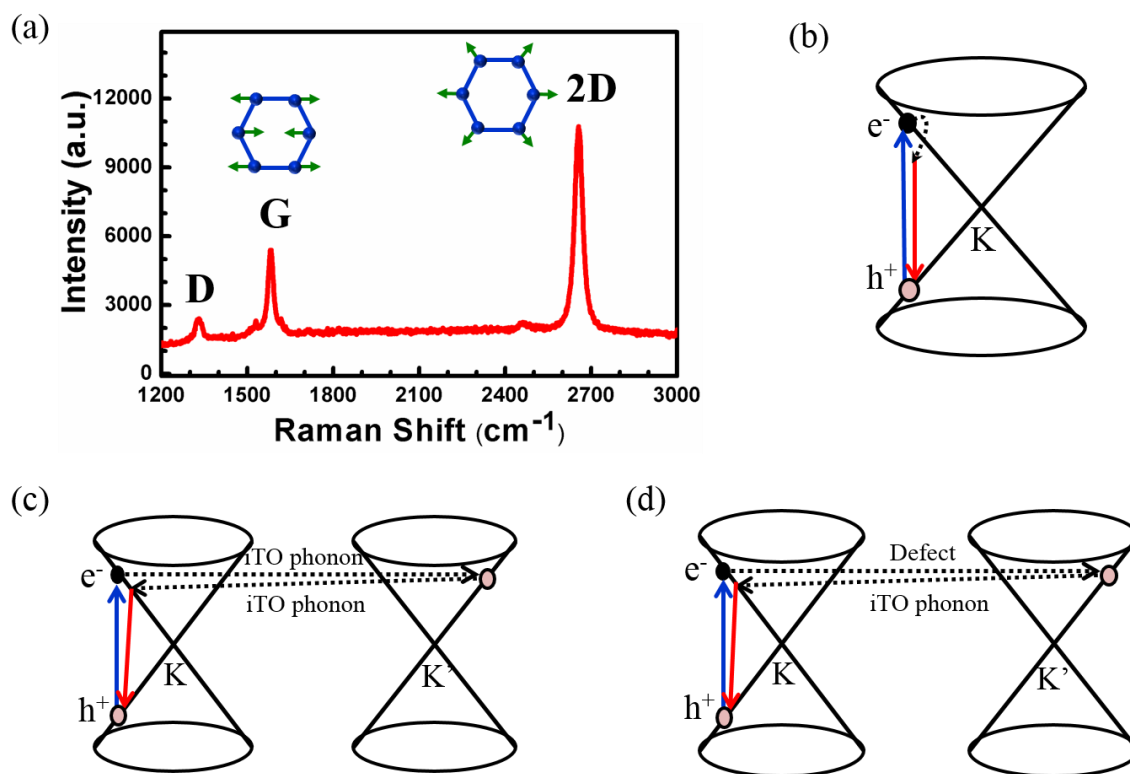
Figure 4.4: (a) Typical Raman spectrum of monolayer graphene with illustration of the atomic vibrations for the G and 2D peaks. This spectrum is taken on CVD graphene transferred onto a SiO$_2$ substrate with 633 nm laser wavelength. Presence of a small D peak at 1330 cm^{-1} is an indication of minor defects in this graphene sample. A schematic diagram of scattering process involved in (b) first order G band, (c) second order double resonance Raman process of 2D band and (c) second order double resonance Raman process of D band (Adapted from ref. [12]). Here, cones representing the linear dispersion of graphene at the k and k' points in the first BZ. The blue and red arrows correspond to the creation and recombination of an electron-hole pair by absorption and scattering of a photon respectively. The dashed arrows represent the inelastic scattering from phonons or the elastic scattering from defects.

Chapter 5

Polarization Induced Doping in Graphene/H-SiC Heterostructures

5.1   Introduction

At a graphene-semiconductor junction, the relative values of the work functions of graphene, Φ_G, and the semiconductor, Φ_S, determines whether graphene is effectively p-type ($\Phi_G < \Phi_S$) or n-type ($\Phi_G > \Phi_S$) doped. For the polar semiconductor SiC, both possibilities occur as shown in Fig. 5.1. The calculated work functions for H-terminated 6H-SiC are 6.09 eV and 3.98 eV for the Si- and C- face, respectively [1]. The work function for monolayer graphene is 5.13 eV, which is calculated with a lattice constant of 2.66 Å matching the SiC substrate (compared to 4.54 eV for the equilibrium lattice constant 2.46 Å of graphene). On Si-face SiC, the Fermi level of pristine graphene falls in the middle of the SiC gap because the Dirac energy (E_D) of graphene is smaller than the valence band maximum (E_{VBM}) of intrinsic SiC i.e. $E_D < E_{VBM}$, thus graphene should be p-type doped. Whereas on C-face SiC, the Fermi level of graphene is below the top of the valence band because $E_D > E_{VBM}$, thus graphene should be n-type doped.

In this chapter, we experimentally demonstrate the polarization doping in the graphene/H-terminated SiC heterostructures. We first prepare wafer sized epitaxial graphene directly on top of SiC by thermal decomposition [2, 3]. On Si-face SiC, the growth of graphene starts with a warped interface layer having a ($6\sqrt{3} \times 6\sqrt{3}$) structure which remains at the interface during subsequent layer growth [4, 5]. The interfacial layer is partially bound to the SiC substrate through Si dangling bonds as shown in Fig. 3.2(d). This leads to the n-type doping in epitaxial graphene/SiC(0001) with the Dirac point (E_D)

~ 0.45 eV below the Fermi level [Fig. 5.4(a)], which is opposed to the expectation from the work function calculations. The origin of the n-type doping is likely the electron transferred to the graphene layers from the Si dangling bonds [6]. Recent work has indeed shown that intercalation of H atoms at the interface can saturate the Si dangling bonds and decouple the epitaxial graphene from the SiC substrate [7-10]. As a result, the interface layer and the first graphene layer turns into first and second QFS graphene layer, respectively [Fig. 3.2(e)]. After H-intercalation, the doping of epitaxial graphene/SiC(0001) changes from n-type to p-type, as revealed by angle-resolved photoemission spectroscopy (ARPES) and transport measurements [7-9].

Here we confirm the n- to p-type conversion by H-intercalation in epitaxial graphene on Si- face SiC by Raman spectroscopy and STM/STS at the atomic scale. We further find that charge carrier density reduces when number of QFS graphene layer increases, similar to that of as grown epitaxial graphene. We also observe the formation of graphene ripples in QFS graphene, likely caused by the negative thermal expansion coefficient of graphene. These atomic scale topographic height variations lead to local fluctuations in the Dirac point that directly follows the undulations of the ripples, which is in direct contrast to the case of exfoliated graphene transferred onto a SiO_2 substrate [11, 12].

On the C-face SiC, similar approach fails to prepare H-intercalated QFS graphene, which should exhibit n-type doping. This is because the growth mechanism and electronic properties of epitaxial graphene grown by thermal decomposition on Si- and C-face of SiC are significantly different [13]. On C- face SiC, the absence of the interface layer results in growth of multilayer graphene (> 10 layers) with rotational disorder [14]. Each layer of the

multilayer graphene is decoupled and behave as a monolayer graphene. As the polarization induced charges are distributed among the multilayers, the top layer is found to be intrinsic with no doping [14]. Thus, a direct comparison between the H-intercalated and as-grown epitaxial graphene on the C-face of SiC is not viable.

Alternatively, we prepare graphene/H-terminated SiC heterostructures by directly transferring the CVD graphene onto H-terminated Si- and C-faces of hexagonal SiC, prepared by H-etching at 1600 ^{o}C in Ar/H$_2$ atmosphere. Raman spectroscopy measurements confirm that the transferred CVD graphene is free standing and under similar stress on both the substrates, thereby, allowing a direct comparison of graphene properties on the SiC surfaces of opposite polarization. STS spectra of the CVD graphene exhibit the Dirac point position above (below) the Fermi level for Si-face (C-face) SiC, which indicate a p-type (n-type) doping in graphene, confirming the polarization induced doping model [Fig. 5.1].

5.2   Experimental Results

5.2.1 As grown and H-intercalated epitaxial graphene/SiC (0001)

Figure 5.2 shows the Raman spectra of SiC substrate, as-grown and H-intercalated epitaxial graphene on the Si-face SiC. The SiC spectra has several features in the range of 1400 - 1800 cm^{-1}, attributed to transverse optical phonon replica and optical phonons [15]. Clearly absent is the defect induced D band at ~1350 cm^{-1} in both materials, indicating that no additional defects are introduced during the hydrogen intercalation process. Red shifts are found for both the in-plane vibrational G band and the two-phonon 2D band for H-intercalated graphene compared to the as-grown. The G band is at 1587 cm^{-1} with a shift

of 10 cm^{-1}, and 2D band appears at 2682 cm^{-1} with a shift of 18 cm^{-1} [Fig. 5.2(a)]. These shifts can be caused by either strain or charge transferred from the underlying substrate [16], with doping-induced shift strongest for G peak [17], and strain-induced more pronounced in 2D peak [18]. Compared to the G peak position at 1582 cm^{-1} for undoped and unstrained graphene, the carrier concentrations in our as-grown and H-intercalated graphene are estimated to be ~ $1.0 \times 10^{13}\ cm^{-2}$ and ~ $0.4 \times 10^{13}\ cm^{-2}$, respectively [17].

Since doping effect is negligible on the 2D band position for carrier concentrations less than ~$3.2 \times 10^{13} cm^{-2}$, shifts in the 2D band is a good indicator of strain in graphene [17]. Raman spectroscopy measures the sum of the interface layer and 1st layer graphene, and therefore in principle difficult to delineate contributions from each layer. However, the red shift of the 2D peak of the H-intercalated graphene compared to the as-grown suggests that compressive strain is released and interaction between graphene and SiC substrate is now weaker.

FWHM of the 2D peak of as-grown epitaxial graphene is 56 cm^{-1}, and can be fitted with four Lorentzian peaks, suggesting bilayer graphene. This is consistent with that epitaxial graphene is grown on top of a warped buffer layer [5]. This is further broadened to 76 cm^{-1} after H-intercalation [Fig. 5.2(b)], indicating that the effective no. of graphene layers has increased as a result of the conversion of the warped interface layer into QFS graphene, consistent with ARPES results [7]. This is further supported by the fact that the intensity ratio of 2D to G peak (I_{2D}/I_G=0.5) is less than one, signature of multilayer graphene.

The change in structural and electronic properties of graphene upon H-intercalation is investigated by STM/STS. Figure 5.3(a) is an STM image of as-grown epitaxial graphene, showing the coexistence of 1st graphene layer and the interface structure that exhibits a different contrast (marked by an arrow), which typically occurs at the early stages of growth [5, 19]. Figure 5.3(b) is a close-up view of the interface layer, showing a honeycomb-like structure with a periodicity ~ 19 Å, i.e., about 6 times the (1×1) lattice spacing of SiC(0001). An atomic resolution image of the 1st graphene layer in Fig. 5.3(c) shows the characteristic honeycomb structure superimposed on top of a larger periodic undulation consistent with the underlying interface layer.

After hydrogen intercalation, the interface layer and 1st graphene layer turns into QFS graphene and QFS bilayer graphene, respectively, as shown in Fig. 5.3(d). In addition, random ripples are also observed in both layers, as can be more clearly seen in the atomic resolution images in Fig. 5.3(e)-(g). The QFS graphene is typically found at the bottom of pits, and exhibits ripples with lateral and vertical length scales of ~3 nm and ~0.2 nm, respectively. The QFS bilayer graphene exhibits a closed-pack structure, consistent with AB stacking [Fig 5.3(e)]. In addition, it shows a more complex morphology, generally with ripples of lateral length scale >10 nm on larger terraces [Fig. 5.3(f)]. On narrow terraces such as that marked by a blue arrow in Fig. 5.3(d), the ripples can exhibit similar characteristics as that of the QFS graphene. Figure 5.3(e) shows the co-existence of QFS 1st and bilayer graphene on the same SiC terrace, where line profile indicates a height difference of 0.08 nm; consistent with that between the interface and 1st layer for as-grown epitaxial graphene on SiC(0001) [20]. QFS bilayer graphene can also be seen over a SiC step (0.25 nm), where the lower terrace exhibits ripples similar to that of QFS 1st layer

graphene, while the upper terrace is flat [Fig. 5.3(g)]. As the QFS bilayer graphene exhibits such complex morphologies, a more definitive identification of QFS graphene layers can be made by dI/dV spectroscopy, as discussed below.

The formation of these ripples is consistent with the negative coefficient of thermal expansion of graphene [21], and the fact that H-intercalated graphene layers are decoupled from the SiC substrate and therefore less strained as indicated in Raman spectroscopy [Fig. 5.2]. During sample cooling following the H-intercalation at 800 °C, the QFS graphene is now more susceptible to deformation. The different length scale of the ripples in the 1st and 2nd layer graphene suggests that while the coupling between the graphene layers is weak vdW, the interaction between the 1st layer graphene and H-terminated SiC is likely stronger.

The change in electronic properties after H-intercalation is probed by tunneling spectroscopy, as shown in Fig. 5.4. The dI/dV spectrum for the as-grown 1st graphene layer exhibits two characteristic minima at zero bias (Fermi level) and at -0.45 eV [Fig. 5.4(a)]. The later one is attributed to the Dirac point, indicative of n-type doping, while the gap at Fermi level is caused by phonon assisted inelastic tunneling [22]. For the 2nd layer graphene the Dirac point shifts closer to the Fermi level and appears at -0.35 eV [Fig. 5.4(a)], consistent with earlier ARPES and STS results [23, 24]. After H-intercalation, while the phonon gap is unchanged, the second minimum is now above the Fermi level [Fig. 5.4(b)], indicative of p-type doping, consistent with transport measurements [9]. For the QFS 1st and 2nd layer graphene the Dirac points appear at 0.32 and 0.20 eV, respectively. For the QFS 3rd layer graphene, the spectra exhibit a parabolic shape with no discernable

Dirac point. This is consistent with the shift of Dirac point towards the Fermi level and falls within the phonon gap as the number of graphene layer is increased.

Quantitatively, the carrier densities of as-grown 1st layer epitaxial graphene and QFS graphene are calculated to be $n = 1.48 \times 10^{13} cm^{-2}$ (electron) and $p = 0.75 \times 10^{13} \text{cm}^{-2}$ (hole), respectively, using the relation $n(p) = 4 \pi E_D^2/(\hbar v_f)^2$, in agreement with Raman results. Clearly, the charge carrier type in graphene has changed from electron to hole after H-intercalation with a reduced carrier density.

The impact of ripples on the electronic properties of H-intercalated graphene is revealed by spatially resolved dI/dV measurements. Shown in Fig. 5.5(a) is an STM image of QFS bilayer graphene, where the peak-to-valley height variation is ~1.5 Å. dI/dV spectra taken along the dashed line at locations 1-4 across a ripple are shown in Fig. 5.5(b). Atop the ripple (spectrum *1)*, the Dirac point is at 219 meV above the Fermi level, which shifts towards the Fermi level (204 meV) near the edge of the ripple (spectrum *2)*. At the bottom of the ripple, the Dirac point appears at 191 meV (spectrum *3)*, and moves back to 219 meV atop another ripple. These changes of E_D are plotted in Fig. 5.5(c) along the line profile. They represent carrier fluctuations in the range of $1.65 \times 10^{10} \text{cm}^{-2}$. The variations in the Dirac point precisely follow the undulation of the ripples, which is clearly different than that observed on graphene transferred on SiO_2 substrates where a correlation to charge impurities in the SiO_2 is found [11].

The Dirac point fluctuations found here reflects an intrinsic effect inherent to the H-intercalated epitaxial graphene/SiC, where charge impurities in the SiC substrate are not expected to exist in great quantities, but the formation of ripples is to be expected due to the mismatch in the thermal expansion coefficient between graphene and SiC [25].

Nonetheless, similar to the SiO_2 case, these local fluctuations in the Dirac point can make the charge neutrality point challenging to reach [26].

5.2.2 CVD graphene transferred on H-terminated Si- and C-face SiC

Figure 5.6 shows the Raman spectra of 6H-SiC(0001) substrate and CVD graphene transferred on Si- and C-faces SiC. Again, the SiC spectrum exhibits several features between 1400 and 1800 cm^{-1}, attributed to optical phonons and transverse optical phonon replica [15]. The transferred graphene exhibits three additional peaks, which can be more clearly seen in the substrate-subtracted spectra [Fig. 5.6(b)]. These peaks, located at 1326, 1582, and 2655 cm^{-1}, are attributed to the defect-induced D band, the in-plane vibrational G band, and the two-phonon 2D band, respectively. The G bands ($1582 \pm 2cm^{-1}$) and 2D bands ($2655 \pm 2cm^{-1}$) of graphene on both the Si- and C-faces exhibit the same frequency, indicating that they are under similar stress [18]. The FWHM of the 2D bands are 40 and 42 cm^{-1} for the Si- and C-faces, respectively, consistent with single layer graphene. Raman spectra of CVD graphene transferred on SiO_2 substrate is also shown in Fig. 5.6(b), where 2D bands of graphene/SiC are shifted ~10 cm^{-1} towards higher wave number compared to graphene/SiO_2 that indicates a relative strong interaction between graphene and SiC substrate. The intensity ratio of the 2D to G peaks (I_{2D}/I_G=0.8) is less than one, a signature of doping in graphene [17]. In addition, the presence of the D band at ~1326 cm^{-1} in both cases indicates the presence of residual defects in the graphene.

The electronic properties of the transferred CVD graphene/SiC are investigated by tunneling spectroscopy. Figure 5.7(a) shows a typical dI/dV spectrum taken on graphene/C-face SiC, which exhibit a gap of ~130 meV at zero bias because of phonon assisted inelastic tunneling in graphene [22]. Outside the gap, a local minima at ~ -0.39 eV

is also evident which corresponds to the Dirac point. For graphene/Si-face SiC, while the phonon gap at the Fermi level is unchanged, the Dirac point is above the Fermi level at ~ 0.35 eV [Fig. 5.7(b)]. These results indicate that CVD graphene on C- and Si-faces SiC is n- and p-type doped, respectively, consistent with the DFT calculations shown in Fig. 5.1. The electron and hole carrier densities of graphene on C- and Si-face SiC are calculated to be $n = 1.12 \times 10^{13} cm^{-2}$ and $p = 0.90 \times 10^{13} cm^{-2}$, respectively.

5.3 Discussion

In the Raman spectra of H-intercalated QFS graphene and CVD graphene/Si-face SiC, the 2D peaks appear at 2682 cm^{-1} and 2655 cm^{-1} with a red shift of 18 cm^{-1} and 45 cm^{-1} compared to as-grown epitaxial graphene, respectively. The relatively smaller red shift for the QFS graphene indicates that it is not completely free standing, and still weakly interacts with the SiC substrate.

The dI/dV spectra of CVD graphene/Si-face SiC is qualitatively similar to that of H-intercalated QFS graphene, with the phonon gap at zero bias and the Dirac points above the Fermi level. The position of the Dirac point for the monolayer CVD graphene is at ~ 0.35 eV compared to ~ 0.32 eV for 1st layer QFS graphene, with 20% higher hole carrier densities. The relatively smaller hole density in the QFS graphene can be explained by the weak interaction with the substrate and possible electron transfer through the residual Si dangling bonds at the interface, as suggested by Raman measurements.

QFS graphene suffers from random ripples formation due to negative thermal expansion coefficient of graphene and weak interaction with the SiC substrate. Interestingly, the variations in the Dirac point precisely follow the undulation of the ripples.

This is due to the fact that the origin of doping in graphene on SiC is the spontaneous polarization of the substrate. Due to the formation of a Schottky dipole at the graphene/SiC interface, the Dirac point depends strongly on the spacing between graphene and SiC [1]. As a result, ripples, i.e., spatial fluctuation of graphene with respect to the substrate leads to the variations in the Dirac point.

In conclusion, charge carrier type in epitaxial graphene/SiC(0001) convert from n- to p-type upon H-intercalation at the interface. By transferring CVD graphene onto H-terminated Si-face and C-face of hexagonal SiC, we experimentally demonstrate the SiC substrate polarization induced doping of graphene. Additionally, we observe the formation of ripples in the H-intercalated graphene, which causes local fluctuations in the Dirac point, thus forms electron and hole puddles that can limit carrier mobility [27].

References

1. S. Rajput, M. Chen, Y. Liu, Y. Y. Li, M. Weinert and L. Li. Spatial fluctuations in barrier height at the graphene-silicon carbide Schottky junction. *Nat. Comm.* **4,** 2752 (2013).

2. A. J. van Bommel, J. E. Crombeen and A. van Tooren. LEED and Auger electron observation of the SiC(0001) surface. *Surf. Sci.* **48,** 463 (1975).

3. K.V. Emtsev *et al.* Towards wafer-size graphene layers by atmospheric pressure graphitization of silicon carbide. *Nat. Maters.* **8,** 203 (2009).

4. C. Reidl, U. Starke, J. Bernhardt, M. Franke and K. Heinz. Structural properties of the graphene-SiC(0001) interface as a key for the preparation of homogeneous large-terrace graphene surfaces. *Phys. Rev. B* **76**, 245406 (2007).

5. Y. Qi, S. H. Rhim, G. F. Sun, M. Weinert and L. Li. Epitaxial graphene on SiC (0001): more than just honeycombs. *Phys. Rev. Lett.* **105,** 085502 (2010).

6. S. Kopylov, A. Tzalenchuk, S. Kubatkin and V. I. Falko. Charge transfer between epitaxial graphene and silicon carbide. *Appl. Phys. Lett.* **97,** 112109 (2010).

7. C. Reidl, C. Coletti, T. Iwasaki, A. A. Zakharov and U. Starke. Quasi-free standing epitaxial graphene on SiC obtained by H$_2$ intercalation. *Phys. Rev. Lett.* **103,** 246804 (2009).

8. S. Forti, K. V. Emtsev, C. Coletti, A. A. Zakharov, C. Riedl and U. Starke. Large area homogeneous quasi-free standing epitaxial graphene on SiC(0001): Electronic and structural characterization. *Phys. Rev B* **84,** 125449 (2011).

9. F. Speck *et al.* The quasi-free-standing nature of graphene on H-saturated SiC(0001). *Appl. Phys. Lett.* **99,** 122106 (2011).

10. J. Ristein, S. Mamadov and Th. Seyller. Origin of doping in quasi-free standing graphene on silicon carbide. *Phys. Rev. Lett.* **108,** 246104 (2012).

11. Y. Zhang, V. W. Brar, C. Girit, A. Zettl and M. F. Crommie. Origin of spatial charge inhomogeneity in graphene. *Nat. Phys.* **5,** 722 (2009).

12. A. Deshpande, W. Bao, F. Miao, C. N. Lau and B. J. LeRoy. Spatially resolved spectroscopy of monolayer graphene on SiO$_2$. *Phys. Rev. B* **79,** 205411 (2009).

13. K. V. Emtsev, F. Speck, Th. Seyller and L. Ley. Interaction, growth and ordering of epitaxial graphene on SiC surfaces: A comparative photoelectron spectroscopy study. *Phys. Rev. B* **77,** 155303 (2008).

14. J. Hass *et al.* Why multilayer graphene on 4H-SiC(000$\bar{1}$) behaves like single sheet of graphene. *Phys. Rev. Lett.* **100,** 125504 (2008).

15. J. C. Burton, L. Sun, F. H. Long, Z. C. Feng and I. T. Ferguson. First- and second-order Raman scattering from semi-insulating 4H−SiC. *Phys. Rev. B* **59,** 7282 (1999).

16. D. A. Schmidt, T. Ohta and T. E. Beechem. Strain and charge carrier coupling in epitaxial graphene. *Phys. Rev. B* **84,** 235422 (2011).

17. A. Das *et al.* Monitoring dopant by Raman scattering in an electrochemically top-gated graphene transistor. *Nat. Nanotech.* **3,** 210 (2008).

18. Z. H. Ni *et al.* Raman spectroscopy of epitaxial graphene on a SiC substrate. *Phys. Rev. B* **77,** 115416 (2008).

19. G. F. Sun, Y. Liu, S. H. Rhim, J. F. Jia, Q. K. Que, M. Weinert and L. Li. Si-diffusion path for pit free graphene growth on SiC(0001). *Phys. Rev. B* **84,** 195455 (2011).

20. H. Huang, W. Chen, S. Chen and A. T. S. Wee. Bottom-up growth of epitaxial graphene on 6H-SiC(0001). *ACS Nano* **2,** 2513 (2008).

21. W. Bao, F. Miao, Z. Chen, H. Zhang, W. Jang, C. Dames and C. N. Lau. Controlled ripple texturing of suspended graphene and ultrathin graphite membranes. *Nat. Nanotech.* **4,** 562 (2009).

22. Y. Zhang *et al.* Giant phonon-induced conductance in scanning tunneling spectroscopy of gate-tunable graphene. *Nat. Phys.* **4,** 627 (2008).

23. T. Ohta, A. Bostwick, J. L. McChesney, T. Seyller, K. Horn and E. Rotenberg. Interlayer interaction and electronic screening in multilayer graphene investigated with angle-resolved photoemission spectroscopy. *Phy. Rev. Lett.* **98,** 206802 (2007).

24. P. Lauffer, K. V. Emtsev, R. Graupner, Th. Seyller and L. Ley. Atomic and electronic structure of few-layer graphene on SiC(0001) studied with scanning tunneling microscopy and spectroscopy. *Phys. Rev. B* **77,** 155426 (2008).

25. N. Ferralis, R. Maboudian and C. Carraro. Evidence of structural strain in epitaxial graphene layers on 6H-SiC(0001). *Phys. Rev. Lett.* **101**, 156801(2008).

26. S. D. Sarma, S. Adam, E. H. Hwang and E. Rossi. Electronic transport in two-dimensional graphene. *Rev. Mod. Phys.* **83**, 407 (2011).

27. J. Martin *et al.* Observation of electron–hole puddles in graphene using a scanning single-electron transistor. *Nat. Phys.* **4,** 144 (2008).
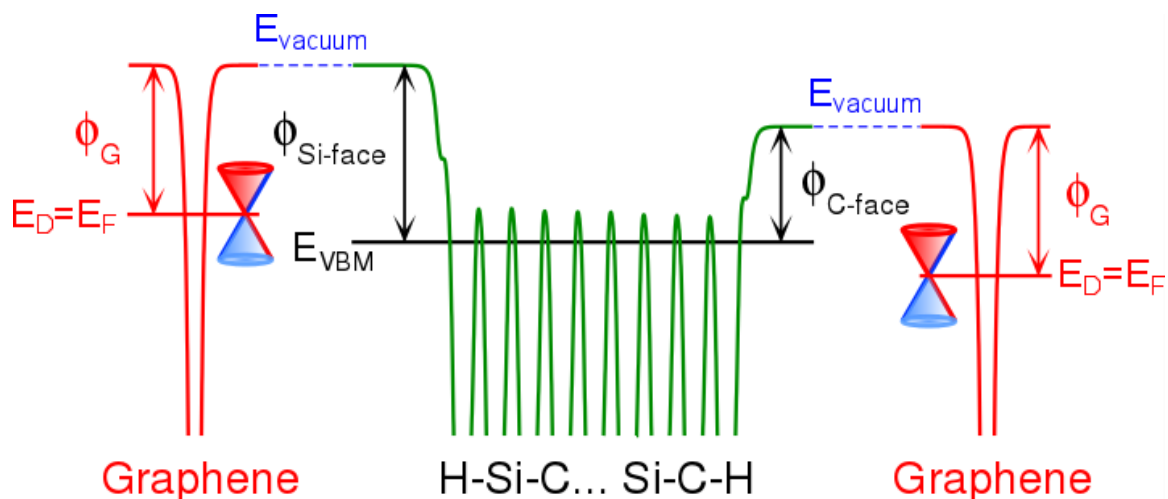
Figure 5.1: Band alignment of graphene and H-terminated 6H-Si face SiC(0001) and 6H-C face SiC(000$\bar{1}$). Graphene is p- and n-type doped on Si- and C-face SiC substrates respectively, because of the relative work function difference such as $\Phi_G < \Phi_{si\text{-}face}$ and $\Phi_G > \Phi_{c\text{-}face}$.
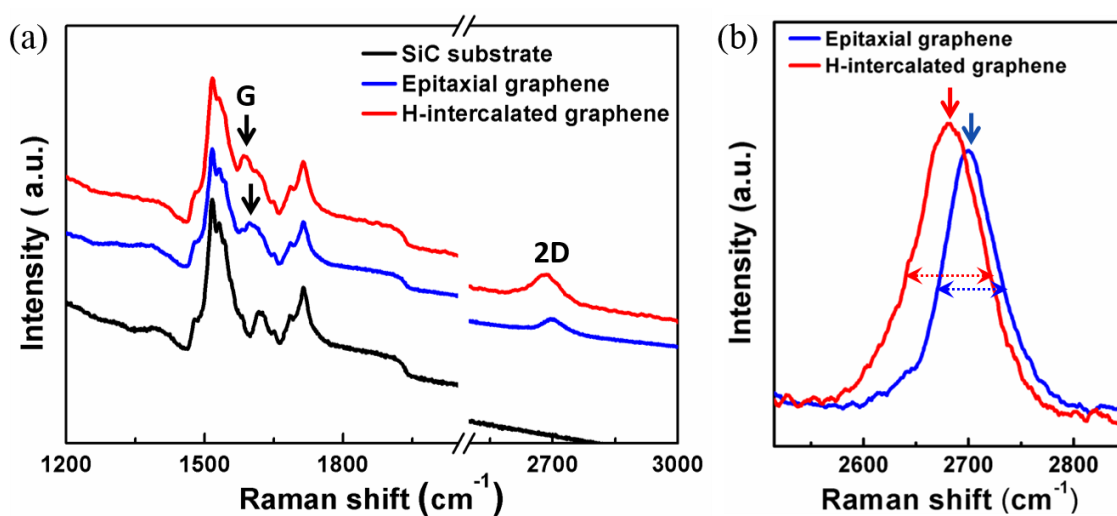
Figure 5.2: (a) Raman spectra of the SiC substrate, as-grown, and H-intercalated epitaxial graphene on Si-face SiC(0001). (b) Close-up view of the 2D bands of the as-grown and H-intercalated epitaxial graphene on SiC(0001) after subtracting baseline and SiC substrate contributions.
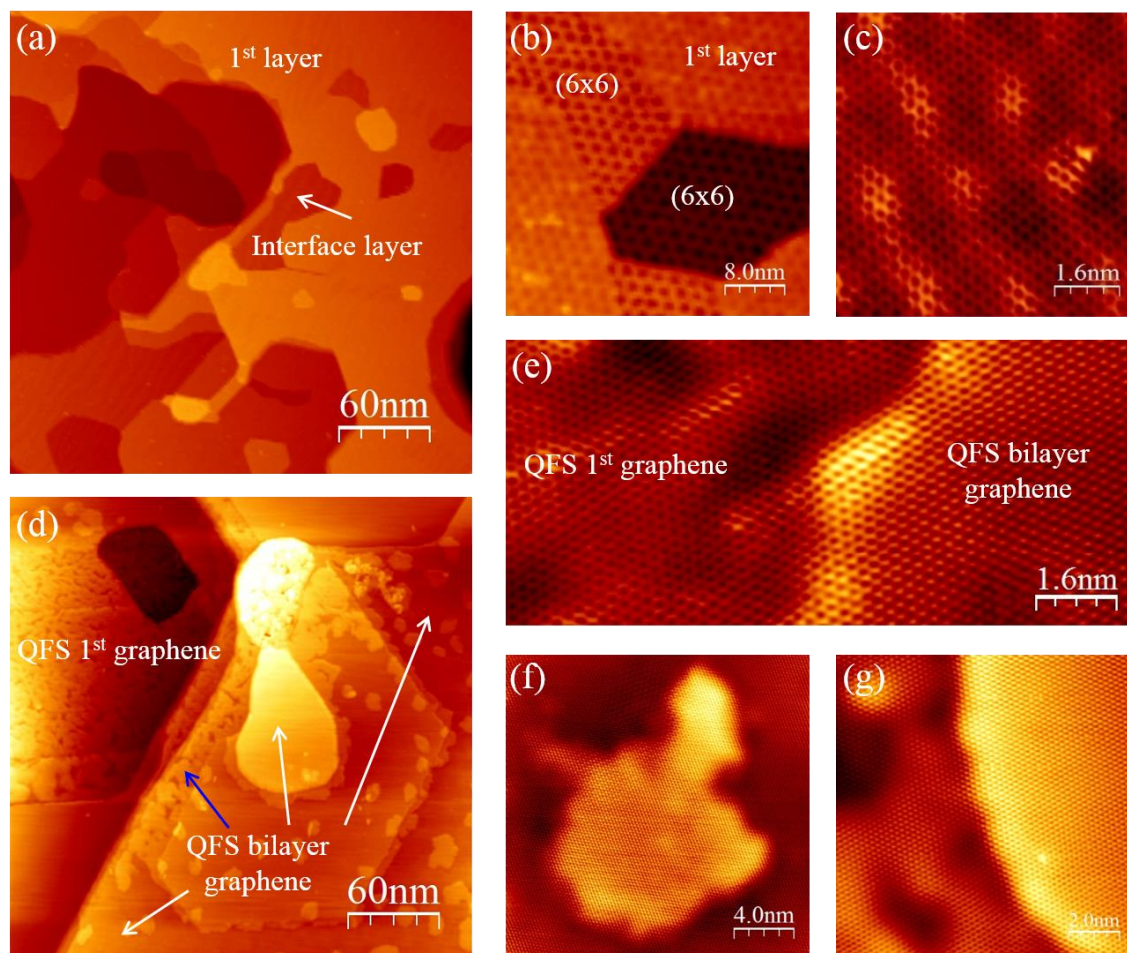
Figure 5.3: (a) STM image of epitaxial graphene on Si-face SiC(0001), showing the coexistence of the interface and 1st graphene layers (I$_t$ =0.5 nA, V$_s$ = -0.2 V). Atomic resolution images of (b) the (6x6) reconstructed interface layer (I$_t$ = 0.5 nA, V$_s$ = -0.2 V), and (c) the 1st graphene layer (I$_t$ = 1.0 nA, V$_s$ = -0.1 V). (d) STM image of the H-intercalated epitaxial graphene on Si-face SiC(0001) with arrows pointing to different regions of QFS bilayer (I$_t$ = 0.1 nA, V$_s$ = -1.51 V). (e) Atomic resolution image of QFS 1st and bilayer graphene on the same SiC terrace (I$_t$ = 0.6 nA, V$_s$ = -0.9 V).) Atomic resolution image of QFS bilayer graphene, showing (f) a large ripple (I$_t$ = 0.1 nA, V$_s$ = -0.01 V) and (g) rippled and flat areas separated by a SiC step (I$_t$ = 0.3 nA, V$_s$ = -0.3 V).
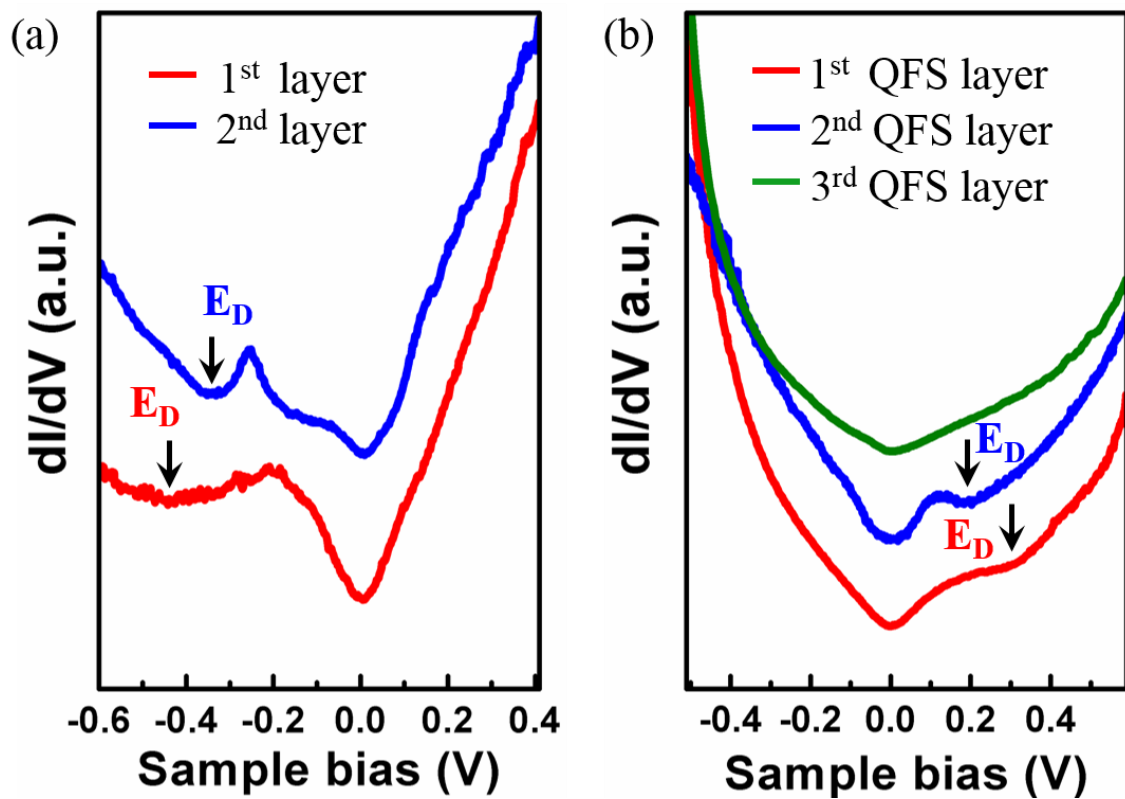
Figure 5.4: Layer dependent dI/dV spectra of (a) as-grown and (b) H-intercalated epitaxial graphene on Si-face SiC(0001) with Dirac points marked.
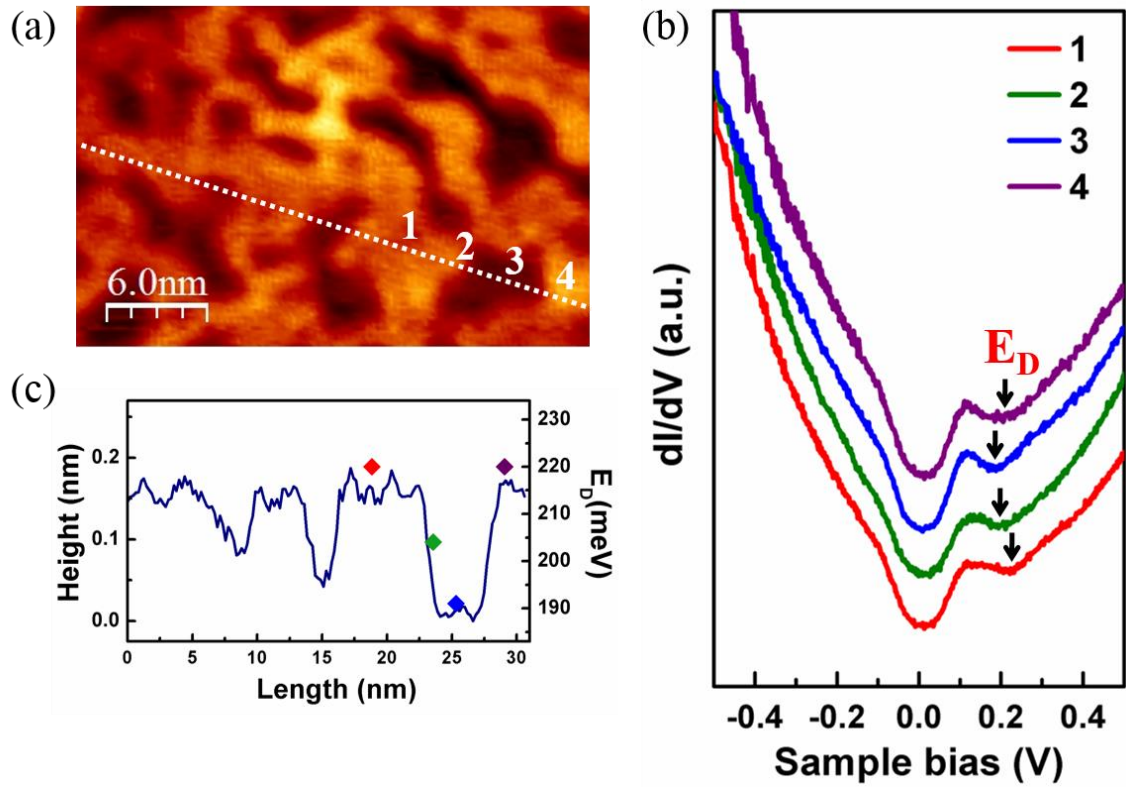
Figure 5.5: (a) STM image of ripples in QFS bilayer graphene (I_t = 0.1 nA, V_s = -0.8 V). (b) Spatially resolved dI/dV spectra taken at positions 1-4 marked in (a). (c) Line-profile and plot of E_D at positions 1-4, showing the fluctuations of E_D directly follow the undulations of the graphene ripples.
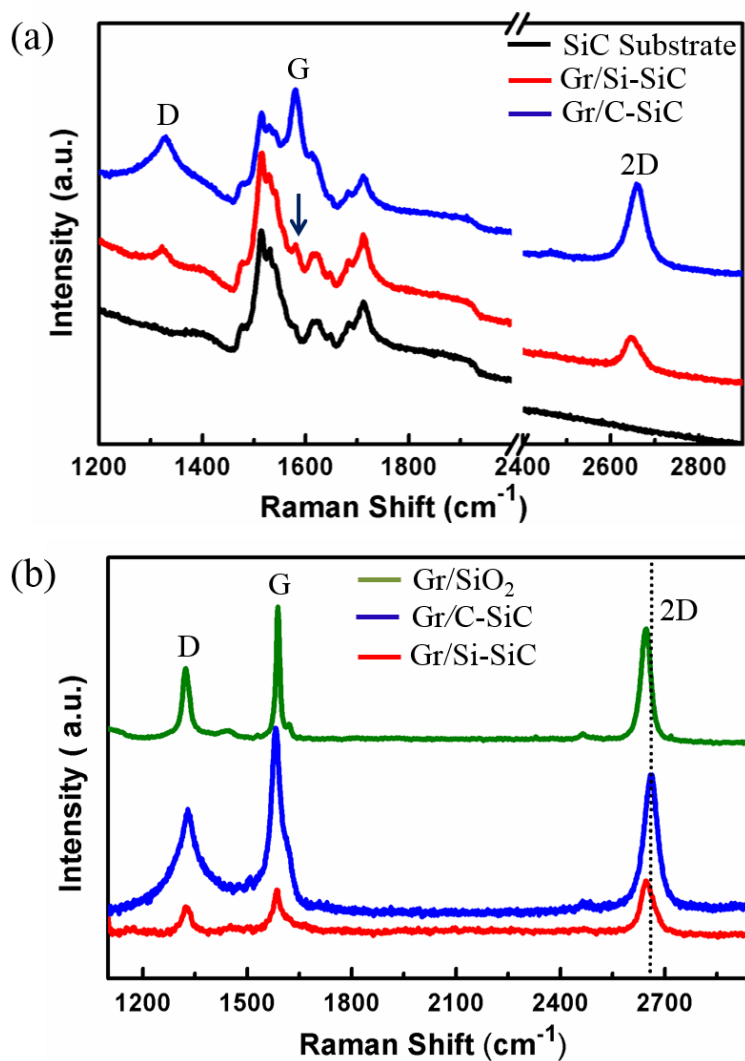
Figure 5.6: (a) Raman spectra of the SiC substrate and CVD graphene transferred on Si and C-face of SiC (b) Raman spectra of graphene on SiO2/Si and the Si- and C-faces of SiC after subtracting baselines and substrate contributions.
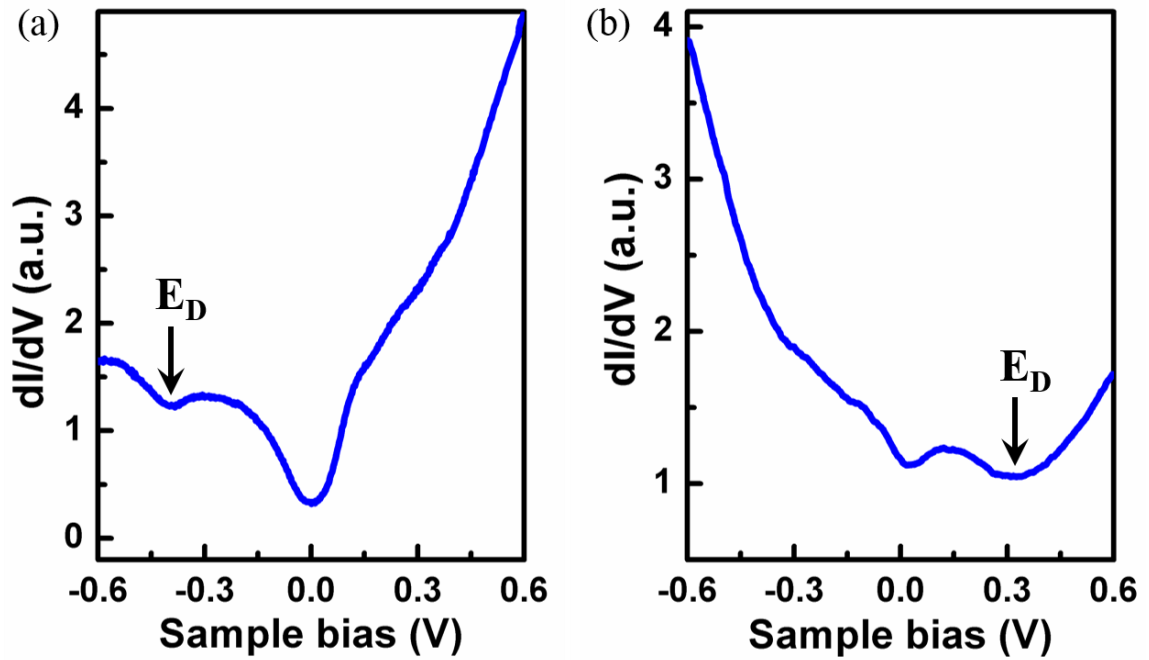
Figure 5.7: dI/dV spectra of CVD graphene transferred on H-terminated (a) C-face SiC(000$\bar{1}$) and (b) Si-face SiC(0001) substrates with the Dirac points marked.

Chapter 6
Spatial Fluctuations in Schottky Barrier Height at Graphene-Semiconductor Junctions

6.1   Introduction

When graphene is interfaced with a semiconductor, Schottky barrier forms at the graphene/semiconductor junction with rectifying properties [1]. Unlike conventional metal-semiconductor junctions, the graphene variant offers a unique advantage of field tunable Fermi level [2], thus the Schottky barrier height, that enables novel applications such as solar cells [3], photodetectors [4], Schottky diodes [5], and most notably three-terminal transistors with 10^6 on/off ratio [6, 7]. To first order, the Schottky barrier height is given simply by the work function difference of graphene and the semiconductor [8], or equivalently the difference between the Dirac energy (E_D) of graphene and the valence band maximum (E_{VBM}) of an intrinsic semiconductor. However, the barrier modifies for an interacting system by the interface Schottky dipole that arises from the charge rearrangements at the junction [9]. This is of particular significance for graphene because of the large polarizability of the π orbitals by an electric field [10], either external or due to the surface dipole of the semiconductor.

Furthermore, the Schottky barrier height is typically derived by assuming a perfect homogeneous interface. Graphene, however, is prone to deformation in the direction normal to its surface, i.e., the formation of ripples when in contact with another material [11-14], or when placed under an applied electric field [15, 16], which causes spatial inhomogeneities at graphene/semiconductor interface. As these ripples are expected to

modulate graphene's electronic properties [17-19], one critical question is whether they will impact the Schottky barrier formation at the graphene/semiconductor junction.

In this chapter, we present an atomic scale study of the Schottky barrier formation at graphene-semiconductor junctions using STM/STS combined with DFT calculations. We investigate graphene Schottky junctions on Si- and C-face SiC, Si and GaAs semiconductors, and discover two types of intrinsic atomic-scale inhomogeneities, graphene ripples and/or trapped charge impurities and surface states in the semiconductor, that can cause fluctuations in the Schottky barrier height at graphene/semiconductor junctions.

6.2   Results

6.2.1 Graphene-SiC junction

Atomically flat H-terminated SiC surfaces, that are free of dangling bonds and charge traps, are prepared by hydrogen etching process described in Chapter 3. Then CVD graphene is transferred onto the H-terminated SiC substrates using polymer assisted process. The surface morphology of transferred graphene is characterized by STM as shown in Fig. 6.1(a). Clearly evident is a distinct network of graphene ridges 2.7 ± 0.6 nm in height, 23.4 ± 4.7 nm in width, and hundreds of nm in length across the terraces where the underlying SiC substrate steps are still visible. These ridges are bulged regions of graphene [20], originated from the CVD growth and preserved during transfer.

Additional smaller spatial fluctuations (i.e., ripples) are also observed between these ridges as shown in Figs. 6.1(b) and 6.1(c) for graphene transferred onto the Si- and C-faces SiC, respectively. While the graphene honeycomb lattice is clearly continuous

throughout the corrugations [Fig. 6.1(d)], analysis of line profiles [Fig. 6.1(e)] further indicates that the dark areas are likely in contact with the underlying SiC substrate, while the bright regions are buckled up from it, resulting in a warped graphene layer. An average ripple height of 0.33 nm is found for graphene on both substrates [Fig. 6.1(f)]. Similarly, the lateral length scale (measured by the width of the dark region) is found to be 2.5 and 3.1 nm for graphene on the C- and Si-face, respectively [Fig. 6.1(g)]. These results are similar to earlier STM studies of exfoliated graphene transferred onto SiO_2/Si [12-14], suggesting that formation of ripples is universal for graphene transferred onto a substrate, independent of whether the substrate is semiconducting or dielectric.

The electronic properties of the transferred graphene/SiC are further investigated by STS. On the graphene/C-face SiC, all dI/dV spectra exhibit a gap of ~130 meV at zero bias [Fig. 6.1(h)], attributed to phonon assisted inelastic tunneling in graphene [21]. For the dark region, a local minimum at -0.39 eV is attributed to the Dirac point that indicates n-type doping, similar to as shown in the previous chapter. However, for the bright region, the Dirac point is shifted to -0.42 eV, while an additional dip at -0.23 eV also appears. Qualitatively similar line shapes are also observed for graphene/Si-face SiC, except the position of the Dirac point are above the Fermi level for all the spectra, indicating p-type doping [Fig. 6.1(i)]. The local minimum at +0.35 eV identified as the Dirac point for the dark region, with an additional dip at +0.15 eV for the bright region. These results indicate that local DOS of graphene/SiC is different in bright and dark regions of graphene ripples.

To further illustrate the impact of ripples on the Dirac states, Fig. 6.2(a) shows spatially resolved dI/dV spectra taken on graphene/C-face SiC across a ripple at positions marked in Fig. 6.2(b). Again, all spectra exhibit the phonon gap, however, with variations

in the Dirac point. Atop the bright region (spectrum 1), two strong peaks separated by ~0.23 eV (marked by up-pointing arrows) are observed with their separation becoming progressively smaller towards the center of the dark region, where only a broad peak at -0.24 eV is seen (spectrum 9). These two peaks re-emerge as the tip is moved towards the bright region (spectra 10-12). Qualitatively similar spatial variations are also observed for graphene/Si-face [Fig. 6.2 (c)]. These observations clearly show that the spatial variations of the Dirac point directly follow the undulation of the ripples, with Gaussian distributions of FWHM of 42 and 51 meV for graphene on the C-face and Si-face SiC, respectively [Fig. 6.2(e)]. The origin of the two additional peaks in the bright regions is unclear at the present, and are tentatively attributed to either additional states arising from quantum confinement in the buckled-up regions [22, 23], or mid-gap states in curved graphene [17-19].

The local variation in the Dirac point lead to fluctuations in carrier concentration $\Delta n (\Delta p)$ that can be calculated by $\Delta n(\Delta p) = 4\pi (\Delta E_D)^2 / (h v_f)^2$, where v_f is the Fermi velocity of graphene and h the Plank's constant. This yields variations of 1.29×10^{11} cm^{-2} and 1.91×10^{11} cm^{-2} in electron and hole concentrations for graphene on the C-face and Si-face SiC, respectively. These results are in direct contrast to the case for graphene on SiO$_2$/Si substrate, where variations in the Dirac point are attributed to charge impurities in the SiO$_2$ substrate [12-14], and not topographic fluctuations.

To determine the origin of the spatial fluctuations in the Dirac point, and whether they are directly tied to the graphene ripples, we calculate the position of E_D-E_{VBM} − a direct measure of the Schottky barrier − as a function of the separation d between the graphene layer and the SiC substrate, as shown in Fig. 6.3(a) for the Si- and C-faces of 6H-SiC. An immediate observation is that the relative positions of E_D relative to E_{VBM} indicate

that graphene is p-type on Si-SiC and n-type on C-SiC. In addition, the value of E_D-E_{VBM} strongly depends on d, consistent with the experimental observation that E_D fluctuates with graphene ripples. The calculated Schottky barriers (E_D-E_{VBM}) at the equilibrium separations, indicated by dots in Fig. 6.3(a), are 0.78 and 0.49 eV for the Si- and C-face SiC, respectively.

Since the dangling bonds of SiC substrate are saturated by hydrogen, graphene bands around the K point for both faces are basically unaffected by interactions with the SiC states [Fig. 6.3(b)], i.e., graphene is a quasi-free-standing layer. According to work function calculations [Fig. 5.1], $E_D < E_{VBM}$ for the Si-face SiC, no charge transfer is expected since there are no unfilled SiC states below E_D ($=E_F$) for electrons from graphene to flow into. On the other hand, the Dirac point is below E_{VBM} for the C-face, so that states above E_D are now occupied. The calculated E_F for the whole system is ~0.03 eV below E_{VBM}, indicating that there is a hole pocket in the vicinity of the interface.

Next, the modification of the graphene Dirac states due to the electric field arising from the intrinsic surface dipole of the SiC substrate is calculated. The spatial distribution of the calculated planar-average polarization density $\Delta\rho(z)$ for the equilibrium graphene-substrate separations is shown in Fig. 6.3(c), along with the electron density from an isolated graphene layer for comparison. The polarization densities are opposite in sign on either sides of the graphene layer, giving rise to large polarization dipoles. In addition, the fact that $\Delta\rho(z)$ is both larger and of opposite sign for the C-face compared to the Si-face reflects the relative difference between the Dirac point and the Fermi level for the two cases. This large polarization dipole formation in graphene, with $\Delta\rho(z)$ in the interface region orders of magnitude larger than the nominal bulk doping of ~10^{18} cm^{-3} (10^{-6} Å^{-3}), is

a direct consequence of the high polarizability of its π orbitals. Varying the graphene-substrate separation d alters the quantitative values of the polarization densities $\Delta\rho(z)$, but the shapes and qualitative differences between the two faces remain.

The integral of the polarization density $\Delta\rho(z)$ as a function of the distance away from the interface, provides a measure of charge transfer $\Delta q(z)$ to/from graphene as shown in Fig. 6.3(d). The interface is chosen to be at the H plane, rather than the more traditional midpoint between atomic layers, so that the majority of the graphene density is in the "graphene" region. For the Si-face SiC, even though there is little or no overall charge transfer (i.e., $\Delta q \sim 0$ for z far outside the graphene), a region ~10 Å wide with a deficit of electrons (corresponding to a hole doping of $\sim 5 \times 10^{12}$ cm^{-2}) is formed as a result of an image dipole across the interface in the SiC. The graphene layer itself, except for a region just at the interface, is p-doped. Thus, while the coincidence of the Dirac point and the Fermi level indicates no charge transfer [Fig. 6.3(b)], the spatial distribution of the polarization suggests p-type doping of graphene, consistent with earlier transport measurements of H-intercalated epitaxial graphene/Si-face SiC [24].

For the C-face SiC, on the other hand, there is a charge transfer of ~0.05 e$^-$/graphene cell (~10^{13} cm^{-2}), in good agreement with the calculated Dirac point shift of ~0.45 eV relative to the Fermi energy [Fig. 6.3(b)]. The charge transferred to graphene is mainly localized between the graphene and the substrate. To compensate the n-doping of the graphene Dirac states, the SiC has a narrow net p-doped region just beyond the first SiC bilayer, as a result of the n-like image dipole contribution and the p-doping from the image charge.

These polarization densities $\Delta\rho(z)$ directly give rise to changes in the Coulomb potential, shown in Fig. 6.3(e), and the differences between $\Delta V_c(\pm\infty)$ is the Schottky dipole [9]. The spatial extent of the barriers in ΔV_c is only ~10 Å, orders of magnitude smaller than the depletion regions in conventional metal-semiconductor systems [8]. The formation of these highly localized barriers is again a direct consequence of the large polarizability of the graphene π orbitals, and points to opportunities for effectively tuning the barrier height by an applied field in graphene/semiconductor Schottky contacts.

6.2.2 Graphene-Si and -GaAs junction

Hydrogen and sulfur terminated Si and GaAs wafers are prepared by etching in $HF+NH_4F$ (1:7) and NH_4S solutions, respectively [25, 26]. To avoid oxide formation on the surface, monolayer CVD graphene is transferred immediately after cleaning the semiconductor substrates. The surface morphology of graphene transferred onto Si substrate is shown in Fig. 6.4(a). Clearly evident is a non-uniform surface with vertical undulations of ~0.5 nm over length scales of tens of nanometers (marked by a circle), likely due to roughness of the underlying Si substrate. Figure 6.4(b) is a close-up view showing the characteristic graphene honeycomb lattice that is continuous over these fluctuations. These features are similar to graphene transferred onto SiC substrates [Fig. 6.1] and earlier STM studies of graphene ripples [12-14], which are attributed to either graphene in contact with the underlying substrate (dark regions), or buckled up from it (bright regions).

Figure 6.4(c) shows spatially resolved dI/dV spectra taken across a ripple on graphene/Si at locations marked in Fig. 6.4(b). All spectra exhibit two characteristic minima, one at zero bias caused by phonon-assisted inelastic tunneling [21], and the other at negative bias marked by downward arrows attributed to the Dirac point, indicating n-

type doping. Moving from bright to dark to bright regions, while the Dirac point varies between 105 and 130 meV, but no direct correlation is found to the topographic fluctuations, in contrast to the case of graphene transferred on SiC substrates. These variations in the Dirac point lead to fluctuations of 3.79×10^{10} cm^{-2} in electron concentration in graphene/Si. Atop the brightest regions (spectra 1-3 and 7,8) an additional peak also appear, as marked by upward arrows, possibly due to impurity states arising from disorders such as polymer and Cu residues [27], or partial hydrogen termination of the Si substrate.

Similar features are observed for graphene/GaAs junction as shown in Fig. 6.5(a). Large scale corrugations of ~ 1 nm in height and hundreds of nm in width likely originated from the substrate roughness. At the atomic scale, ripples ~ 0.35 nm in height are also seen [Fig. 6.5(b)]. A series of dI/dV spectra, taken at positions 1-11 in Fig. 6.5(b), are shown in Fig. 6.5(c). While all spectra exhibit the similar phonon-assisted inelastic tunneling at zero bias [21], the Dirac point (marked by downward arrows) is now above the Fermi level, indicative of p-type doping. Again, fluctuations in Dirac energy, E_D, between 110 and 160 meV are also observed, but with no direct correlation with the undulation of the ripples. This yields a variations of 1.57×10^{11} cm^{-2} in hole concentrations in graphene/GaAs. Likely substrate disorder induced states peaked at ~0.24 eV are again observed at some locations (spectra 1-3, 5).

These observations clearly indicate that graphene is prone to ripple formation when interfaced with Si and GaAs substrates, similar to CVD graphene transferred on hydrogen-terminated SiC substrates and exfoliated graphene on SiO$_2$ [12-14]. Interestingly, unlike the graphene/SiC junctions, the spatial variations in the Dirac point for both junctions do

not follow the topographic fluctuations. The local carrier fluctuations due to Dirac point variation nevertheless results in electron and hole puddles, similar to that of graphene/SiO_2 [13, 28]. This inherent spatial inhomogeneity in graphene lead to fluctuations in the Schottky barrier height.

6.3 Discussion

For graphene/C-face SiC, tunneling spectra give a barrier of 0.39 ± 0.04 eV, in good agreement with the calculated value of 0.45 eV, but no experimental photoemission or transport data on the C-face are available for comparison. For graphene/Si-face SiC, on the other hand, while the Schottky barrier measured in transport studies 0.91 eV [1] is close to the calculated value 0.78 eV, tunneling spectroscopy yields a smaller value of 0.35 ± 0.05 eV [Fig. 6.2(c)]. Tip-induced doping in STS measurements [29] and uncertainties in the calculation of the polarizability arising from the choice of exchange-correlation potentials (among other calculation parameters) may contribute to the difference.

While the calculated Schottky barriers are referenced to the E_{VBM}, the SiC substrates used in the experiments are n-type with the bulk Fermi level a few tenth of eV below the conduction band edge [30]. The use of E_{VBM} as the reference is consistent with the freestanding nature of the transferred graphene and the Fermi level pinning within the SiC gap near the valence band edge [31]. This is further supported by the fact that the nominal bulk n-type doping of $\sim 10^{18}$ cm^{-3} (10^{-6} Å^{-3}) is orders of magnitude smaller than polarization densities at the graphene/SiC interface [Fig. 6.3(c)], and by the existence of a narrow p-doped layer near the interface in SiC for both Si- and C-faces.

In conclusion, we observe spatial variations in the Dirac point at a graphene/semiconductor junction that cause fluctuations in the Schottky barrier height, as revealed by atomic resolution STM imaging and dI/dV tunneling spectroscopy. We further discover two types of intrinsic atomic-scale inhomogeneities that can cause fluctuations in the Schottky barrier height at graphene/semiconductor junctions: graphene ripples and/or trapped charge impurities and surface states in the semiconductor. Which mechanism dominates will depend on the nature of the semiconductor (e.g., polar vs non-polar), and/or the degree of disorder and roughness of the semiconductor surface. For polar substrates such as hexagonal SiC, fluctuations in the Dirac point are found to directly follow the topographical undulations of graphene ripples. For graphene-Si and -GaAs junctions, on the other hand, no such correlation is found, where variations in the Dirac point are likely induced by surface states and/or charge impurities due to substrate disorder. This atomic scale understanding of the fundamental properties of graphene/semiconductor Schottky contact will expedite to the development of vertical graphene devices with functionalities that are unattainable in planar device geometry [6, 7].

References

1. S. Tongay *et al.* Rectification at graphene-semiconductor interfaces: Zero-gap semiconductor based diodes. *Phys. Rev. X* **2,** 011002 (2012).

2. Y. J. Yu, Y. Zhao, S. Ryu, L. E. Brus, K. S. Kim and P. Kim. Tuning the graphene work function by electric field effect. *Nano Lett.* **9,** 3430 (2009).

3. Y. Lin *et al.* Graphene/semiconductor heterojunction solar cells with modulated antireflection and graphene work function. *Energy Environ. Sci.* **6,** 108 (2013).

4. Y. An, A. Behnam, E. Pop and A. Ural. Metal-semiconductor-metal photodetectors based on graphene/p-type silicon Schottky junction. *Appl. Phys. Lett.* **102,** 013110 (2013).

5. C. C. Chen, M. Aykol, C. C. Chang, A. F. J. Levi and S. B. Cronin. Graphene-silicon Schottky diodes. *Nano Lett.* **11,** 1863 (2011).

6. H. Yang *et al.* Graphene barrister, a triode device with a gate-controlled Schottky barrier. *Science* **336,** 1140 (2012).

7. T. Georgiou *et al.* Vertical field-effect transistor based on graphene-WS_2 heterostructures for flexible and transparent electronics. *Nat. Nanotechnol.* **8,** 100 (2013).

8. S. M. Sze. Physics of Semiconductor Devices. John Wiley & Sons, New York, (1981).

9. R. T. Tung. Formation of an electric dipole at metal-semiconductor interfaces. *Phys. Rev. B* **64,** 205310 (2001).

10. A. H. Castro Neto, F. Guinea, N. M. R. Peres, K. S. Novoselov and A. K. Geim. The electronic properties of Graphene. *Rev. Mod. Phys.* **81,** 109 (2009).

11. A. Fasolino, J. H. Los and M. I. Katsnelson. Intrinsic ripples in graphene. *Nat. Materials.* **6,** 858 (2007).

12. V. Geringer *et al.* Intrinsic and extrinsic corrugation of monolayer graphene deposited on SiO_2. *Phys. Rev. Lett.* **102,** 076102 (2009).

13. Y. Zhang, V. W. Brar, C. Girit, A. Zettl and M. F. Crommie. Origin of spatial charge inhomogeneity in graphene. *Nat. Phys.* **5,** 722 (2009).

14. A. Deshpande, W. Bao, F. Miao, C. N. Lau and B. J. LeRoy. Spatially resolved spectroscopy of monolayer graphene on SiO_2. *Phys. Rev. B* **79,** 205411 (2009).

15. W. Zhao, L. Philippe and J. Elias. Deflection of suspended graphene by a transverse electric field. *Phys. Rev. B* **81,** 155405 (2010).

16. M. T. Ong and E. J. Reed. Engineered piezoelectricity in graphene. *ACS Nano* **6,** 1387 (2012).

17. F. Guinea, M. I. Katsnelson and M. A. H. Vozmediano. Midgap states and charge inhomogeneities in corrugated graphene. *Phys. Rev. B* **77,** 075422 (2008).

18. F. Guinea, M. I. Katsnelson and A. K. Geim. Energy gaps and a zero-field quantum Hall effect in graphene by strain engineering. *Nat. Phys.* **6,** 30 (2010).

19. N. Levy *et al.* Strain-induced pseudo-magnetic fields greater than 300 Tesla in graphene nanobubbles. *Science* **329,** 544 (2010).

20. G. F. Sun, J. F. Jia, Q. K. Xue and L. Li. Atomic scale imaging and manipulation of ridges on epitaxial graphene on 6H-SiC(0001). *Nanotech.* **20,** 355701 (2009).

21. Y. Zhang *et al.* Giant phonon-induced conductance in scanning tunneling spectroscopy of gate-tunable graphene. *Nat. Phys.* **4,** 627 (2008).

22. J. H. Bardarson, M. Titov and P. W. Brouwer. Electrostatic confinement of electrons in an integrable graphene quantum dot. *Phys. Rev. Lett.* **102,** 226803 (2009).

23. S Subramaniam *et al.* Wave-function mapping of graphene quantum dots with soft confinement. *Phys. Rev. Lett.* **108,** 046801 (2012).

24. F. Speck *et al.* The quasi-free-standing nature of graphene on H-saturated SiC(0001). *Appl. Phys. Lett.* **99,** 122106 (2011).

25. J. I. Dalap, B. Doris, Q. Deng, M. C. Downer, J. K. Lowell and A. C. Diebold. Randomly oriented Angstrom‐scale microroughness at the $Si(100)/SiO_2$ interface probed by optical second harmonic generation. *Appl. Phys. Lett.* **64,** 2139 (1994).

26. H. H. Lee, R. J. Racicot and S. H. Lee. Surface passivation of GaAs. *Appl. Phys. Lett.* **54,** 724 (1989).

27. J. Balakrishnan *et al.* Giant spin Hall effect in graphene grown by chemical vapor deposition. *Nat. Comm.* **5,** 4748 (2014).

28. J. Martin *et al.* Observation of electron–hole puddles in graphene using a scanning single-electron transistor. *Nat. Phys.* **4,** 144 (2008).

29. P. Cheng *et al.* Landau quantization of topological surface states in Bi_2Se_3. *Phys. Rev. Lett.* **105,** 076801 (2010).

30. G. Prakash, M. A. Capano, M. L. Bolen, D. Zemlyanov and R. G. Reifenberger. AFM study of ridges in few-layer epitaxial graphene grown on the carbon-face of 4H-SiC(000). *Carbon* **48,** 2383 (2010).

31. A. Bostwick, T. Ohta, Th. Seyller, K. Horn and E. Rotenberg. Quasiparticle dynamics in graphene. *Nat. Phys.* **3,** 36 (2007).
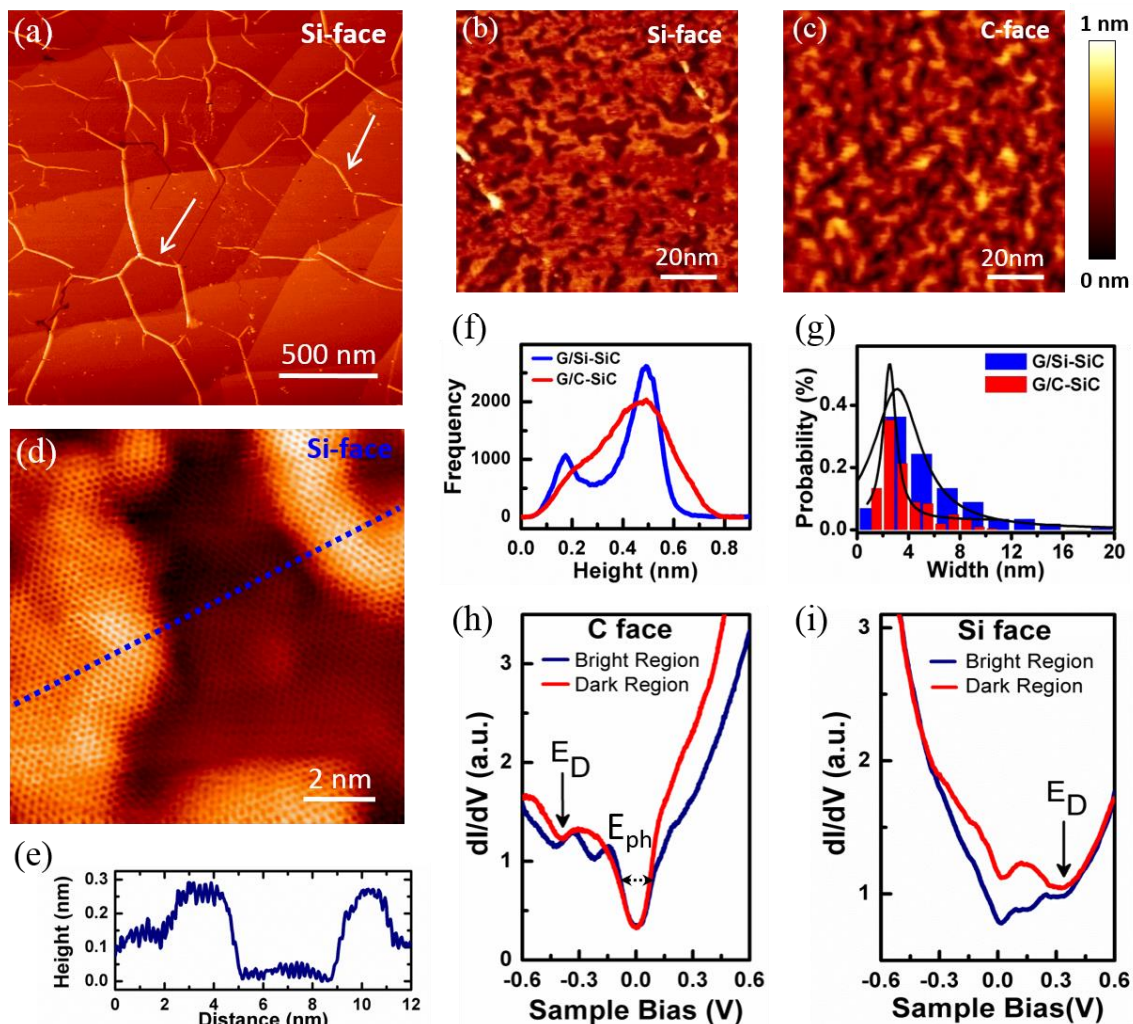
Figure 6.1: (a) Large scale STM image of graphene transferred on Si-face SiC showing graphene ridges and underneath SiC steps (I_t = 0.11 nA, V_s = -0.17 V). Morphology of graphene on (b) the Si-face (I_t = 0.1 nA, V_s = -0.05 V) and (c) the C-face SiC (I_t = 0.1 nA, V_s = -0.17 V). (d) Atomic resolution image of dark and bright regions of graphene on the Si-face (I_t = 0.4 nA, V_s = -0.02 V. (e) Line profile along the dotted blue line in (d). (f) Histograms of the measured heights of graphene ripples on both the Si- and C-faces. The average separation between the maxima and minima of the ripples is ~0.33 nm for both faces. (g) Distribution of the width of the ripples (measured by width of the dark regions) for graphene on both faces, fitted to Lorentzian line shapes (solid lines). dI/dV spectra of graphene transferred on the (h) C-SiC, and (i) Si-faces of SiC.

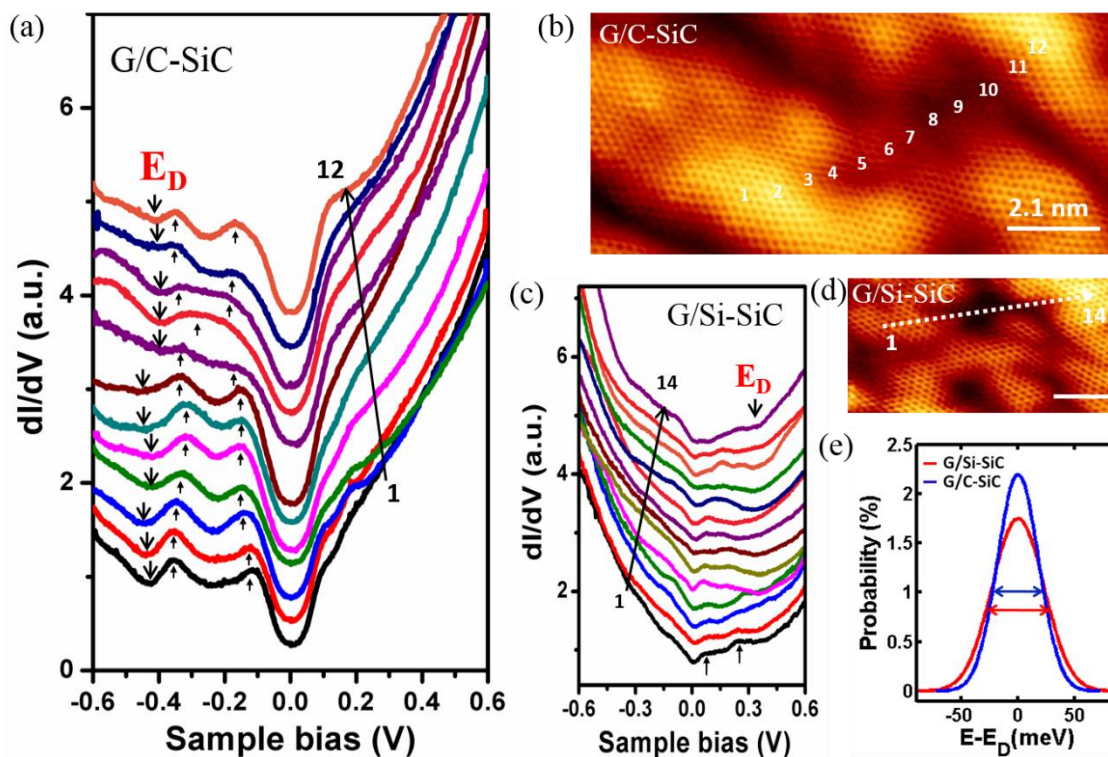**Figure 6.2:** (a) dI/dV spectra taken at the positions marked in (b), the STM image of graphene on C-face SiC (I_t = 1.6 nA, V_s = -0.4 V). (c) dI/dV spectra taken at the positions marked in (d), the STM image of graphene on the Si-face SiC (I_t = 0.6 nA, V_s = -0.2 V, 1.6 nm scale bar). (**e**) Histograms of the variation of the Dirac points for graphene on the C- and Si-faces of SiC with FWHM of 42 meV and 51 meV, respectively.
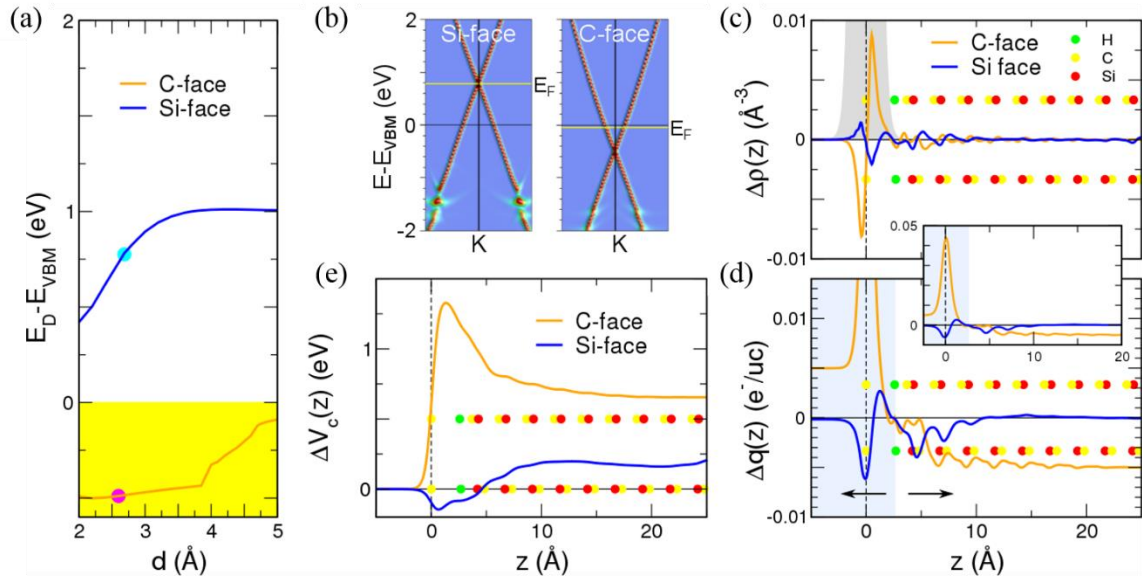
Figure 6.3: (a) Calculated positions of the Dirac point relative to the VBM as a function of the separation d between graphene and the SiC surface; the solid dots denote the calculated equilibrium positions for 6H-SiC. (b) k-projected bands around the K point of the 1×1 graphene Brillouin zone relative to E_{VBM}. The calculated Fermi levels are also indicated. (**c**) Calculated planar-averaged electron polarization density perpendicular to the surface, $\Delta\rho(z)$, defined as the difference between the self-consistent electron densities of the combined system and the superposition of the isolated SiC substrate and graphene layers at the calculated equilibrium separations of the graphene and SiC substrate. The positions of the atomic layers are given by colored dots, and the density for an isolated graphene layer is indicated by the solid gray region. (**d**) The integral of $\Delta\rho(z)$ per graphene unit cell, $\Delta q(z)$, away from the interface for both graphene and Si (with the arrows indicating the direction of integration); the solid light blue area indicates the graphene region. The inset is an expanded view of $\Delta q(z)$. (**e**) Calculated Coulomb potentials corresponding to $\Delta\rho(z)$.

Figure 6.4: (a) Large scale STM image of CVD graphene transferred onto n-Si substrate (I_t = 0.1 nA, V_s = -0.65 V). (b) Atomic resolution STM image of graphene ripples showing dark and bright regions (I_t = 0.1 nA, V_s = -0.3 V. (c) Spatially resolved dI/dV spectra taken at the locations marked in (b).
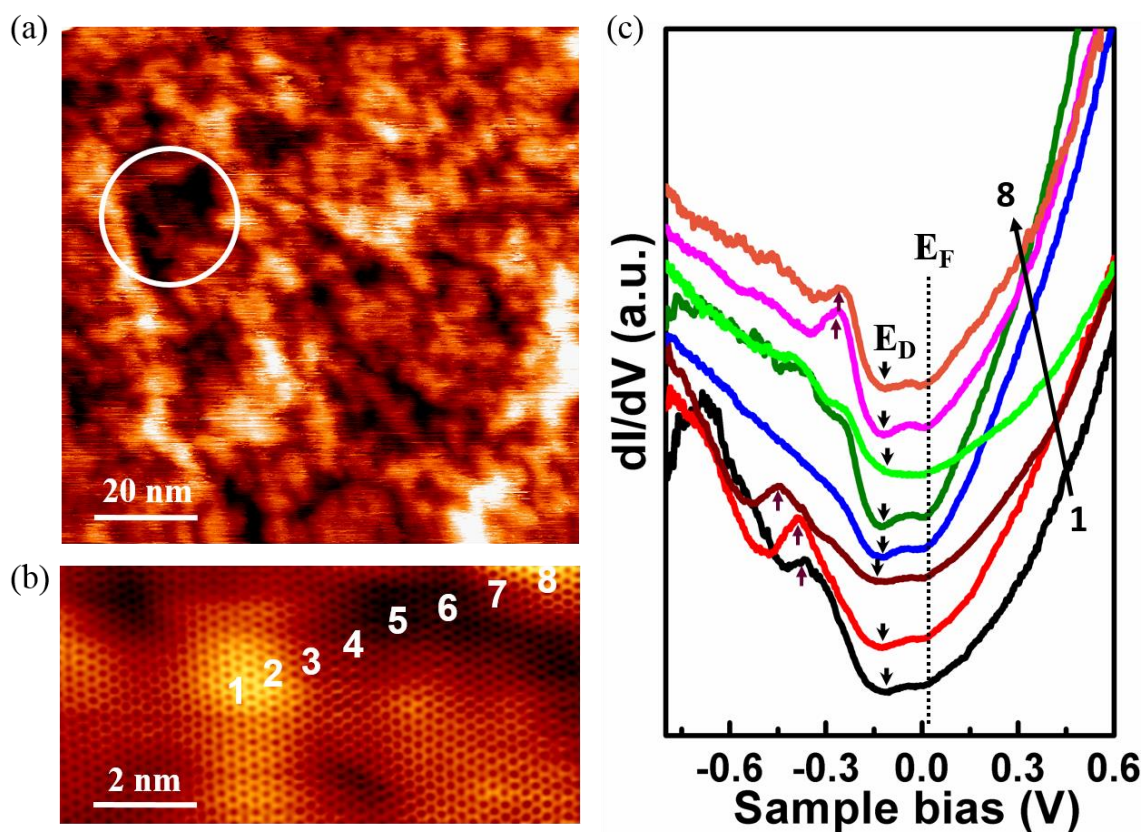
Figure 6.5: (a) Large scale STM image of CVD graphene transferred onto n-GaAs substrate (I_t = 0.1 nA, V_s = -0.3 V). (b) Atomic resolution STM image of graphene ripples showing dark and bright regions (I_t = 0.2 nA, V_s = -0.3 V. (c) Spatially resolved dI/dV spectra taken at the locations marked in (b).
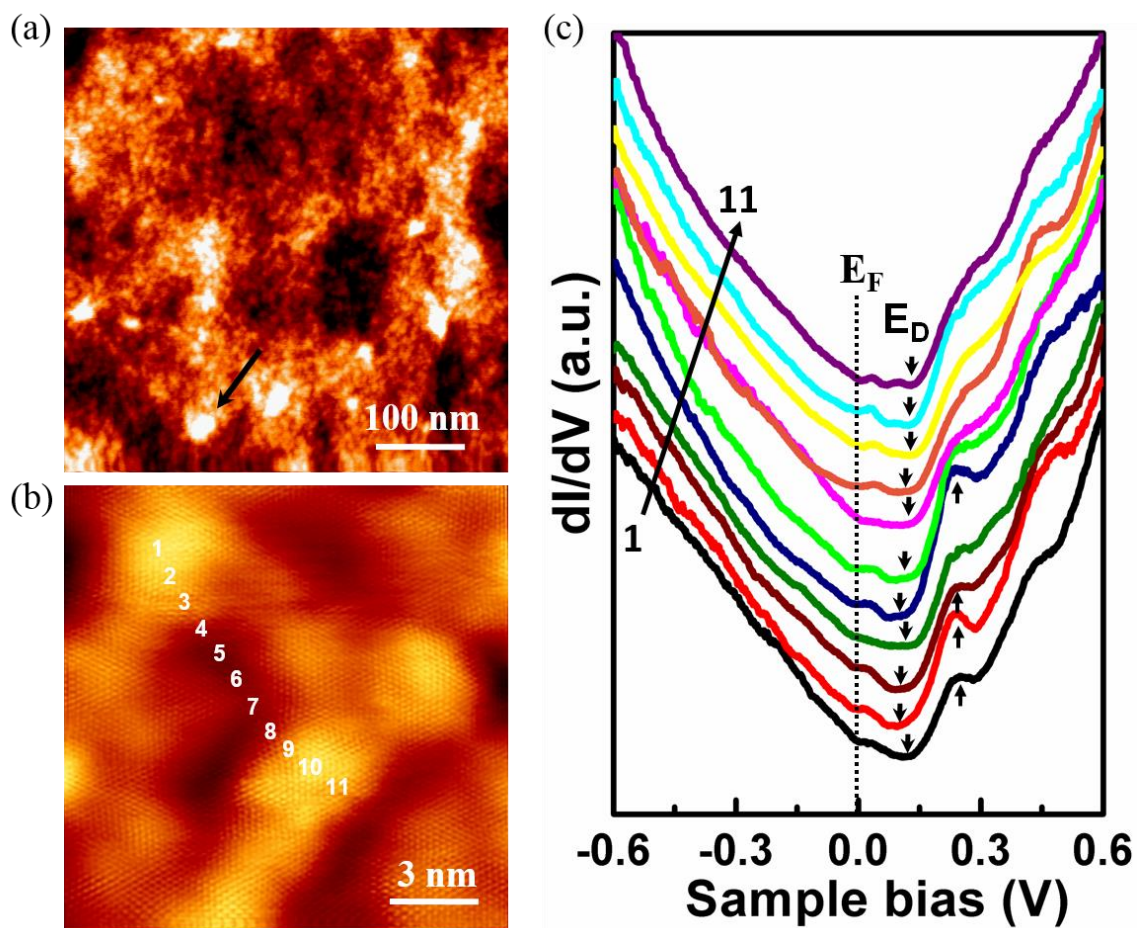
<div align="center">

Chapter 7

Proximity-Induced Giant Spin-Orbit Coupling in Graphene-Topological Insulator Van der Waals Heterostructure

</div>

7.1   Introduction

Fueled by the first experimental isolation and manipulation of graphene in 2005 [1], 2D materials have emerged at the forefront of materials research [2-3]. In their bulk form, these materials typically exhibit a characteristic anisotropic in-plane strong covalent and out-of-plane weak vdW bonding, allowing them to be stable in two dimensions in the monolayer habit. This facilitates a new avenue for "materials by design" through mechanically stacking and/or vdW epitaxy of heterostructures of highly mismatched 2D materials [2]. Coupled with our rapidly advancing expertise in handling monolayer materials, it is now possible to incorporate metallic, semiconducting, superconducting, and magnetic phases in one stack, assembled like Lego blocks with atomic precision to create materials with tailored properties and functionality beyond the limits of their bulk counterparts [3]. In particular, the inherent "thinness" of 2D materials makes their vdW heterostructures an ideal platform for capitalizing on the proximity effect, an intrinsically interfacial effect that has been predicted to arise from the overlapping of atomic orbitals across the interface [4-6].

In the case of graphene, great efforts have been devoted to enhance its intrinsically small SOC [7-10] to facilitate the experimental observation of novel phenomena such as quantum spin Hall effect - a topological state of matter with edge states populated by massless Dirac fermions [11]. With the prospect of gate tunable SOC, the observation of

these time-reversal symmetry protected edge states would offer dissipationless transport ideal for spintronics applications [12]. Earlier approaches mostly relied on chemical functionalization of graphene, including weak hydrogenation [13] and doping of heavy metal adatoms such as gold, indium, and thallium [14,15], which typically lead to disorders in graphene due to lattice deformation as a result of sp^3 hybridization and introduction of adatoms, and hence can limit carrier mobility [16]. Other methods include the intercalation of heavy metal atoms (e.g, Au/Pb) between graphene and metal substrates (e.g., Ni and Ir) [17, 18], which can be a challenge to achieve uniformly. Alternatively, recent theoretical efforts have focused on non-invasive approaches to capitalize on the proximity effect in vdW heterostructures to enhance the SOC of graphene without compromising its structural integrity [4-6]. Indeed, a SOC of up to 17 meV is observed in graphene/WS_2 vdW heterostructures, albeit arising only from tunneling of S vacancy states in WS_2 to graphene [19].

In this chapter, we synthesis graphene/topological insulator vdW heterojunctions by transferring CVD graphene onto Bi_2Se_3(0001) films grown by molecular beam epitaxy. Using STM/STS, we experimentally demonstrate a spin-orbit splitting of the graphene Dirac states up to 80 meV, which also exhibits a spatial variation of ±20 meV. These findings are consistent with our DFT calculations, which show that by proximity to Bi_2Se_3 the four-fold degeneracy of the graphene bands are lifted at the Dirac point. Moreover, due to the inherent non-epitaxial relation between graphene and Bi_2Se_3, the transferred SOC in graphene is shown to exhibit a strong spatial fluctuation both in energy and crystal momentum.

In contrast to earlier predictions [4, 6], however, our DFT calculations further reveal that for the graphene-Bi_2Se_3 vdW junction where direct hopping/bonding is expected to be weak, the transfer of the SOC is through Bi character introduced into the graphene Dirac states due to orthogonalization to the Bi_2Se_3 substrate states, leading to the formation of an approximate nodal plane near the Se layer with decaying weight on the Bi and deeper substrate planes. This admixture of Bi_2Se_3 substrate wave function character into the graphene states is responsible for the SOC splitting of the graphene bands, rather than an intrinsic enhancement of the SOC of carbon. These findings demonstrate an indirect bonding mechanism leading to the proximity effect, a viable and effective route to uniformly enable new functionalities without compromising the structural integrity of the target layer in vdW heterostructures.

7.2   Results

Calculations of spin-orbit coupling in graphene due to proximity to Bi_2Se_3. To address the possibility of large observable spin-orbit coupling in graphene – "transferred" through the interaction between the graphene π orbitals and those of $Bi_2Se_3(0001)$ – DFT calculations were done using the Full-potential Linearized Augmented Plane Wave (FLAPW) method as implemented in *flair* [20]. The $\sqrt{3} \times \sqrt{3}$ graphene overlayer on a 1×1 $Bi_2Se_3(0001)$ used in the calculations results in a compressed C-C bond length of 1.38 Å compared to the nominal 1.42 Å [Fig. 7.1(a)], which suggests that the graphene does not have a simple epitaxial relationship to the substrate. Thus, the calculations should be viewed as model calculations. Because of the different periodicities of the graphene and Bi_2Se_3 substrate, the K (and K') points of the graphene BZ fold back to around Γ of the

Bi$_2$Se$_3$ [Fig. 7.1(b)]; thus a *k*-projection technique is used to extract the dispersion of the graphene bands.

Calculations were initially done for graphene on one side of a 7 quintuple layer (QL) Bi$_2$Se$_3$(0001) film [Fig. 7.1(c)], where standard Dirac state is found on the free surface [21, 22]. When interfaced with graphene, the Dirac states are modified and shifted to the interface. To address whether the induced spin-orbit splittings require the existence of Bi$_2$Se$_3$ Dirac states, similar calculations were subsequently carried out for graphene on a single QL Bi$_2$Se$_3$ [Figs. 7.1(c)] where there is not enough bulk for the Dirac state to fully develop, i.e., the surface states are not gapless [21]. The results show that the general features of the bands for both cases resemble spinless bilayer graphene [23], i.e., one set of bands exhibit a degeneracy at the Dirac point, and another set of upward and downward dispersing bands split away from the Dirac point. The fact that the bands in the two cases are essentially the same indicates that the origin of the transferred spin-orbit coupling is the hybridization of the graphene and Bi$_2$Se$_3$ orbitals, but not with the gapless Dirac surface states as suggested in earlier calculations [4,6].

Moreover, when the SOC is set to zero (either in the calculation as a whole as in Fig. 7.1(c), or only in the Bi$_2$Se$_3$ substrate), the graphene bands exhibit the standard spin-degenerate linear dispersion, further confirming that transferred SOC is responsible for the splitting. Note that graphene Dirac point is above the Fermi level, indication of p-type doping, which is a result of the different work functions between the compressed graphene and Bi$_2$Se$_3$.

Since the intrinsic SOC of carbon is small, the origin of the large spin-orbit splitting of the graphene bands must arise from Bi$_2$Se$_3$ character – particularly the Bi states due to

their large relativistic effects – hybridized into the wave functions. Figure 7.1(d) shows the density from the (scalar relativistic) graphene states at the Dirac point for the heterojunction. In addition to the expected π state density of graphene, significant weight is seen on the Bi atoms, but essentially none on the uppermost Se atoms. Since the surface state of the 1 QL Bi_2Se_3 (and the gapless Dirac states for $Bi_2Se_3 > 5$ QL) have significant Se character and spatially overlap with the graphene π orbitals [Fig. 7.2(a)], if direct bonding is dominant, then the graphene Dirac states of the combined system would be expected to have significant weight on the Se atoms also. Thus, this lack of surface Se character in the hybridized graphene bands indicates that the simple picture of direct bonding between the helical Bi_2Se_3 surface states and the graphene Dirac states is not responsible for the calculated spin-orbit splitting [4,6]. This conclusion is also consistent with the large values calculated [c.f., Fig. 7.1 (c)], since the intrinsic SOC of Se is small compared to Bi.

Instead, for vdW heterojunctions where direct hopping/bonding is expected to be weak (as is the case here), orthogonalization requirements on the overlapping wave functions alone (i.e., no hopping) leads to gaps at band crossings and mixes in substrate wave function character into the graphene states throughout. This orthogonalization of the graphene Dirac states to the Bi_2Se_3 states is achieved by forming an approximate nodal plane near the Se layer with decaying weight on the Bi and deeper substrate planes [Fig. 7.2(b), which shows an isosurface 4x smaller than Fig. 1(d)].

Furthermore, to reflect the non-epitaxial relation between the graphene and Bi_2Se_3, an inherent trait of vdW heterostructures, we have also considered several different registries and separations for the graphene relative to the Bi_2Se_3. Figure 7.3 shows the

calculated graphene band structures for three choices of registry, where the uppermost Se atoms are in hollow or top sites of graphene, or slightly shifted. Although there are clear differences depending on the registry, the general features are similar. The magnitudes of the splittings, and the prominence of the Rashba-type features [24], exhibit a strong dependence on the height of the graphene away from the substrate, as expected due to the rapid decrease of the wave function overlap between the graphene and substrate with distance. In addition, the different registries show different splittings even for the same separations, indicating that spatial fluctuations in splittings and intensities are expected. These noticeable differences in the dispersion are in principle observable in angle-resolved photoemission. For probes that integrate for k-space, the Rashba-type splitting can lead to van Hove singularity in the density of states [25, 26], which can be directly measured by dI/dV tunneling spectroscopy as shown below.

Morphology and electronic structure of Bi_2Se_3/epitaxial graphene/SiC(0001). The 3D topological insulator Bi_2Se_3 films are grown by molecular beam epitaxy on epitaxial graphene on 6H-SiC(0001). Figure 7.4(a) shows an STM image of a 30 nm thick Bi_2Se_3 film, exhibiting growth spirals resulting from its characteristic anisotropic in-plane strong covalent and out-of-plane weak vdW bonding [27]. The Triangular spirals are characterized by atomically flat terraces separated by step heights of 0.95 nm, consistent with the thickness of one Bi_2Se_3 QL. Atomic scale imaging taken on the terrace show a closed pack structure with a periodicity of ~ 4.1 Å [inset, Fig. 7.4(b)], characteristic of the (1x1) of Bi_2Se_3 (0001). The electronic properties of the Bi_2Se_3 films were further investigated by dI/dV tunneling spectroscopy that reflects the energy resolved local DOS.

The dI/dV spectrum typically exhibits a V-shape with a minimum at ~250 meV below the Fermi level, attributed to the E_D [Fig. 7.4(b)]. The E_D position below the Fermi level indicates n-type doping of the film, likely due to Se vacancies typically present in MBE grown films, consistent with earlier studies [28].

Raman spectroscopy of graphene/Bi$_2$Se$_3$ heterostructure. CVD graphene grown on Cu foils is transferred onto the Bi$_2$Se$_3$ film immediately after removal from UHV. The transfer of graphene is first confirmed by Raman spectroscopy [Fig. 7.4(c)]. In the low frequency region, strong peaks at 128 and 171cm^{-1} corresponds to in-plane E_g^2 and out-of-plane A_{1g}^2 vibrational mode of Bi$_2$Se$_3$, respectively [27]. Three peaks characteristics of graphene, the defect induced D band, the in-plane vibrational G band, and the two phonon (2D) band appears at 1333, 1582 and 2656 cm^{-1}, respectively [29]. The FWHM of graphene 2D band (~ 38 cm^{-1}) and the intensity ratio of 2D to G peaks ($I_{2D}/I_G = 2.02$) are both consistent with single layer graphene [Fig. 7.4(c) inset]. The low intensity of D peak, $I_G/I_D = 2.26$, further indicates high quality graphene with minimal defect density.

Atomic structures of graphene-Bi$_2$Se$_3$ heterostructure. After graphene transfer and confirmation by Raman spectroscopy, samples are reintroduced back into UHV and annealed at ~ 150 $^{\circ}$C for 2 hours. Figure 7.4(d) is a large scale STM image showing the surface morphology of graphene transferred onto Bi$_2$Se$_3$. A network of graphene ridges, bulged up regions of graphene a few nm in height [30], are ubiquitous, Bi$_2$Se$_3$ spirals are still clearly visible underneath the graphene. While some of the graphene ridges originated

from CVD growth and preserved during transfer, new ones can also develop, preferentially along the Bi_2Se_3 step edges (one appointed by arrow) with height up to several nm.

On the flat terraces between ridges, graphene is found to be atomically flat without the formation of nanoscale ripples, in contrast to graphene transferred onto SiO_2/Si substrates [31-32] and hydrogen-terminated SiC [33]. Graphene honeycomb lattice is clearly resolved on flat terraces, which is also continuous across the step edges of the Bi_2Se_3, as shown in the atomic resolution STM image in Fig. 7.4(e). Moreover, Moiré patterns, often formed between two misaligned lattices, are not observed, unlike graphene-BN vdW junctions [34] and CVD graphene grown on metal substrates such as Ru(111) [35]. This may be due to the presence of disorders due to adsorbates on the Bi_2Se_3 surface after graphene transfer, which typically n-dope the surface [36, 37].

Since Bi_2Se_3 film was exposed to DI water during the graphene transfer process, control experiments were carried out to investigate the effect of water on the electronic properties of the topological insulator film. Bi_2Se_3 film was removed from UHV, dipped into deionized water for 60 sec and re-introduced back into UHV for STM and STS study. STM imaging suggests no substantial effect on surface morphology of Bi_2Se_3 [Fig. 7.5(a)]. While the line shape of the dI/dV spectra remains unchanged, the Dirac point now appears at -425 meV [Fig. 7.5(b)]. Compared to as-grown Bi_2Se_3 films, this indicates a shift of ~ 175 meV away from the Fermi level, suggesting that water exposure further electron dopes the Bi_2Se_3 film. Nevertheless, the Dirac surface states remain intact, consistent with ARPES study of adsorption of water molecules in UHV [36].

Giant spin-orbit splitting of graphene bands. The electronic properties of the graphene layer are further investigated using STS. Shown in Fig. 7.6(a) is a representative dI/dV spectrum of graphene taken at flat terraces, two high tunneling conductance regions are seen below zero bias (E_F) and above 0.33 eV, attributed to the conductance of the Bi_2Se_3 bulk valence and conduction bands, respectively. Compared to the as-grown Bi_2Se_3 spectrum [Fig. 7.4(b)], the bands are shifted up by ~ 0.3 eV. Within the gap the conductance does not reach zero, but exhibit variations that can be better seen in the close-up view in Fig. 7.6(b). Additional local maxima at 60 and 160 meV are clearly seen, separated by a minimum at 110 meV. Comparison with the calculated band structure at ~3.875 Å shows that the minimum can be attributed to the Dirac point of the graphene.

The two peaks at 60 and 160 meV can be attributed to the spin-orbit splitting of the degenerate bands of graphene. The asymmetrical line shape is a consequence of the Rashba-like splitting in momentum [c.f. Fig. 7.3], which is further confirmed by fitting with $1/\sqrt{E_{1(2)} - E}$ (dashed line), a defining characteristic of the Van Hove singularity in one-dimensional density of states, similar to those seen in the surface bands of Pb and Bi/Ag(111) systems [25]. These observations indicate the proximity of graphene to Bi_2Se_3 results in a spin-orbit coupling that splits the graphene band by ~50 meV (half of the peaks separation), an enhancement of several orders of magnitude compared to the intrinsic value of ~ μeV [12].

Spatial variation of spin orbit coupling in graphene-Bi_2Se_3 heterostructure. As discussed above, since an epitaxial relation is not expected for transferred graphene on Bi_2Se_3, spatial fluctuation of the spin orbit coupling is expected [c.f. Fig. 7.3]. This is

confirmed by spatially resolved dI/dV spectra [Fig. 7.7(a)] taken on graphene across a flat terrace of Bi_2Se_3 at positions 1-10 marked in STM image in the inset. All spectra exhibit the two local maxima due to SOC split bands, however with fluctuations of up to ~50 meV in position. While there is no significant change in the positions of peak 'b', peak 'a' shows significant spatial variation, leading to fluctuations in the magnitude of spin orbit splitting. Analysis of more than 100 spectra taken on flat graphene area at different locations exhibit a wide distribution in the Dirac energy and spin orbit splitting (up to 80 meV) [Fig. 7.7(b) & (c)], which yields a mean value of 142 and 120 meV with standard deviation of 23 and 19 meV for the Dirac energy and spin orbit splitting, respectively.

The formation of graphene ridges also provides opportunities to investigate the effect of separation between the graphene and Bi_2Se_3 on the spin-orbit splitting. Series of dI/dV spectra taken across and along the graphene ridge over a Bi_2Se_3 step edge [Fig. 7.8(a)] are shown in Fig. 7.8(b) and Figs. 7.8(c) & (d), respectively. Note that this series of spectra generally exhibits increased conductance above 0.3 eV, compared to those taken over a flat terrace [c.f., Fig. 7.7(a)]. This is likely due to an increased relative contribution from graphene due to larger separation from the substrate over these ridges. This is confirmed by spectra taken on top of a ridge where graphene is completely decoupled, which exhibit a V-shape characteristic of freestanding graphene (Fig. 7.9(d)].

Going across the graphene ridge [Fig. 7.8(b)], away from the edge on the lower terrace (spectra 1-3), two maxima at 70 and 220 meV attributed to spin-orbit splitting are seen. Approaching the step edge (spectra 4-7) where the separation between the graphene and substrate increases, the peak at 70 meV remains unchanged in position, while the peak at 220 meV shifts to lower energy, yielding increasingly smaller spin orbit coupling. Right

at the edge with maximum separation (spectra 8), the 70 meV peak diminishes in intensity, and the higher energy peak is at 180 meV, yielding a separation of only 110 meV. Moving away from the step edge on the upper terrace (spectra 9-13), the separation between the two spin-orbit splitting peaks restores gradually back to 150 meV. Note that additional peaks are also seen at higher energies (e.g., at ~0.4 eV) in this series, likely due to impurities trapped at the interface during the graphene transfer. Along the bottom of the edge where the graphene is likely to conform more closely to the Bi_2Se_3, two robust peaks are consistently observed with a spin-orbit splitting of 75 meV [Fig. 7.8(c)]. Along the top of the ridge however, a consistently suppressed 70 meV peak and a red-shifted higher energy peak is seen [Fig. 7.8(d)], similar to that of spectrum 8 in Fig. 7.8(b).

7.3   Discussion

The spin-orbit coupling transferred in graphene due to proximity to Bi_2Se_3 we measured here is up to 80 meV, several orders of magnitude greater than the intrinsic values [12]. Compared to earlier attempts that rely on chemical functionalization [13] and incorporation of impurities [38], we demonstrate that proximity effect is a promising approach to enhance the SOC in graphene without introducing scattering centers or compromising its structural integrity and/or intrinsic property such as high carrier mobility. Though the magnitude of spin-orbit splitting is comparable to those obtained by the intercalation of heavy metal atoms (e.g, Au/Pb) between graphene and metal substrates (e.g., Ni and Ir) [17,18], proximity to topological insulators or vdW materials represents a more practical route to uniformly engineer its properties.

Our findings further reveal two intrinsic characteristics – the symmetry breaking and orthogonalization requirement of the wave functions at the interface – that underlines the proximity-induced properties in vdW heterostructures. While direct bonding between the layers are not expected due to the inherent weak interlayer bonding and lack of epitaxial relation, the formation of vdW junction nevertheless breaks the symmetry of the target layer. In the case of graphene, the proximity to the Bi_2Se_3 substrate breaks both inversion and horizontal mirror (σ_h) symmetries. For free standing graphene, which has D_{6h} symmetry, the small group of the K (K') points is D_{3h} and the Dirac states belong to a doubly degenerate single group irreducible representation (irrep). With SOC, these four states (with spin) break into two 2-fold degenerate irreps of the double group, and thus a gap opens at K.

When graphene is in proximity to a substrate, the situation is different even ignoring the difference in translational symmetry of the graphene and substrate. The loss of inversion symmetry implies that the SOC bands need not be 2-fold degenerate, while the loss of the σ_h symmetry reduces the small group of K to C_{3v}. While the four states at the Dirac point still transform as the doubly degenerate Γ_3 irrep of the single group [c.f., Fig. 7.1(c)], with SOC, $\Gamma_3 \rightarrow \Gamma_4(2)+\Gamma_5(1)+\Gamma_6(1)$, where the numbers in parentheses indicate the degeneracy of the double group irreps. Thus, the SOC bands of graphene/Bi_2Se_3 around the Dirac point consist of two linearly dispersing bands (Γ_4, gapless) and two spin-orbit split states (Γ_5, Γ_6), as shown in Fig. 7.1(c). Taking into account the substrate periodicity, the remaining Γ_4 degeneracy is broken, resulting in a small gap [~15 meV in Fig. 7.1(c)], which decreases to 3 meV at 4 Å (c.f., Fig. 7.3 for the hollow registration). For other registries, gaps of 1.3 to 18 meV are found.

For the graphene/Bi_2Se_3 vdW heterostructures where direct hopping/bonding at the interface is expected to be weak, our findings indicate that the transfer of large SOC to graphene bands is realized through the hybridization of the Bi_2Se_3 character into its wave functions, and not through intrinsic spin-orbit effects in graphene due, for example, to the substrate electric field (i.e., the traditional Rashba interaction) [10, 24]. The lack of surface Se character in the hybridized graphene Dirac states, however, further indicates that the simple picture of direct bonding between the topological Bi_2Se_3 surface states and the graphene Dirac states is not responsible for the large spin-orbit splitting of the graphene bands, as suggested in earlier calculations [4, 6]. Instead, orthogonalization requirements on the overlapping wave functions [39] alone (i.e., no hopping) can mix in substrate wave function character into the graphene states, opening gaps at band crossings. As such, simply considering the modifications to the electronic bands may not be sufficient to reveal the underlying origin of proximity effects such as the spin-orbit induced splittings [4, 6].

In conclusion, we have demonstrated that the spin-orbit splittings and dispersion of the graphene bands are direct consequences of breaking symmetry and orthogonalization requirement of the wave functions at the graphene/Bi_2Se_3 vdW heterojunction. The inherent weak interlayer bonding and thus the lack of epitaxial relation between the graphene and Bi_2Se_3 layers nevertheless leads to spatial variations in the induced spin-orbit splittings. Our findings reveal that the indirect orthogonalization mechanism is at least as important as direct bonding effects, and should be generally considered to tailor properties in vdW heterostructures.

References

1. K. S. Novoselov *et al.* Electric field effect in atomically thin carbon film. *Science* **306**, 666 (2004).

2. A. H. Castro Neto and K. S. Novoselov. New directions in science and technology: Two-dimensional crystals. *Rep. Prog. Phys*. **74**, 082501 (2011).

3. A. K. Geim and I. V. Grigorieva. Van der Waals heterostructures. *Nature* **499**, 419 (2013).

4. K-H. Jin and S-H. Jhi. Proximity-induced giant spin-orbit interaction in epitaxial graphene on a topological insulator. *Phys. Rev. B* **87,** 075442 (2013).

5. L. Kou *et al.* Graphene-based topological insulator with an intrinsic bulk band gap above room temperature. *Nano Lett.* **13,** 6251 (2013).

6. J. Zhang, C. Triola and E. Rossi. Proximity effect in graphene-topological insulator heterostructures. *Phys. Rev. Lett.* **112**, 096802 (2014).

7. H. Min, J. E. Hill, N. A. Sinitsyn, B. R. Sahu, L. Kleinman and A. H. MacDonald. Intrinsic and Rashba spin-orbit interaction in graphene sheets. *Phys. Rev. B* **74,** 165310 (2006).

8. Y. Yao, F. Ye, X. L. Qi, S. C. Zhang and Z. Fang. Spin-orbit gap of graphene: First principles calculations. *Phys. Rev. B* **75,** 041401 (2007).

9. A. H. Castro Neto and F. Guinea. Impurity-induced spin-orbit coupling in graphene. *Phys. Rev. Lett*. **103**, 026804 (2009).

10. M. Gmitra, S. Konschuh, C. Ertler, C. Ambrosch-Drax and J. Fabia. Band-structure topologies of graphene: Spin-orbit coupling effects from first principles. *Phys. Rev. B* **80**, 235431 (2009).

11. C. L. Kane and E. J. Mele. Quantum spin Hall Effect in graphene. *Phys. Rev. Lett.* **95,** 26801 (2005).

12. W. Han, R. K. Kawakami, M. Gmitra and J. Fabian. Graphene spintronics. *Nat. Nanotechnol.* **9**, 794 (2014).

13. J. Balakrishnan, G. K. W. Koon, M. Jaiswal, A. H. CastroNeto and B. Ozyilmaz. Colossal enhancement of spin–orbit coupling in weakly hydrogenated graphene. *Nat. Phys.* **9,** 284 (2013).

14. D. W. Ma, Z. Y. Li and Z. Q.Yang. Strong spin-orbit splitting in graphene with adsorbed Au atoms. *Carbon* **50,** 297 (2012).

15. C. Weeks, J. Hu, J. Alicea, M. Franz and R. Wu. Engineering a robust quantum spin Hall state in graphene via adatom deposition. *Phys. Rev. X* **1,** 021001 (2011).

16. Z. H. Ni *et al.* On resonant scatterers as a factor limiting carrier mobility in graphene. *Nano Lett.* **10**, 3868 (2010).

17. D. Marchenko *et al.* Giant Rashba splitting in graphene due to hybridization with gold. *Nat. Commun.* **3,** 1232 (2012).

18. F. Calleja *et al.* Spatial variation of a giant spin–orbit effect induces electron confinement in graphene on Pb islands. *Nat. Phys.* **11**, 43 (2015).

19. A. Avsar *et al*. Spin orbit proximity effect in graphene. *Nat. Commun.* **5,** 4875 (2014).

20. M. Weinert, G. Schneider, R. Podloucky and J. Redinger. FLAPW: Applications and implementations. *J. Phys. Condens. Matter* **21**, 084201 (2009).

21. Y. Zhang *et al.* Crossover of the three-dimensional topological insulator Bi_2Se_3 to the two-dimensional limit. *Nat. Phys.* **6,** 584 (2010).

22. Y. Liu *et al.* Tuning Dirac state by strain in topological insulator Bi_2Se_3. *Nat. Phys.* **10,** 294 (2014).

23. A. H. Castro Neto, F. Guinea, N. M. R. Peres, K. S. Novoselov and A. K. Geim. The electronic properties of graphene. *Rev. Mod. Phys.* **109**, 81 (2009).

24. E. I. Rashba. Graphene with structure-induced spin-orbit coupling: Spin-polarized states, spin zero modes, and quantum Hall effect. *Phys. Rev. B* **79**, 161409R (2009).

25. C. R. Ast *et al*. Local detection of spin-orbit splitting by scanning tunneling spectroscopy. *Phys. Rev. B* **75**, 201401 (R) (2007).

26. H. Hirayama, Y. Aoki and C. Kato. Quantum interference of Rashba-type spin-split surface state electrons. *Phys. Rev. Lett.* **107**, 027204 (2011).

27. Y. Liu, M. Weinert and L. Li. Spiral growth without dislocations: Molecular beam epitaxy of topological insulator Bi_2Se_3 film on epitaxial graphene/SiC(0001). *Phys. Rev. Lett.* **108,** 115501 (2012).

28. P. Cheng *et al.* Landau quantization of topological surface states in Bi_2Se_3. *Phys. Rev. Lett.* **105,** 076801 (2010).

29. A. C. Ferrari *et al.* Raman spectrum of graphene and graphene layers. *Phys. Rev. Lett.* **97,** 187401 (2006).

30. G. F. Sun, J. F. Jia, Q. K. Xue and L. Li. Atomic scale imaging and manipulation of ridges on epitaxial graphene on 6H-SiC(0001). *Nanotechnol.* **20,** 355701 (2009).

31. V. Geringer *et al.* Intrinsic and extrinsic corrugation of monolayer graphene deposited on SiO_2. *Phys. Rev. Lett.* **102,** 076102 (2009).

32. Y. Zhang, V. W. C. Brar, C. Girit, A. Zettl and M. F. Crommie. Origin of spatial charge inhomogeneity in graphene. *Nat. Phys.* **5**, 722 (2009).

33. S. Rajput, M. Chen, Y. Liu, Y. Y. Li, M. Weinert and L. Li. Spatial fluctuations in barrier height at the graphene-silicon carbide Schottky junction. *Nat. Comm.* **4,** 2752 (2013).

34. C. R. Wood *et al.* Commensurate–incommensurate transition in graphene on hexagonal boron nitride. *Nat. Phys*. **10**, 451 (2014).

35. D. Stradi *et al.* Electron localization in epitaxial graphene on Ru(0001) determined by moiré corrugation. *Phys. Rev. B* **85**, 121404(R) (2002).

36. H. M. Benia, C. Lin, K. Kern and C. R. Ast. Reactive chemical doping of Bi_2Se_3 topological insulator. *Phys. Rev. Lett.* **107,** 177602 (2011).

37. C. Y. Chen *et al.* Robustness of topological order and formation of quantum well states in topological insulators exposed to ambient environment. *Proc. Natl. Acad. Sci.* **109**, 3694 (2012).

38. J. Balakrishnan *et al.* Giant spin Hall effect in graphene grown by chemical vapor deposition. *Nat. Commun.* **5,** 4748 (2014).

39. W. A. Harrison. Electronic structure and the properties of solids. p536-538, Dover Publications, Inc. New York, 1989.
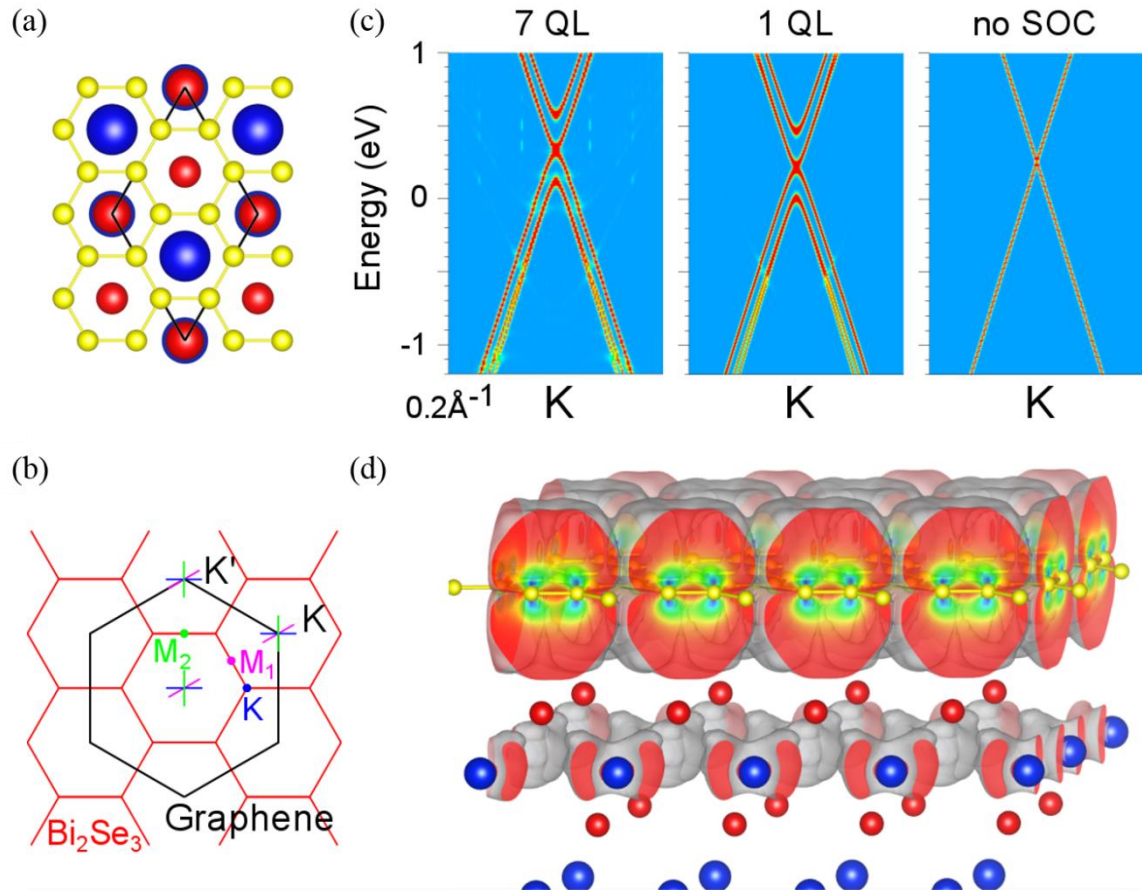
Figure 7.1: (a) Ball-and-stick model of graphene on the Bi_2Se_3(0001) surface with a $\sqrt{3} \times \sqrt{3}$ epitaxial relationship. Yellow ball: carbon; blue ball: Bi; red ball: Se. (b) Brillouin zones for Bi_2Se_3 and graphene, with the high symmetry points for each marked. The graphene K and K' points fold back to the Γ point of the Bi_2Se_3 BZ. The colored lines show different cuts along high symmetry directions around Γ and the K, K'. (c) The *k*-projected bands for graphene on 1 and 7 QLs of Bi_2Se_3, and for the 7 QLs without SOC. (The surface of the 7 QL system exhibits the standard topological insulator Dirac surface state [28].) (d) Density corresponding to the graphene Dirac point states for the graphene/Bi_2Se_3 junction, showing that graphene π orbitals also have weight on the Bi atoms, which accounts for the large transferred spin-orbit interaction. (Isosurface: 10^{-4} e^-/a_B^3; maximum of the R-G-B color is 0.125 e^-/a_B^3.)
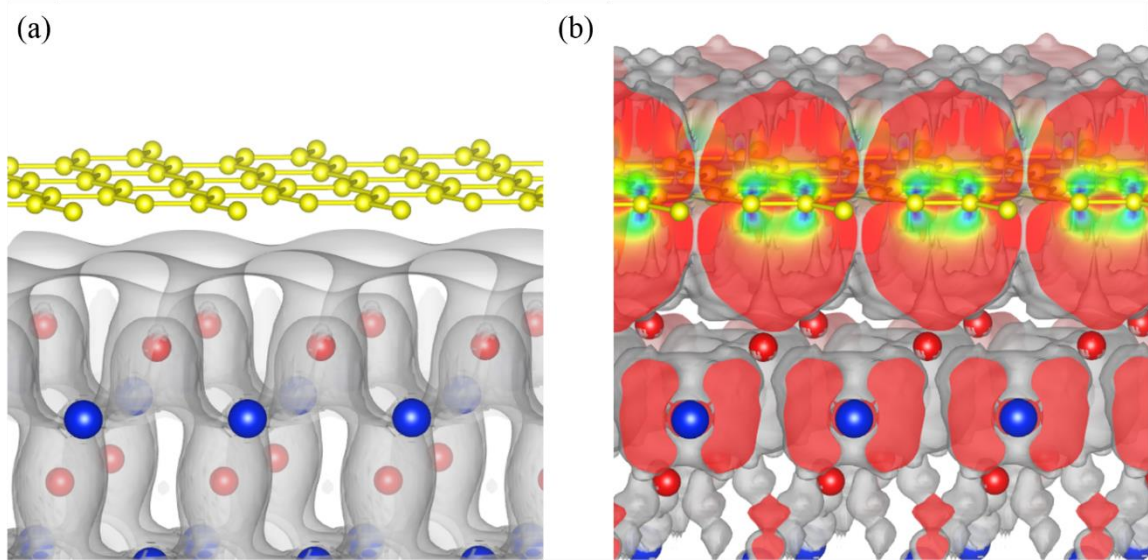
Figure 7.2: (a) Isosurface (5×10^{-5} $e^-/a_B{}^3$) of the 1 QL Bi_2Se_3 surface state that evolves from the conduction band into the topological insulator Dirac state. Note that this state is mainly on the Se atoms. Yellow ball: carbon; blue ball: Bi; red ball: Se. (b) Density corresponding to the graphene Dirac point states for the graphene/Bi_2Se_3 junction, showing that graphene π orbitals also have weight on the Bi atoms, which accounts for the large transferred spin-orbit splitting. (Isosurface: 2.5×10^{-5} $e^-/a_B{}^3$; maximum of the R-G-B color is 0.125 $e^-/a_B{}^3$.)
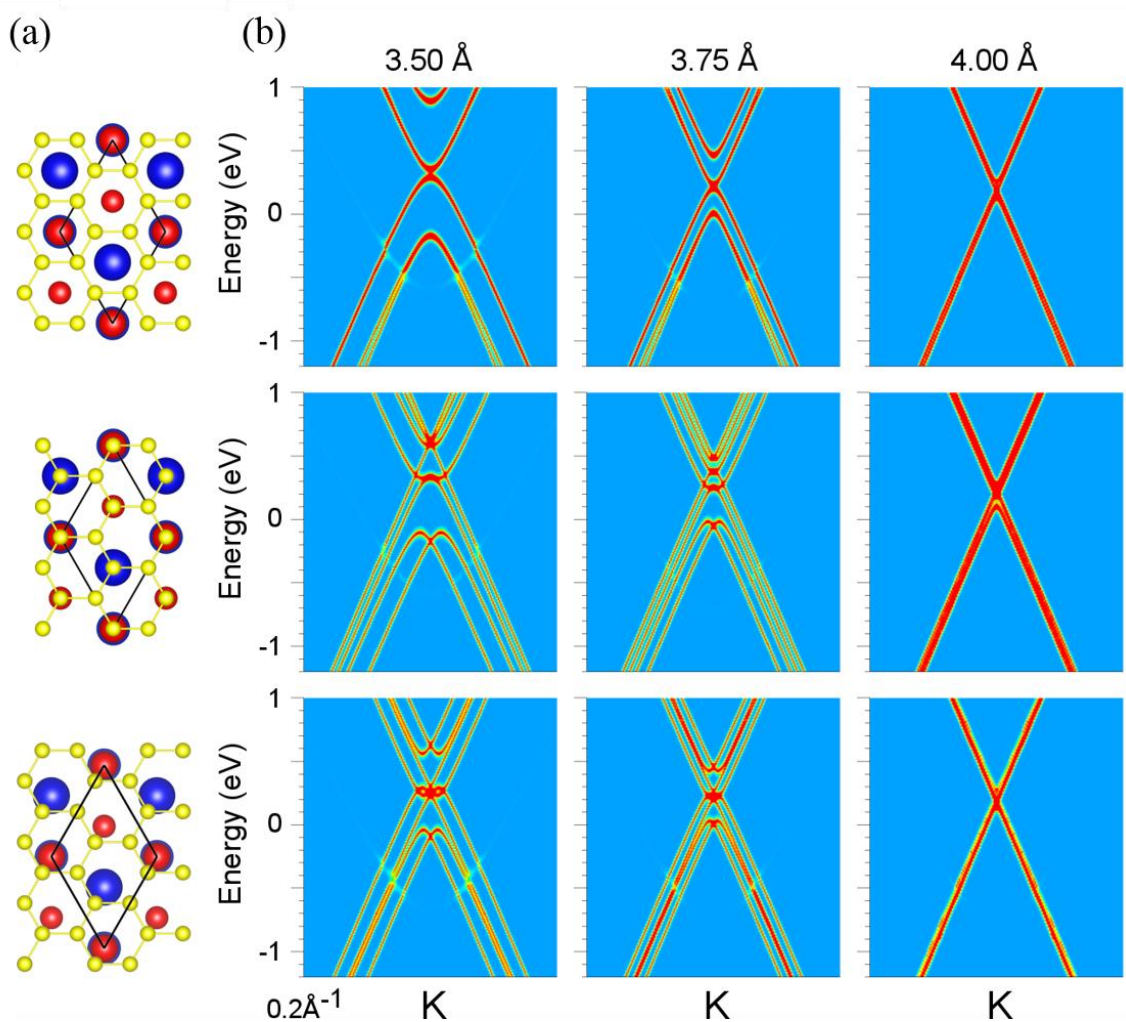
Figure 7.3: (a) Structural models of three different registries (yellow ball: carbon; blue ball: Bi; red ball: Se), and (b) the corresponding bands (K+K') along the "Γ-K" line for various graphene-Bi_2Se_3 separations.
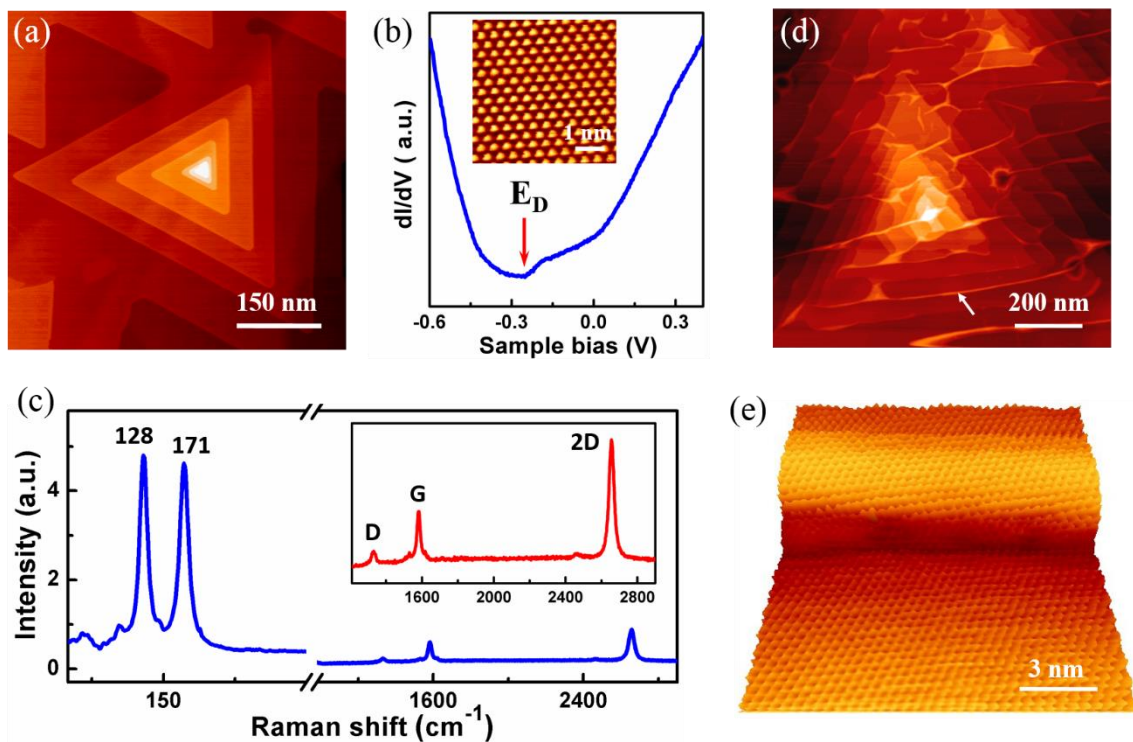
Figure 7.4: (a) Large scale STM image of Bi_2Se_3 film showing spiral growth ($I_t = 0.1$ nA, $V_s = -0.81$ V). (b) dI/dV spectra of as grown Bi_2Se_3 film with Dirac point marked. Inset: Atomic resolution image of Bi_2Se_3 film ($I_t = 0.15$ nA, $V_s = -0.6$ V). (c) The Raman spectrum of graphene- Bi_2Se_3. Inset: close up view of three characteristics peaks of graphene. (d) Large scale STM image of graphene transferred on Bi_2Se_3 ($I_t = 0.1$ nA, $V_s = -1.89$ V). (e) Atomic resolution image of graphene is continuous over the step edge ($I_t = 0.5$ nA, $V_s = -0.1$ V).

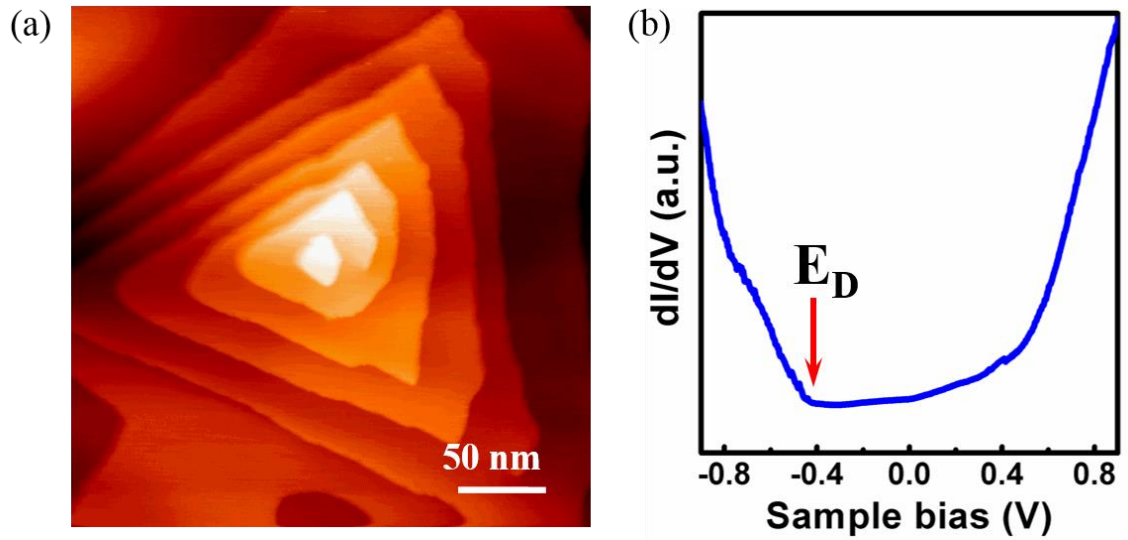**Figure 7.5:** (a) STM image of a 30 nm MBE-grown Bi_2Se_3 film after dipping in water for one minute (I_t = 0.1 nA, V_s = 1.02 V). (b) dI/dV spectrum taken on the water-exposed Bi_2Se_3 film, showing the shift of E_D away from the Fermi level.
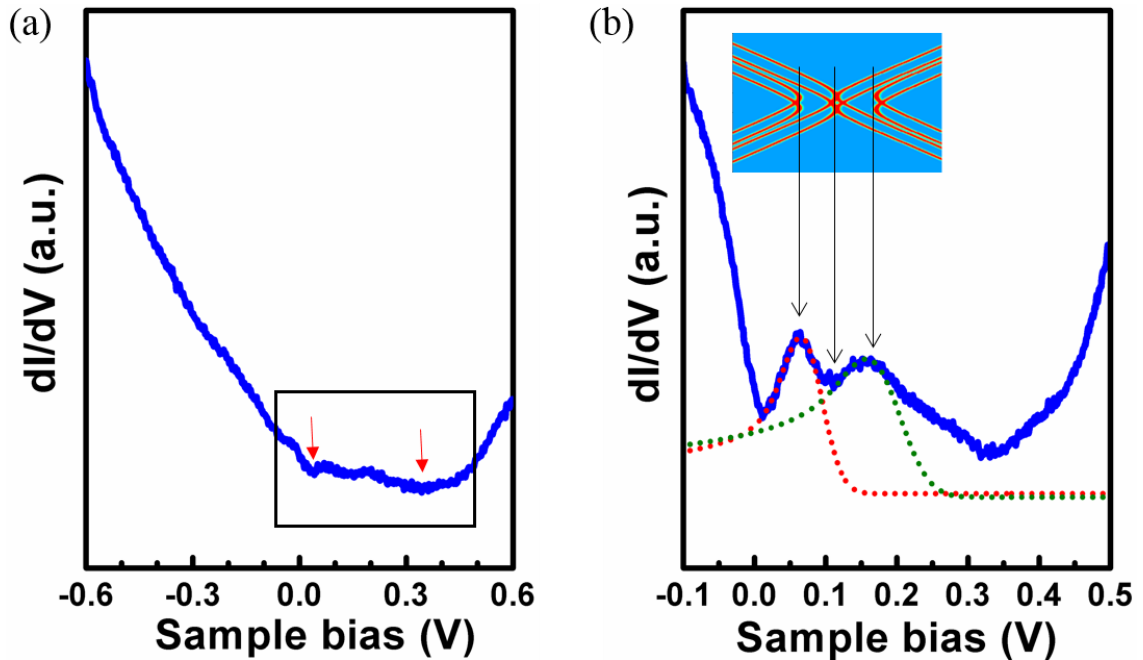
Figure 7.6: (a) dI/dV spectra taken on graphene on graphene/Bi_2Se_3 heterostructure. (b) Close-up view of the boxed region in (a), dashed lines are $1/\sqrt{E_{1(2)} - E}$ fits to the two spin orbit peaks convoluted with Gaussian broadening: $f(x) = \frac{1}{\sigma\sqrt{2\pi}} exp\left(-\frac{1}{2}\left(\frac{x-\mu}{\sigma}\right)^2\right)$, with μ=0, σ=25 and 35 meV for the first and second peak, respectively. Both peaks follow a $1/\sqrt{E}$ behavior, characteristic of the Van Hove singularity in 1D parabolic dispersion. The observation of this singularity is reminiscent of the distinct feature of a spin-split band in a two-dimensional electron gas. Inset: calculated spin-orbit split bands of graphene/Bi_2Se_3 at 3.875 Å and offset registry for comparison [c.f., Fig. 7.3].
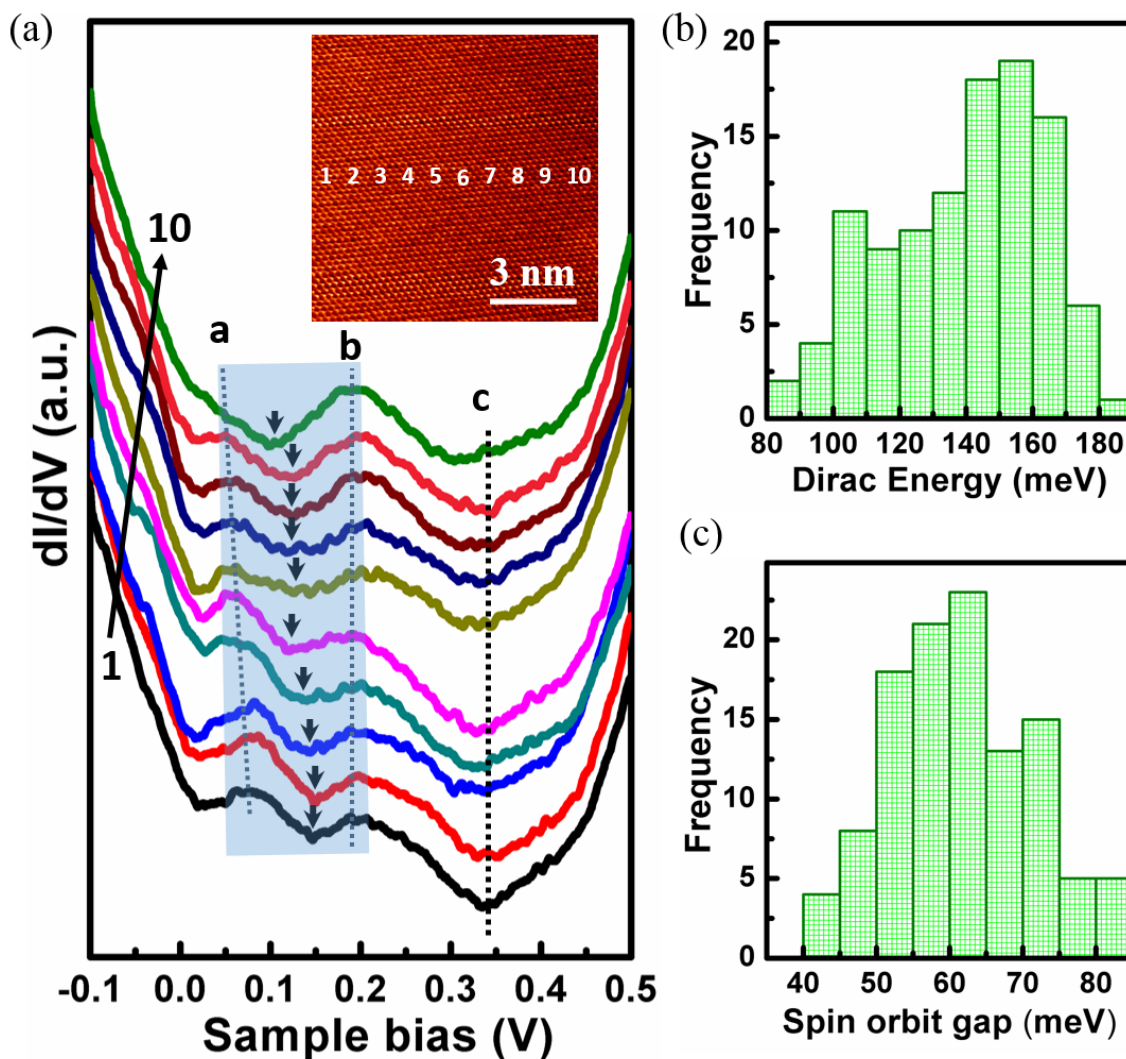
Figure 7.7: (a) Spatially resolved dI/dV spectra taken on a flat terrace at positions 1-10 marked in the STM images in the inset (I_t = 0.1 nA, V_s = -0.4 V). Histogram of distribution of (b) the Dirac point position and (**c**) spin orbit splitting.

Figure 7.8: (a) STM image of a Bi$_2$Se$_3$ step edge underneath graphene (I$_t$ = 1.1 nA, V$_s$ = -0.02 V, 3 nm scale bar). dI/dV spectra taken (b) across, (c) along bottom and (d) top of the ridge at positions marked in (a).
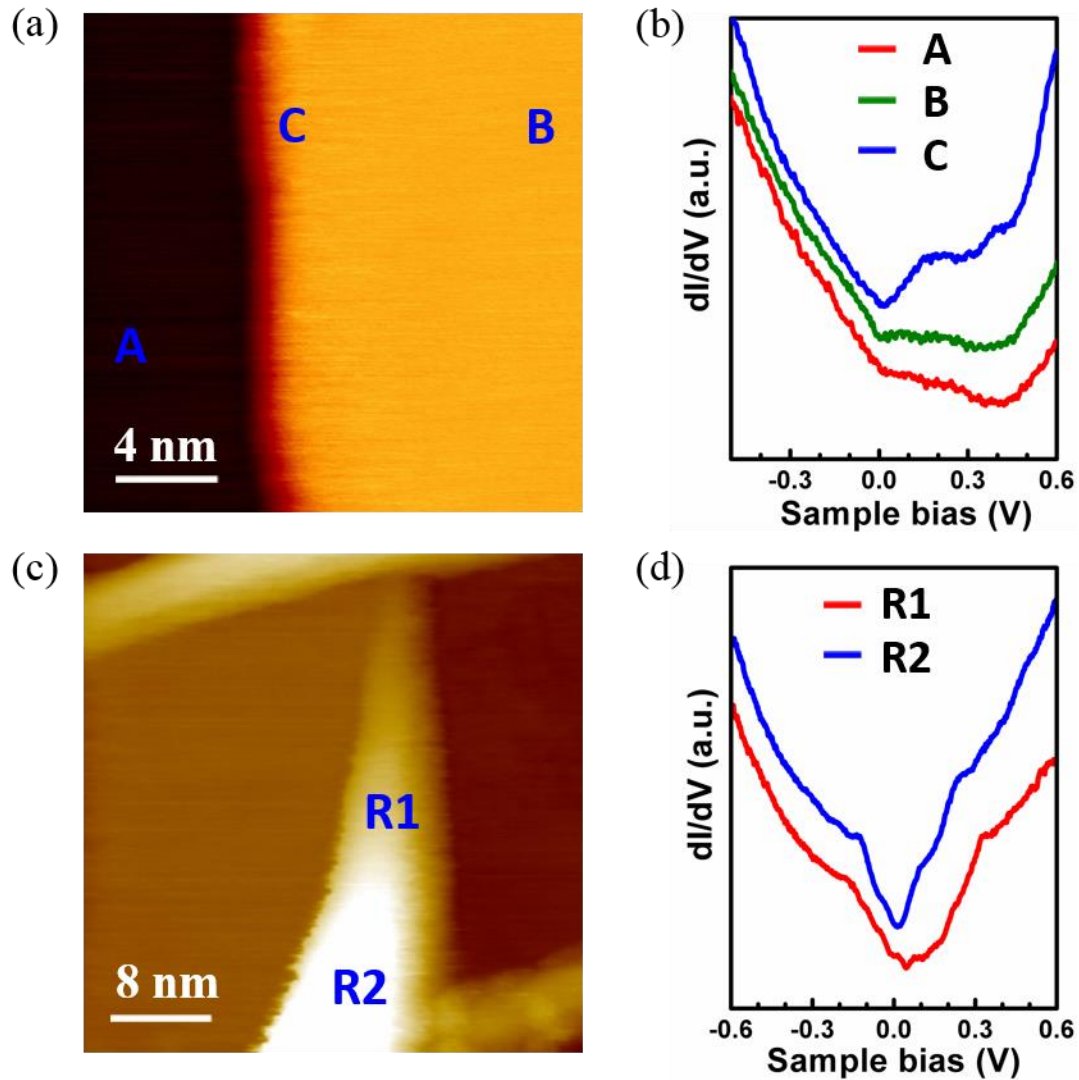
Figure 7.9: (a) STM image of the transferred graphene across a Bi_2Se_3 step edge ~ 1 nm in height (I_t = 0.1 nA, V_s = -0.4 V, 4 nm scale bar). (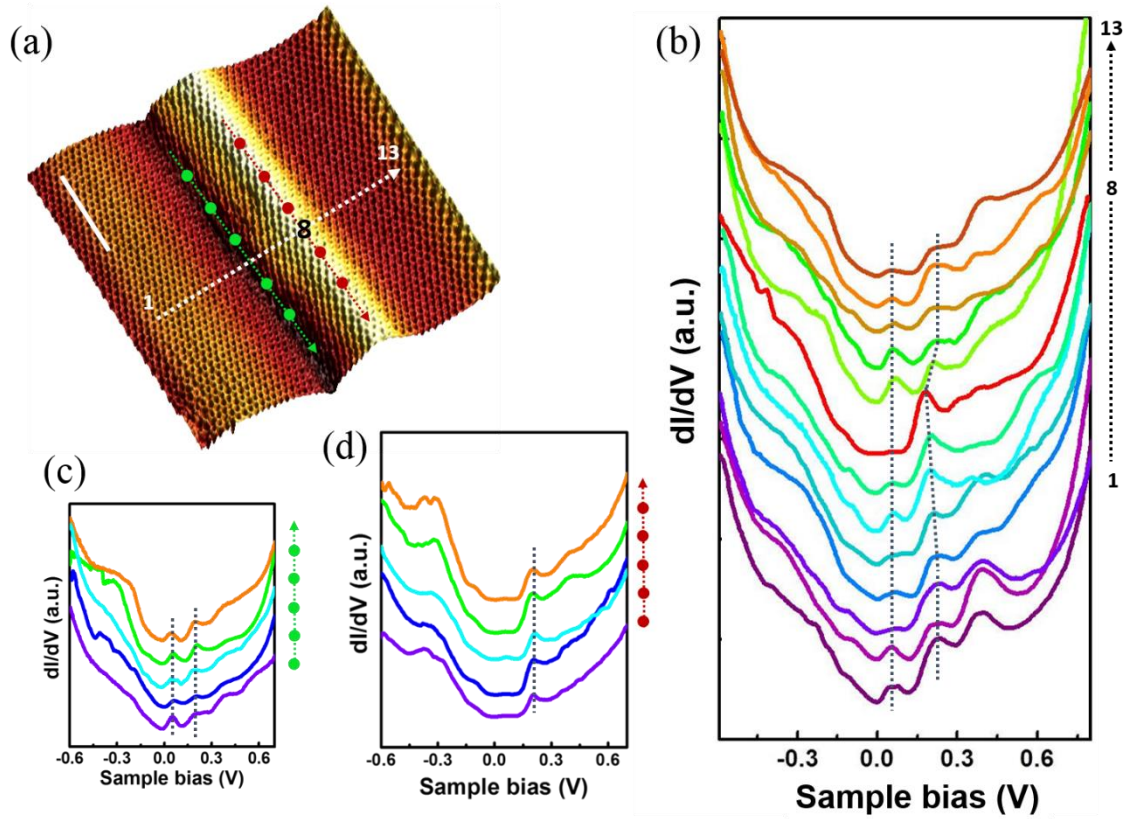b) dI/dV spectra taken on lower and upper flat terrace (spectrum A and B), and in close proximity to the step edge (spectrum C). Spectrum C has higher DOS above Fermi level compared to spectrum A and B with two peaks at 0.16 and 0.39 eV respectively. (c) STM image of a ridge with variable height of few nm, where graphene is completely decoupled from Bi_2Se_3 (I_t = 0.1 nA, V_s = -0.4 V). (d) dI/dV spectrum taken at position marked in (c), showing a characteristic V-shape expected for freestanding graphene.

Chapter 8
Summary and Outlook

8.1   Summary

This dissertation research demonstrates that interface engineering is a viable route to control and further enhance the electronic properties of graphene.

By transferring CVD graphene onto surfaces of opposite polarization - H-terminated Si-face and C-faces of hexagonal SiC, we show that charge carrier type in graphene can be controlled by substrate polarization. Furthermore, we find that charge carrier type in epitaxial graphene/SiC(0001) convert from n- to p-type upon H-intercalation at the interface. Additionally, we observe the formation of ripples in the graphene H-terminated SiC heterojunctions, which causes local fluctuations in the Dirac point. This is due to the formation of a Schottky dipole at the graphene/SiC interface, thus the Dirac point depends strongly on the spacing between graphene and SiC. As a result, ripples, i.e., topographic fluctuations of graphene with respect to the substrate leads to the variations in the Dirac point, which is in direct contrast to the case of exfoliated graphene transferred onto a SiO_2 substrate.

When graphene is interfaced with a semiconductor, Schottky barrier forms at the junction. We observe spatial variations in the Dirac point at a graphene/semiconductor junctions that cause fluctuations in the Schottky barrier height. We discover two types of intrinsic atomic-scale inhomogeneities that can cause fluctuations in the Schottky barrier height at graphene/semiconductor junctions: graphene ripples and/or trapped charge impurities and surface states in the semiconductor. For polar substrates such as hexagonal

SiC, fluctuations in the Dirac point are found to directly follow the topographical undulations of graphene ripples. For graphene-Si and -GaAs junctions, on the other hand, no such correlation is found. Instead, variations in the Dirac point are likely induced by surface states and/or charge impurities of the semiconductors.

By transferring CVD graphene onto MBE grown topological insulator Bi_2Se_3, we demonstrate the proximity-induced SOC up to 80 meV in graphene, an enhancement of several orders of magnitude compared to the intrinsic value of ~ μeV. Moreover, the SOC exhibits spatial variations of ±20 meV, as a result of inherent weak interlayer vdW bonding and thus the lack of epitaxial relation between the graphene and Bi_2Se_3 layers. DFT calculations reveal that the transfer of the SOC is through Bi character introduced into the graphene Dirac states due to orthogonalization to the Bi_2Se_3 substrate states, leading to the formation of an approximate nodal plane near the Se layer with decaying weight on the Bi and deeper substrate planes. This admixture of Bi_2Se_3 substrate wave function character into the graphene states is responsible for the SOC splitting of the graphene bands, rather than an intrinsic enhancement of the SOC of carbon. These findings demonstrate that indirect bonding mechanism leading to the proximity effect is a viable route to induce desirable properties in vdW heterostructures without comprising their structural integrity.

8.2 Outlook

Graphene-ferroelectric heterojunctions: Our demonstration of polarization doping in graphene-SiC junction suggests that the integration of graphene with ferroelectric materials, which exhibits bipolarity and remnant polarization, can create new opportunities for multifunctional devices. For example, graphene can be transferred onto lead zirconate

titanate (PZT) substrate, where the type and concentrations of charge carriers in graphene will be continuously tuned by an external electric field. Demonstration of such tunability would facilitate the fabrication of atomically sharp nano scale p-n junctions in graphene/PZT heterostructure by applying gate voltage using a local scanning probe. Carrier transport across such a graphene p-n junction is similar to the refraction of electromagnetic waves at an interface where the refractive index changes sign, known as the Veselago lens [1-2]. Such switch mechanism would allow graphene transistors operating in the quantum coherent regime [3], extending the promise of graphene electronics far beyond conventional field effect transistors.

Quantum spin Hall effect in graphene/topological insulator: Our demonstration of the proximity-induced 80 meV spin orbit coupling in graphene-Bi_2Se_3 graphene makes it possible the observation of the quantum spin Hall effect at room temperature. The spin-orbit induced gap would make graphene a quantum spin Hall insulator with only the gapless edge states conduction [4]. The observation of such effect requires the fabrication of graphene nanoribbons that are integrated with Bi_2Se_3 films, which can be implemented by two possible routes. First, graphene nanoribbons can be produced by unzipping carbon nano tubes [5], then transferred onto the MBE grown Bi_2Se_3 films. The second approach involves STM tip assisted lithography, which is capable of fabricating graphene nanoribbons just a few nm in width [6-7]. Here, CVD graphene will be transferred onto the MBE grown Bi_2Se_3 first, then the STM tip will scanned predetermined patterns in reactive environments such as H_2, O_2, or H_2O in ultrahigh vacuum. The large electronic field near the tip-graphene tunneling gap would facilitate the dissociation of H_2, O_2 and H_2O molecules so that etching reactions, such as

$$4H + 2C \rightarrow C_2H_4 \ (\uparrow)$$
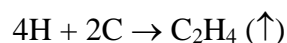
would lead to the removal of carbon atoms from graphene [8], leaving in its track trenches and ribbons with H-termination. After the graphene nanoribbons are fabricated, spatially resolved tunneling dI/dV spectroscopy can be carried out to provide the most direct proof of such gapless edge states.

References

1. J. B. Pendry. Negative refraction makes a perfect lens. *Phys. Rev. Lett.* **85**, 3966 (2000).

2. J. B. Pendry. Negative refraction for electrons. *Science* **315**, 1226 (2007).

3. V. V. Cheianov, V. Falko and B. L. Altshuler. The focusing of electron flow and a Veselago lens in graphene p-n junctions. *Science* **315**, 1252 (2007).

4. C. L. Kane and E. J. Mele. Quantum spin Hall Effect in graphene. *Phys. Rev. Lett.* **95,** 26801 (2005).

5. L. Jiao, L. Zhang, X. Wang, G. Diankov and H. Dai. Narrow graphene nanoribbons from carbon nanotubes. *Nature* **458,** 877 (2009).

6. L. Apaszto, G. Dobrik, P. Lambin and L. P. Biro. Tailoring the atomic structure of graphene nanoribbons by scanning tunneling microscopy lithography. *Nat. Nanotechnol.* **3,** 397 (2008).

7. G. Z. Magda *et al.* Room-temperature magnetic order on zigzag edges of narrow graphene nanoribbons. *Nature* **514**, 608 (2014).

8. Y. Y. Li, M. X. Chen, M. Weinert and L. Li. Direct experimental determination of onset of electron–electron interactions in gap opening of zigzag graphene nanoribbons. *Nat. Comm.* **5,** 4311 (2014).

Appendix A
STM Instrumentation

Despite the extreme simple working principle, technical implementation of STM requires knowledge of several different disciplines. This section discusses the essential elements of STM.
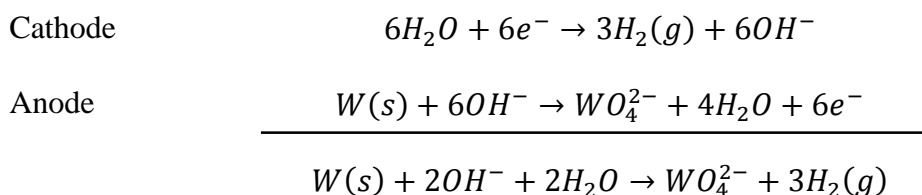
I. Tip preparation and treatment

The resolution of an STM largely depends on shape of the tip and on its chemical composition, e.g. atomic resolution is usually achieved with a very sharp tip having a single atom at the apex. Therefore reproducible preparation of STM tips is an important skill. While STM tips are commercially available, they are not used in our research. Because of long exposure to ambient environments, metal oxide layers typically formed on the tip may act as an additional tunneling barrier between the tip and the sample and reduce the STM resolution. To avoid this situation, it is recommended that a freshly prepared tip must be loaded directly into the UHV system.

The STM tips generally fall into two categories: mechanically formed and electrochemically etched. The former one can be prepared by simply cutting a metal wire with scissor at an angle $\sim 60^0$. Platinum iridium (Pt-Ir) wire (0.25mm diameter) is commonly used because Pt is relatively inert to oxidation and small percentage of Ir makes the tip harder. Although these tips are bulky with an overall radius of $\sim$ 1um, the rough grinding process often creates a number of sharp minitips at the end that act like fingers of a hand extending towards the surface. Because of the strong exponential dependence of the

tunneling current on the separation, only the minitip closest to the sample surface contributes to the tunneling current.

Electrochemical etching of tungsten wire is the most popular method to prepare a sharp STM tip with a radius of apex curvature in the order of 20 to 50nm [1, 2]. Tungsten has been a materiel of choice because it is hard, mechanically stable and also suitable for use at low temperatures. A basic setup of the etching process is shown in Fig. A1(a). A polycrystalline tungsten wire, typically 0.5mm in diameter, is mounted on a micrometer and vertically inserted in aqueous solution of KOH. The height of the wire relative to the surface of the solution can be adjusted. A ring-shaped stainless steel wire is placed concentrically around the tungsten wire. When a voltage is applied between the two electrodes (the tungsten wire anode and the stainless steel ring cathode), etching occurs at the interface of the air and the KOH solution as demonstrated by the following reactions [3]

Cathode $$6H_2O + 6e^- \rightarrow 3H_2(g) + 6OH^-$$

Anode $$W(s) + 6OH^- \rightarrow WO_4^{2-} + 4H_2O + 6e^-$$

$$W(s) + 2OH^- + 2H_2O \rightarrow WO_4^{2-} + 3H_2(g)$$

Water molecules reduce to hydrogen gas at the cathode, while solid tungsten wire oxidizes to tungstate anions (WO_4^{2-}), soluble in water, at the anode. The dissolution of tungsten causes the formation of a neck on the wire at the air-KOH interface. As the reaction proceeds, the neck becomes thinner and thinner until the weight of the lower half of wire fractures the neck, and lower part drops off in the solution. The dropped piece also has a tip, which may be better than the upper one. After removing the tip from the solution, a

through rinsing with DI water and alcohol is required to remove KOH residues from the tip surface.

The aspect ratio and overall shape of an electrochemically etched tip depends on several parameters: the etching rate, the shape of the meniscus, the concentration of the KOH solution and the initial immersion length of the wire in the solution [2]. A too fast etching rate often produces irregular shaped tips, while a too long process results in a rather long and thin tips. Long and thin tips are unstable against mechanical vibrations, and are thus less favorable than a short tip which taper rapidly towards the apex. The most important parameter that determines the final shape of tip end is cutoff time of the etching current after the lower part drops off. To get a sharp tip end, the applied voltage between the electrodes should be shut off immediately after the drop-off.

As-prepared etched tungsten tips have an oxide layer of ~ 20nm on the surface. Dipping the tip in a hydrogen fluoride (HF) solution prior to loading in an UHV chamber is helpful in removing oxides. To remove the remaining oxides and other contaminations, the tip must be annealed in UHV above 800 ℃ without causing any blunting. Popular annealing methods of the tip include electron bombardment and resistive heating by a tungsten filament [4, 5]. In-situ methods such as applying high voltage pulses to the tip or large bias voltages during scanning are also very effective for cleaning and sharpening the tip [6]. These methods result in the self-reconstruction of the tip at the apex. Another common method involves controlled collision of tip with a clean surface in which few surface atoms attach to the tip apex and form a nano-tip. These methods have been used since the birth of the STM.

Tip treatment for spectroscopy

As prepared tips often show unpredictable and non-reproducible tunneling spectra, thus tip calibration is crucial to obtain reliable STS data. In imaging mode, a sharp tip is required to achieve atomic resolution while in spectroscopy mode a tip with flat DOS is desirable. The tip that provides atomic resolution often has highly structured DOS which complicates the interpretation of the dI/dV spectra. An ideal tip for STS measurements must have DOS with free-electron metal behavior, which can be obtained by the following in-situ methods:

Annealing of the tip: A field emission current can be used to locally heat up the end of the tip [7]. A sharp tip generates field emission current when a large positive bias voltage is applied to the sample. When emission current is very high, the tip end melts and recrystallizes to form facets with low surface energy. In case of a tungsten tip, W(110) facets are preferred having surface DOS similar to free electron metals [3].

Controlled crashing of the tip on a metal surface: In this process, the STM tip is brought in physical contact with a clean and flat metal surface for a fraction of second. After a couple of controlled collisions, the tip apex is most likely coated with metal atoms. A successful tip treatment results in a flat tunneling spectrum on the metal surfaces. Silver (Ag) and gold (Au) surfaces are commonly used in this method because they are nearly free electron metals near the Fermi level [8, 9].

In this work, we calibrated the tips by controlled collision and carrying out dI/dV measurements on Ag(111) films grown on 6H-SiC(0001) [10]. Figure A1(b) shows a typical tunneling spectra taken on the Ag film, which shows a step like feature in the tunneling conductance near zero sample bias. This behavior is consistent with the low edge

of the energy band of the Ag(111) surface [8], and ensures that tip is free of spectroscopic anomalies.

II. Piezoelectric scanner

Piezoelectric scanner is the heart of an STM. It moves the probe tip across the sample and controls the tip height above the surface. The inverse piezoelectric effect, application of electric field leads to a deformation in the piezoelectric material, is used to control the tip position to sub-Angstrom accuracy. The tip movement in the x, y directions and in the z direction should be independent for a good scanner, and amount of the movement should be proportional to the applied voltage. It is desirable to have a mechanically rigid scanner with high resonant frequency for better vibration isolation and feedback performance.

A tripod scanner, with three piezoelectric bars arranged orthogonal to each other, was commonly used in early years of STM. Piezoelectric tube scanners [11] soon became popular due to its simple structure, high sensitivity, and high resonant frequency. A schematic of a tube scanner is shown in Fig. A2(a). A tube made of PZT ceramics is poled in the radial direction and metallized on the outer and inner surfaces. The inner surface is connected to the z voltage, and the tip is attached to center of the tube. The outer surface is sectioned into four quadrants, where two neighboring quadrants are assigned as x and y electrodes. The tube scanner moves the tip by bending sideways when asymmetrical voltages are applied to either the x or y pair of electrodes. When symmetrical voltages are applied to the four quadrants, the tube either extends or contracts in length which controls the tip height. The wall thickness h of the piezoelectric tube is kept much smaller than the diameter D, so that stress and strain variation over the wall thickness can be neglected.

Let's consider that equal and opposite voltages V are applied to the y pair of electrodes as shown in Fig. A2(b), while the x and z electrodes are grounded. As a result, a strain is generated in the z direction, $S_3 = (\delta z/z) = d_{31} V/h$ where d_{31} is a piezoelectric constant. It in turn creates a stress $\sigma_3 = YS_3$ in the z direction, where Y is the Young's modulus of the material. A positive stress is generated in one of the y quadrants and negative stress in the other. The torque due to the pair of forces, causes the tube to bend. The curvature of the bending is given by [12]

$$R = \frac{\pi Dh}{4\sqrt{2}d_{31}V}$$ (1)

As a result, deflection in the y direction is given by

$$\Delta y = \frac{L^2}{2R} = \frac{2\sqrt{2}d_{31}VL^2}{\pi Dh}$$ (2)

Similarly, if equal and opposite voltages are applied to the x pair of electrodes keeping the y and z electrodes grounded, an expression for the x deflection will be identical. Applying the same voltage to all four x and y electrodes [Fig. A2(c)], the displacement in the z direction is given by

$$\Delta z = \Delta L = d_{31}V\frac{L}{h}$$ (3)

Note that motion in the z direction can also be controlled by applying voltage to the inner wall electrode.

III. Vibration isolation

To achieve atomic resolution in STM imaging, variations in the tip-sample gap must be less than a picometer [3]. However, the amplitude of typical environmental vibrations is in the range of nm to microns, which is several orders of magnitudes greater than the vibration

levels required for atomic scale imaging. Thus, effective isolation is absolutely necessary to reduce vibrations at the tip-sample junction. In the first STM, Binning and Rohrer used superconducting magnetic levitation at liquid helium temperature to keep the STM free from the vibrations [13]. A number of different mechanisms have been developed since then, such as spring suspension system with magnetic damping [14] and the use of viton elements between metallic plates to form a stack [15].

The environmental vibrations that affect the performance of STM can be divided into high and low frequency noises. High frequency vibrations (>100 Hz) that arise from vacuum pumps, can be minimized by keeping the microscope inside an acoustical chamber. The common sources of low frequency environmental vibrations (1-100 Hz) are people walking, closing and opening doors, as well as floor and building wall vibrations. The most popular way to minimize these vibrations in modern UHV systems is suspending the STM unit from a chamber using springs with eddy current dampers, and mounting the entire chamber on a table which is decoupled from the floor by vibration isolation legs. Thus, a complete STM system can be divided into two subsystems, an STM unit with tip assembly and a vibration isolation system [Fig. A3(a)].The principle of isolation exist in making natural resonant frequencies of the two subsystems very different from each other [16].

To illustrate physics of the vibration isolation, let's consider a vibrating system where a point mass M is mounted on a frame through a spring and viscous damper as shown in Fig. A3(b). Here, the frame represents the STM base plate and the mass represents the tip assembly. Considering vibrations with only one degree of freedom, the displacements

of the mass and the frame in vertical direction from equilibrium positions are described by $x(t)$ and $x'(t)$ respectively. The Newton equation of motion for the mass is

$$M\ddot{x} + c(\dot{x} - \dot{x}') + k(x - x') = 0 \tag{4}$$

where second and third term corresponds to damping and restoring force, respectively. Rewriting Eq. (4) in terms of the natural frequency ω_0 and damping constant Y,

$$\ddot{x} + 2Y\dot{x} + \omega_0^2 x = 2Y\dot{x}' + \omega_0^2 x' \tag{5}$$

where
$$\omega_0 = 2\pi f_0 = \sqrt{k/M} \quad and \quad Y = c/2M \tag{6}$$

For a sinusoidal vibration of the frame, the motion of the mass should also be sinusoidal

$$x'(t) = x_0' e^{i\omega t} \quad and \quad x(t) = x_0 e^{i\omega t} \tag{7}$$

Substituting Eq. (7) into Eq. (5), the relative amplitude of the two displacements is

$$\frac{x_0}{x_0'} = \frac{\omega_0^2 + 2iY\omega}{\omega_0^2 - \omega^2 + 2iY\omega} \tag{8}$$

The transfer function, which is a response of the tunneling gap distance $(x_0 - x_0')$ to a vibrational amplitude (x_0'), is given by

$$\Gamma_1(\omega) = \left| \frac{x_0 - x_0'}{x_0'} \right| = \sqrt{\frac{\omega^4}{(\omega_0^2 - \omega^2)^2 + 4Y^2\omega^2}} \tag{9}$$

An efficient vibration isolation means a small transfer function. In the lower frequency range $\Gamma_1(\omega) \approx (\omega/\omega_0)^2$. If the resonant frequency ω_0 is high, say 2 kHz, the system response will be sufficiently small $\sim 10^{-6}$ for driving frequencies below 2 Hz. Therefore, the STM unit should have a very high resonant frequency for efficient vibration isolation. This can be achieved by making the tunneling unit small and as rigid as possible.

Now we reconsider the vibrating system shown in Fig. A3(b), with the frame representing the lab floor and the mass representing the STM vibration isolation system. The Newton's equation of motion for the mass is equivalent to Eq. (5)

$$\ddot{x}' + 2\Upsilon\dot{x}' + \omega_1^2 x' = 2\Upsilon_1\dot{X} + \omega_1^2 X \tag{10}$$

where

$$\omega_1 = \sqrt{k'/M'} \qquad and \qquad \Upsilon_1 = c/2M' \tag{11}$$

The transfer function for the vibration isolation system versus the floor is defined as the ratio of the two amplitudes

$$\Gamma_2(\omega) = \left|\frac{x_0'}{X_0}\right| = \sqrt{\frac{\omega_1^4 + 4\Upsilon_1^2\omega^2}{(\omega_1^2 - \omega^2)^2 + 4\Upsilon_1^2\omega^2}} \tag{12}$$

At higher frequencies, if damping is negligible, then the transfer function is inversely proportional to the excitation frequency $\Gamma_2(\omega) \approx (\omega_1/\omega)^2$. The vibration isolation is more efficient at higher frequencies, but there are large oscillations at the resonant frequency. To avoid such resonance excitation, appropriate damping is necessary. But heavy damping ($\Upsilon_1 \gg \omega_1$) affects efficiency of the vibration isolation at higher frequencies. Therefore, a compromise has to be made between the suppression of resonance and of high frequency vibrations. It is clear that at or below the natural frequency ω_1, vibrations will be enhanced instead of being attenuated. Therefore, the natural frequency of the vibration isolation system should be as low as possible.

The overall transfer function, response of the tunneling gap to the external vibrations, is given by the product of $\Gamma_1(\omega)$ and $\Gamma_2(\omega)$. For the intermediate frequency range ($\omega_1 \ll \omega \ll \omega_0$), Eq. (9) and Eq. (12) can be approximated and the overall transfer function for small damping condition is given by

$$\Gamma_1(\omega)\Gamma_2(\omega) = \left(\frac{\omega}{\omega_0}\right)^2 \left(\frac{\omega_1}{\omega}\right)^2 = \left(\frac{\omega_1}{\omega_0}\right)^2 \tag{13}$$

and for large damping condition

$$\Gamma_1(\omega)\Gamma_2(\omega) = \frac{2\Upsilon_1\omega}{\omega_0^2} \tag{14}$$

So best vibration isolation at the intermediate frequencies solely depends on the ratio of ω_1 and ω_0. Therefore it is desirable to have a low resonant frequency ω_1 for the vibrational isolation stage, and a high resonant frequency ω_0 for the STM tunneling unit. For a spring suspension system, the resonant frequency of the system depends only on the stretched length of the spring $\omega = \sqrt{K/M} = \sqrt{g/\Delta L}$ because the stretched length due to the mass m is related to the spring constant by $mg = k\Delta L$.

For a more sophisticated vibration isolation, systems using a two-stage suspension spring with eddy current damping are used [Fig. A3(c)]. The Newton equations for the two masses are

$$m_1\ddot{x}_1 + c_1(\dot{x}_1 - \dot{X}) + k_1(x_1 - X) + c_2(\dot{x}_1 - \dot{x}_2) + k_2(x_1 - x_2) = 0 \tag{15}$$

$$m_2\ddot{x}_2 + +c_2(\dot{x}_2 - \dot{x}_1) + k_2(x_2 - x_1) = 0 \tag{16}$$

Extending the earlier analysis to the double stage system, the transfer function is given by the ratio of the vibration amplitudes of the second mass and of the frame [3].

$$\Gamma(\omega) = \left|\frac{x_2}{X_0}\right| = \frac{\omega_0^2\omega_1^2}{|\omega^4 + (\omega_0^2 + \omega_1^2 + \omega_2^2)\omega^2 + \omega_0^2\omega_1^2|} \tag{17}$$

Where $\omega_1 = \sqrt{k_1/m_1}$ and $\omega_2 = \sqrt{k_2/m_1}$. In order to have a minimum transfer function, one should make (k_1/m_1) equal to (k_2/m_2), and ω_2 as small as possible. Thus, a heavier mass m_1 in intermediate stage is preferable. Also, the total stretched length of the springs

should be as large as possible. In general, the double stage system is much more efficient in vibration isolation compared to a single stage system with the same physical dimensions.

IV.   Control electronics

The basic electronics required to control the STM operation consist of a current amplifier, feedback controller, and a computer interface for data acquision [Fig. 4.1(a)].

Current amplifier: Since the tunneling current in STM is very small, the current amplifier is used to amplify it and then convert it into a voltage signal. An amplifier mainly consists of two components, an operational amplifier and a feedback resistor R_{FB}. The operational amplifier has a high input impedance, a high voltage gain, and a low output impedance. To a good approximation, the output voltage should provide a feedback current through feedback resistor to compensate input current such that net current entering the inverting input of the operational amplifier is zero. The non-inverting input is grounded. The output of the amplifier is $V_{out} = -I_{in}R_{FB}$. The minus sign indicates that phase is reversed. For $R_{FB} = 100M\Omega$, one nano-Ampere of input current will result in an output voltage of 100mV.

Feedback electronics: STM operation requires the use of a feedback loop to maintain a constant tunneling gap during the scan. Output of the logarithmic amplifier is compared with a reference voltage, which corresponds to the tunneling current set point. The difference of the two is then sent to the feedback circuit, which sends a voltage to the z piezo actuator. If the tunneling current is larger than the set point value, a voltage applied to the z piezo actuator tends to withdraw the tip from the sample surface, and vice versa. Thus, an equilibrium tip height is established through the feedback loop.

Computer interface: Most of the STM operations are controlled by a computer and hence a computer interface is an essential part. Computer software and digital to analog converters are used to generate voltage ramps, that are applied to x and y piezo actuators to raster scan the tip. The voltage reading of the z piezo actuator is taken to the computer with an analog to digital converter. With the use of a dedicated microprocessor, the tunneling voltage, feedback on/off signal and z output can also be generated by a computer.

V. Lock-in amplifier

A lock-in amplifier is a powerful tool used to detect a very small AC signal (up to few nanovolts), even when signal is obscured by an extremely noisy environment. A lock-in amplifier is based on a phase-sensitive detection technique which measures the amplitude of a signal at a specific reference frequency and phase, and ignores noise signals at frequencies other than the reference frequency. The lock-in amplifier is commonly used to directly measure the dI/dV as a function of electron energy.

Let's consider a sinusoidal input signal $V_S \sin(\omega_s t + \theta_s)$, where V_S, ω_s and θ_s are the signal amplitude, frequency and phase, respectively. Along with the input signal, lock-in measurements require a reference signal $V_R \sin(\omega_R t + \theta_R)$. The lock-in amplifies the input signal and then multiplies it by the reference signal using a phase-sensitive detector or multiplier. The output of the detector,

$$V_{Out} = V_S V_R \sin(\omega_s t + \theta_s) \sin(\omega_R t + \theta_R)$$

$$= \frac{1}{2} V_S V_R \big[\cos\big((\omega_s - \omega_R)t + \theta_s - \theta_R\big) - \cos\big((\omega_s + \omega_R)t + \theta_s + \theta_R\big) \big] \quad (18)$$

consists of two AC signals, one at a difference in frequencies $(\omega_s - \omega_R)$ and the other at a sum in frequencies $(\omega_s + \omega_R)$. If ω_R is set equal to ω_s, the Ist term will be a DC signal. If

the detector output is passed through a low pass filter while keeping ω_R equal to ω_s, then the 2nd term will be removed. The filtered output will be

$$V_{Out} = \frac{1}{2} V_S V_R \cos(\theta_s - \theta_R) \tag{19}$$

This is a nice DC signal proportional to the amplitude of the input signal. Here, the phase of the input signal and the reference signal should not change with time, otherwise $\cos(\theta_s - \theta_R)$ will change with time and V_{Out} will not be a DC signal. Thus, the lock-in reference signal needs to be phase-locked to the input signal.

In practice, the input signal is made up of a signal plus noise instead of a pure sine wave. The amplifier then responds only to the portion of the input signal that occurs at the reference frequency with a fixed phase relationship. Noise signals at frequencies far from the reference frequency are attenuated by the low pass filter. However, attenuation of noise at frequencies very close to the reference frequency depends upon the low pass filter bandwidth. A narrower bandwidth filter removes noise very close to the reference frequency.

References

1. J. P. Ibe *et al.* On the electrochemical etching of tips for scanning tunneling microscopy. *J. Vac. Sci. Technol. A* **8,** 3570 (1990)

2. R. Zhang, and D. G. Ivey. Preparation of sharp polycrystalline tungsten tips for scanning tunneling microscopy imaging. *J. Vac. Sci. Technol. B* **14,** 1 (1996).

3. C. J. Chen. Introduction to scanning tunneling microscopy. Oxford University Press, 2nd edition, New York (2008).

4. H. W. Fink *et al.* Mono-atomic tips for scanning tunneling microscopy. *IBM J. Res. Develop.* **30,** 460 (1986).

5. S. Earnst *et al.* Optimization of the preparation process for tips used in scanning tunneling spectroscopy. Thesis, chapter 3, Max-Planck-Institut fˈur Chemische Physik fester Stoffe, Dresden.

6. G. Binning and H. Rohrer, Scanning tunneling microscopy. *Helv. Phys. Acta.* **55,** 726 (1982).

7. R. M. Feenstra, J. A. Stroscio and A. P. Fein. Tunneling spectroscopy of the Si(111)-2×1 surface. *Surf. Sci.* **181,** 295 (1987).

8. L. Limot, T. Maroutian, P. Johansson and R. Berndt. Surface-state Stark shift in a scanning tunneling microscope. *Phys. Rev. Lett.* **91,** 196801 (2003).

9. Y. Zhang *et al.* Giant phonon induced conductance in scanning tunneling spectroscopy in gate tunable graphene. *Nat. Phys.* **4,** 627 (2008).

10. Y. Y. Li, M. X. Chen, M. Weinert and L. Li. Direct experimental determination of onset of electron-electron interactions in gap opening of zigzag graphene nanoribbons. *Nat. Commns.* **5,** 4311 (2014).

11. G. Binning and D. P. E. Smith. Single tube three dimensional scanner for scanning tunneling microscopy. *Rev. Sci. Instrum.* **57,** 1688 (1986).

12. C. J. Chen. Electrochemical deflections of piezoelectric tubes with quartered electrodes. *Appl. Phys. Lett.* **60,** 132 (1992).

13. G. Binning and H. Rohrer. Scanning tunneling microscopy. *Surf. Sci.* **126,** 236 (1983).

14. S. I. Park and C. F. Quate. Theories of feedback and vibration isolation systems for the scanning tunneling microscope. *Rev. Sci. Instrum.* **58,** 2004 (1987).

15. M. P. Cox and P. R. Griffin. A high performance Scanning tunneling microscope. *J. Vac. Sci. Technol. A* **6,** 376 (1988).

16. M. Okano, K. Kajimura, S. Wakiyama, F. Sakai, W. Mizutani and M. Ono. Vibration isolation for scanning tunneling microscopy. *J. Vac. Sci. Technol. A* **5,** 3313 (1987).
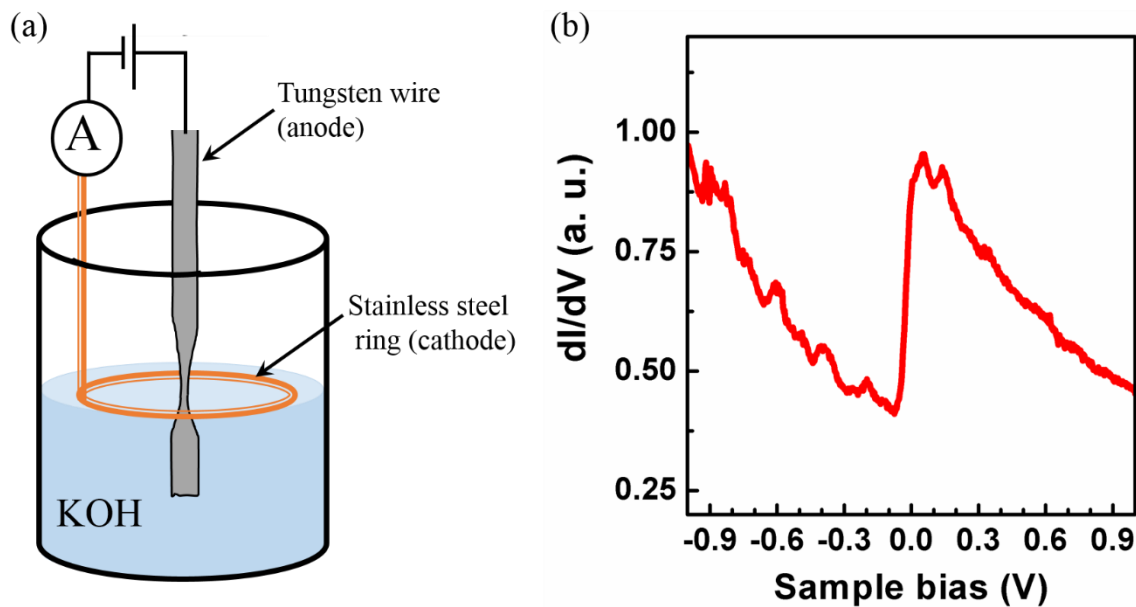
Figure A1: (a) Schematic of the electrochemical etching setup for a tungsten tip using KOH electrolyte solution. A voltage is applied between anode and cathode for an etching reaction to take place. (b) A typical dI/dV spectrum taken on Ag film/SiC. A step like feature in conductance near zero sample bias indicates the presence of metallic surface states.
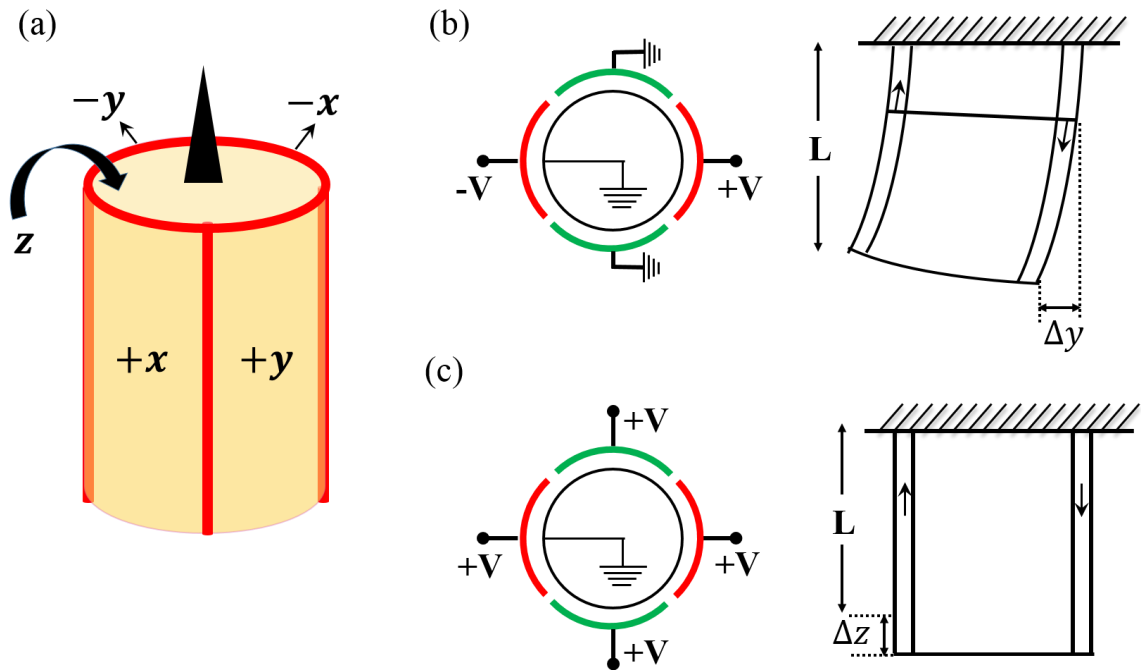
Figure A2: (a) Piezoelectric tube scanner: z electrode is connected to the inner surface and x and y electrodes to the adjacent quadrants on the outer surface. (b) Opposite and equal voltages applied to the y electrodes lead to a deflection of tube scanner in y direction. (c) Application of equal and symmetric voltages to the four electrodes on the outer surface result in extension of tube length along its axis.
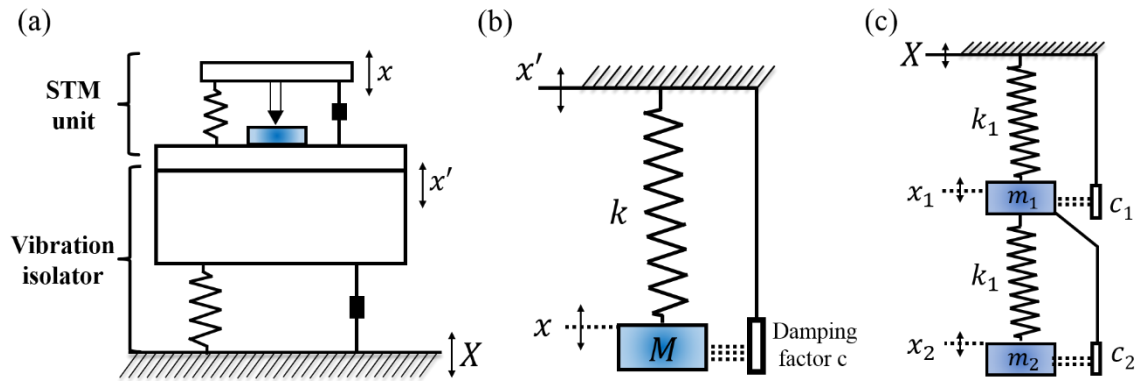
Figure A3: (a) Schematic of the STM subsystems, an STM tunneling unit and a vibration isolator. Model of (b) a single and (c) double stage suspension spring vibration isolation system with one degree of freedom.

CURRICULUM VITAE

Shivani Rajput
shivanirjpt@gmail.com

Education

Ph.D., Condensed Matter Physics (Aug 2009- Jul 2015)
University of Wisconsin, Milwaukee, WI, USA
GPA: 3.78/4.00
<u>Dissertation Title:</u> Tunneling Experiments with Dirac Electrons in Graphene
Heterojunctions

M. Sc., Physics (2004- 2006)
C.C.S. University, Meerut, Uttar Pradesh, India
GPA: 77.46/100

B. Sc., Physics (H) (2001- 2004)
University of Delhi, New Delhi, India
GPA: 62.3/100

Technical skills

- **Material synthesis**
  - Growth experience with molecular beam epitaxy (MBE), sputtering, thermal and electron beam evaporation
  - Polymer based fabrication of van der Waals heterostructures

- **Characterization techniques**
  - Scanning tunneling microscopy/spectroscopy (STM/STS), Raman spectroscopy, atomic force microscopy (AFM), and scanning electron microscopy (SEM)

Research Publications

1. **S. Rajput,** Y. Y. Li, M. Weinert and L. Li. Indirect bonding mechanism for proximity-induced giant spin-orbit coupling in graphene-topological insulator van der Waals heterostructure. *Nat. Commun.* (Submitted)

2. D. Tomer, **S. Rajput**, L. J. Hudy, C. H. Li and L. Li. Inhomogeneity in barrier height at graphene/Si (GaAs) Schottky junctions. *Nanotechnol.* **26,** 215702 (2015).

3. D. Tomer, **S. Rajput**, L. J. Hudy, C. H. Li and L. Li. Carrier transport in reverse biased graphene-semiconductor Schottky junctions. *Appl. Phys. Lett.* **106,** 173510 (2015).

4. T. Hosseini, D. Tomer, **S. Raiput**, L. Li and N. Kouklin. Transport and photoconduction characteristics of metal-graphene-4H-SiC(0001) heterojunction devices. *Appl. Phys. Lett.* **105,** 223107 (2014).

5. D. Tomer, **S. Rajput**, L. J. Hudy, C. H. Li and L. Li. Intrinsic inhomogeneity in barrier height at monolayer graphene/SiC Schottky junction. *Appl. Phys. Lett.* **105**, 021607 (2014).

6. Y. Liu, Y. Y. Li, **S. Rajput**, D. Gilks, L. Lari, P. L. Galindo, M. Weinert, V. K. Lazarov and L. Li. Tuning Dirac states by strain in the topological insulator Bi_2Se_3. *Nat. Phys.* **10**, 294 (2014).

7. **S. Rajput**, Y.Y. Li and L. Li. Direct experimental evidence for the reversal of carrier type upon hydrogen intercalation in epitaxial graphene/SiC(0001). *Appl. Phys. Lett.* **104,** 041908 (2014).

8. **S. Rajput**, M. X. Chen, Y. Liu, Y. Y. Li, M. Weinert and L. Li. Spatial fluctuations in barrier height at the graphene-SiC Schottky junction. *Nat. Commun.* **4,** 2752 (2013).

9. E. S. Krystofiak, **S. Rajput**, R. M. Albrecht, M. Gajdardziska-Josifovska and J. A. Oliver. Synthesis and characterization of magnetite-gold core-shell nanoparticles. *Microscopy & Microanalysis* **16,** 1714 (2010).

10. R. P. Sharma, P. Sharma, **S. Rajput** and A. K. Bhardwaj. Suppression of stimulated Brillouin scattering in laser beam hot spots. *Laser and particle beams* **27,** 619 (2009).

Conference Presentations

- "When graphene meets semiconductor: An atomic scale study of Schottky Barrier Formation", [Oral Presentation] MRS spring 2015, San Francisco, CA, U.S.A.

- "Scanning tunneling microscopy/spectroscopy of graphene-MoS_2 heterojunction", [Oral Presentation] APS March meeting 2015, San Antonio, TX, U.S.A.

- "When graphene meets semiconductor: An atomic scale study of Schottky Barrier Formation", [Oral Presentation] Physical Electronics Conference 2014, La Crosse, WI, U.S.A.

- "Spatial fluctuation in barrier height at the graphene-silicon carbide Schottky junction", [Oral Presentation] APS March meeting 2014, Denver, CO, U.S.A.

- "Polarization induced p-type doping in the H-intercalated epitaxial graphene on SiC(0001)", [Oral Presentation] AVS meeting 2013, Long beach, CA, U.S.A.

- "Scanning tunneling microscopy/spectroscopy study of hydrogen intercalated epitaxial graphene on SiC (0001)", [Oral Presentation] APS March meeting 2013, Baltimore, MD, U.S.A.

- "A study of epitaxial graphene/SiC(0001) functionalized by nitrogen doping", [Oral Presentation] APS March meeting 2012, Boston, MA, U.S.A.

Awards/Achievements

- Travel award for American Vacuum Society (AVS) 2013, Long Beach, CA, USA
- David Lichtman scholarship for best experimental physics graduate student 2012, UWM, USA
- Ministry of Human Resource and Development (MHRD) fellowship 2007, IITD, India
- Graduate Aptitude Test in Engineering (GATE) award 2005, INDIA
- Gold medalist of intra-university YOGA competition 2004, C.C.S. University, India